Signal proxy and radiative Bhabha background studies: contributions to the search for invisibly decaying dark photons at Belle II

by

Daniel Weston Mckay Crook

B.Sc., McGill University, 2021

A THESIS SUBMITTED IN PARTIAL FULFILLMENT
OF THE REQUIREMENTS FOR THE DEGREE OF

Master of Science

in

THE FACULTY OF GRADUATE AND POSTDOCTORAL
STUDIES

(Physics)

The University of British Columbia

(Vancouver)

August 2023

The following individuals certify that they have read, and recommend to the Faculty of Graduate and Postdoctoral Studies for acceptance, the thesis entitled:

Signal proxy and radiative Bhabha background studies: contributions to the search for invisibly decaying dark photons at Belle II

submitted by **Daniel Weston Mckay Crook** in partial fulfillment of the requirements for the degree of **Master of Science** in **Physics**.

Examining Committee:

Christopher Hearty, Professor, Physics and Astronomy, UBC
Supervisor

Janis McKenna, Professor, Physics and Astronomy, UBC
Supervisory Committee Member

Abstract

The nature of dark matter is one of the greatest extant mysteries in physics. Many hypotheses have been proposed to explain dark matter, but none have ever been substantiated. Some of these hypotheses propose dark sectors, i.e., entire families of dark matter particles. One such hypothesis is that of the dark photon, a massive, gauge boson which would be the mediator of the dark electromagnetic force. The dark photon would couple feebly to the photon, and thereby be producible through e^+e^- annihilation at a particle collider. Described here are contributions toward a search for the dark photon at Belle II, an electron-positron collider experiment in Japan. This search focuses on invisible decays of the dark photon, with a single initial-state radiation photon serving as the only evidence of the production and decay. Due to the delicate nature of this event signature, the dark photon search requires a carefully constructed set of event requirements and vetoes that remove as much background as possible without removing a large amount of the signal. To further this goal, two control samples were designed. One control sample is of a clean radiative dimuon sample, used as a signal proxy, while the other is of the radiative Bhabha background. These control samples are then used to design vetoes and selection criteria for the search for the dark photon at Belle II, termed the single-photon analysis.

Lay Summary

Through many astronomical observations, physicists have shown that the majority of mass in our universe is not ordinary, visible matter. The majority of mass in our universe appears to be invisible, meaning that it does not interact with light; this mass is thus called dark matter. While decades of physics have produced and tested a model that describes regular matter, it doesn't incorporate dark matter at all, and there is very little understanding of what dark matter is. As one of the greatest mysteries in physics, an empirical explanation of dark matter could revolutionize the field. This thesis presents part of an analysis that uses data from the Belle II particle collider experiment to search for a potential form of dark matter, a hypothetical particle called the dark photon.

Preface

This thesis is based on data of the Belle II experiment, which is a large, international collaboration. The result is original and as yet unpublished.

The single photon analysis is performed by a collaboration of groups at two universities. At UBC, this group consists of my supervisor Prof. Christopher Hearty, and Dr. Michael De Nuccio. At Karlsruhe Institute of Technology, this is Prof. Torben Ferber, and Dr. Giacomo De Pietro. Miho Wakai and Dr. Sam Cunliffe have previously worked on this analysis.

The design of the analysis was done by the aforementioned group at Belle II. The sections of work presented in the analysis section are entirely the author's own, as are the figures in that section. The data and Monte Carlo events used in this thesis were produced by the Belle II collaboration. The beams used by Belle II were produced by the SuperKEKB accelerator. The data used here was collected from 2019 to 2022 by the Belle II collaboration, a process in which the author of this thesis was not involved.

Table of Contents

List of Tables

List of Figures

xii

List of Symbols

α Fine structure constant

α_μ Angle between the recoil photon and the closer muon, measured at the ECL

α_D Dark fine structure constant

α_E Angle between an extra photon and the single photon

α_K Angle between a KLM cluster and the single photon

α_R Angle between the recoil photon and recoil momentum vectors

γ Photon

ε Strength of mixing

θ Polar angle

θ_R Theta of the recoil photon

$\mu^\mp$ Muon

$\tau^\mp$ Tauon

$\Upsilon(4S)$ Upsilon meson at the 4S resonance

$\Upsilon(5S)$ Upsilon meson at the 5S resonance

ϕ Azimuthal angle

χ Lightest dark matter particle

A'	Dark photon
A'_μ	Dark photon gauge field
C_{2M}	Cluster second moment
dr	Distance from IP to POCA in the x-y plane
dt99	Width of the time distribution that 99% of photons of a given energy fall into
dz	Distance from IP to POCA in z
e	Elementary charge
$e^\mp$	Electron or positron
E^*	Centre of mass energy
E_t	Energy associated with a track in the ECL
$F'^{\mu\nu}$	Dark field strength tensor,
I_K	Innermost KLM layer in a cluster
J^μ_{EM}	Standard Model electromagnetic current
L_μ	Likelihood of a particle being a muon
m_χ	Mass of the lightest dark matter particle
$m_{A'}$	Mass of the dark photon
m_R	Mass recoiling against the dimuon system
n_{CDC}	Number of hits in the CDC
n_K	Number of KLM layers in a cluster
n_{OOT}	Number of out-of-time crystals in the ECL
p	Momentum of a track

p_μ Momentum of the muon

p_P Momentum of the recoil photon

p_R Recoil momentum

p_T Transverse momentum of a track

$\mathcal{R}$ Ratio of the cross sections of e^+e^- to hadrons and e^+e^- to muons

r Orbital distance

t_c Timing of an ECL cluster

t_K Timing of a KLM cluster

Z_{MVA} Cluster Zernike multivariate analysis (MVA)

List of Abbreviations

ARICH   aerogel ring-imaging Cherenkov

basf2   Belle II analysis software framework

CDC   central drift chamber

CMB   cosmic microwave background

CMS   centre of mass

DAQ   data acquisition

ECL   electromagnetic calorimeter

EM   electromagnetism

FPGA   field programmable gate arrays

gbasf2   grid based Belle II analysis software framework

GR   general relativity

HLT   high level trigger

IP   interaction point

ISR   initial-state radiation

KLM K_L^0 and muon detector

L1   level 1

MC   Monte Carlo

MIP   minimum ionizing particle

MOND   modified Newtonian dynamics

MVA   multivariate analysis

POCA   point of closest approach

PXD   pixel detector

ROC   receiver operating characteristic

RPC   resistive plate chamber

SP   single photon

SVD   silicon vertex detector

TOP   time-of-propagation

Acknowledgments

I would like to express my gratitude to numerous people. Firstly, I extend my sincere thanks to Chris for guiding and supporting me throughout this research. I am truly appreciative of Michael's guidance and exceptional editing skills, which significantly enhanced the quality of this thesis. I also extend my thanks to Miho for her constant presence in the office, as well as her assistance and friendship. Additionally, I appreciate the contributions of the rest of the UBC Belle II group, including those who have since left.

Thank you to my entire family, with a special mention for my mom, dad, and sister (I'd definitely get called out by my mom if I didn't thank her specifically) to whom I talked whenever I needed distraction or commiseration. My appreciation also goes out to all my friends for their camaraderie and unwavering support. A heartfelt thanks is reserved for my extraordinary partner, Emma.

Thank you also to Metric; it is doubtful I could have continued working as late into the evening without your music.

Chapter 1

Introduction

The Standard Model of particle physics is a theory that describes the fundamental particles and their interactions, aside from gravity. It dates from the second half of the 1900s, and has been extremely successful, especially in predicting the existence of undiscovered particles. The Standard Model divides particles into categories based on their spin and how they interact, and reveals the intricate structure through the use of group theory and quantum field theory. However, with the discovery of the Higgs Boson in 2012, the predictions of the Standard Model have been mostly exhausted. The Standard Model has been extensively tested, and has not yet been convincingly disproven, though there are many questions that it leaves unanswered. Chief among these is the matter-antimatter asymmetry in the universe, the existence of neutrino masses, and the existence of dark matter and dark energy. The Standard Model has also thus far been irreconcilable with theories of gravity. As such, searching for new physics, or physics beyond the Standard Model, is a major area of research in particle physics.

1.1 Dark matter and evidence for its existence

Dark matter is the name we give to the cause of a variety of gravitational effects that physicists have observed that are not explained by our theory of gravity, general relativity (GR). There are some physicists who advocate for new models of gravity as the solution, instead of dark matter. The modified Newtonian dynamics (MOND)

scheme is one of several proposed alternatives that claim to remove the need for dark matter, however it has serious flaws [4], and there are currently no widely accepted or plausible alternatives to GR.

There are a great number of empirical observations that indicate or strongly support the existence of dark matter. Several of the most famous or relevant pieces of evidence are briefly summarized here:

- Rotation curves are the graph of the rotational speed of stars and gas around the centre of the galaxy as a function of their distance from it. The data for these graphs comes from measurements that use redshifted 21 cm light, which corresponds to the emission line of atomic hydrogen, and from photometry measurements of the brightness of the stars [6].

  Following Newtonian dynamics, Kepler's third law can be used, which is equivalent to setting the gravitational force equal to the centripetal force. As such, theory predicts that the rotational speed of the disk should be proportional to $1/\sqrt{r}$, where r is the orbital distance, as the visible mass of the disk decreases. However, when the observational data is compared to theory, it becomes clear that the two do not agree, because experimental evidence indicates the rotational curve becomes roughly flat towards the edge of the disk, and even far beyond as the mass becomes much less dense [6]. Figure 1.1 shows the data and theory comparison for the spiral galaxy NGC 3198.

  The widely accepted solution to this discrepancy is that there must be more mass in the galaxy, mass that we aren't able to observe. This mass is in the shape of a roughly spherical halo, and is therefore referred to as the dark matter halo [6].

- The cosmic microwave background (CMB) is radiation from photons emitted after the cooling and formation of neutral hydrogen in the early universe [12]. These photons have been redshifted to the microwave range as the universe has expanded. The CMB spectrum is a near perfect blackbody with a temperature of 2.73 K [21]. The CMB is isotropic to the 10^{-5} level, and the very small anisotropies provide a wealth of knowledge, including that baryons account for only a fraction of the mass density of the universe. This
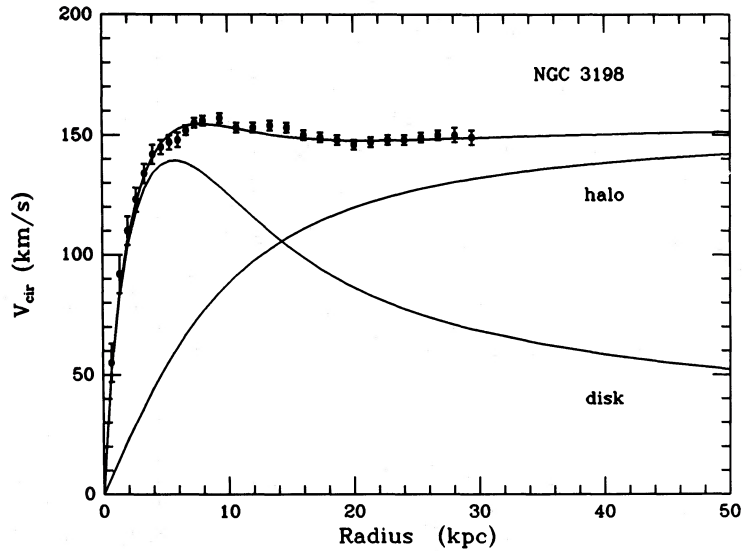
Figure 1.1: The rotation curve for the spiral galaxy NGC 3198. Data is shown
with error bars. The data has a curve fit to it, and also displayed are two
curves for the rotational curve for the visible disk, and for the theoretical
halo component. It is clear that the visible disk curve does not fit the data
by itself. Figure from [30].

indicates there must be non-baryonic dark matter, and precise CMB measure-
ments can also provide an estimate for the total amount [21].

• GR predicts that the curvature of space affects light, not just objects with
mass. This means that large concentrations of mass can cause light to curve,
and bend light around distant objects or create multiple images of one light
source. The deflection of the light corresponds to the mass of whatever
caused the space-time curvature, allowing a mass estimate of distant plan-
ets, galaxies, and galaxy clusters. By using bright galaxies or point-like
sources such as quasars, the masses of galaxies can be precisely calculated
and compared to the observable mass. These comparisons indicate that there
is a lot of dark matter in galaxies, including galaxies where the dark matter
is the vast majority of the mass present [3].

A particularly compelling case of the gravitational lensing argument is that

of the Bullet cluster. It's a galaxy cluster that contains two colliding galaxy clusters [25]. The components of the colliding clusters behave differently, with the mass centres (as imaged using gravitational lensing) having continued moving, while the visible matter in the form of plasma clouds having slowed down due to electromagnetic interactions. These plasma clouds are easily visible due to their X-ray emission [11]. Without dark matter the centre of mass map would correspond to that of the visible matter, in this case, primarily the plasma. As an image of the visible matter and mass centres shown in Fig. 1.2 demonstrates however, these visible mass and mass centres are significantly different, providing strong evidence for the existence of dark matter [25]. The Bullet cluster is often considered to refute the MOND theories for alternative gravity, or at least remove the ability of MOND to avoid the idea of dark matter [10].

For more dark matter evidence, or details on the evidence above, see [6] and [3].

Despite all the evidence for its existence, little is known about dark matter, and there are not many qualities we can say with certainty it has. We do know it has mass, and that there is much more of this mass than there is regular matter. Dark matter must also be stable [8]. It is an intensively studied subject though, and there is much we can say dark matter is not. It is generally accepted that dark matter is non-baryonic, and simulations of structure formation of the universe show that hot (relativistic) dark matter is not viable explanation, ruling out neutrinos as dark matter [4] [5]. Dark matter must also have no electrical charge, and not interact, or at least interact very feebly with the photon and all other Standard Model particles (excluding through gravity). If it interacted more strongly it would it be visible by other means. These requirements rule out all Standard Model particles, leaving new particles as the only possible candidates [4]. This of course assumes that it is particle based, which it might not be, but given the success of the Standard Model, it seems a reasonable assumption [8].

Many hypothetical particles have been proposed, with various degrees of theoretical backing, and as our knowledge has improved, many of these have been ruled out. Physicists have developed a check list of qualities that a dark matter

Figure 1.2: The Bullet cluster as imaged by Chandra, Hubble Space Telescope, and gravitational lensing analyses. Image from [1]. This image is from after the collision of the galaxy clusters. The plasma, detected by its emission of X-rays, is shown in pink, and the gravitational centres measured by lensing are shown in blue. These regions are physically separated, providing evidence for dark matter. The visible matter has been slowed by interactions, while much of the mass of the clusters has continued to move.

candidate should have to be considered viable [29]. The 10 criteria on that list include checking the candidates' compatibility with current experimental and empirical evidence, such as searches that have already been conducted. There's also the question of whether the candidate could ever be probed experimentally. While not an absolute physical requirement, it must be a testable explanation to belong to the realm of science.

1.2   Dark sectors

Given the total mass of dark matter in the universe relative to that of Standard Model matter, there is every reason to assume that dark matter is of similar com-

plexity in nature to that of ordinary matter [8]. This potential complexity brings around the concept of a dark sector. Dark sectors are a hypothetical collection of dark matter particles and their mediators, analogous to that described by the Standard Model. Dark sectors may have structure and their own fields and gauge interactions, but do not interact through standard model gauge groups [20].

Dark sectors must interact with regular matter through gravity, otherwise they fail to explain dark matter. However, for us to be able to detect them through other means, there must be some other interaction with regular matter. In dark sector models this interaction occurs through a portal [14]. Portal is the general term for the operator or interaction mechanism that connects the two sectors [27], and is called this because it can be thought of as the gateway between the two sectors. The interaction mechanism takes different forms depending on the model and what type of particle is mediating the interaction.

Portals are an important concept in dark sectors, though they are not without issues, because they ignore the gauge principle to at least some degree [14]. This is not necessarily a problem, but should not be ignored either, because the gauge principle is the basis for all known fundamental interactions [7].

The case which best respects the gauge principle is when the mediator is a spin 1 particle. Here, the interaction is caused by the coupling of a dark sector and Standard Model gauge boson. While there are many other possible mediators, including spin 1/2 and 0 particles, this thesis is concerned with the vector-mediator case, where a dark particle called the dark photon mixes with the photon.

1.3   Searching for dark matter at particle colliders

Due to the intense interest in the nature of dark matter, the number of searches and search techniques has rapidly proliferated in recent years. The search techniques can be categorized into one of three categories: direct detection, which looks for dark matter from the galaxy colliding with standard model particles; indirect detection, which looks for the standard model products of dark matter annihilating; and collider experiments that aim to produce dark matter through the collision of Standard Model particles [8]. All of these search techniques rely on the assumption that dark matter interacts, though feebly, with Standard Model particles.

Particle accelerators are machines that are able to accelerate various charged particles up to extraordinarily high energies. The beams of high-energy particles they produce can then be used to explore many areas of particle physics. Particle colliders are particle accelerators that collide two beams of high-energy particles.

Particle colliders are a common tool in the search for dark matter because they are able to cause a large number of particle interactions, or collisions, in a controlled manner, and at an often otherwise inaccessible energy. This opens up the study of rare decays of Standard Model particles that would not otherwise be observable in large enough numbers to draw useful conclusions. While the dark matter particles themselves are not detectable in such decays, the other products of the interaction are, and quantities such as the missing mass and missing energy can be measured [8]. This allows such events to be studied, and permits the measure of quantities of the dark matter candidate. As interactions involving dark matter must be quite rare, statistics are one of the key strengths of dark matter searches using particle colliders.

When models propose a dark matter candidate that could feasibly be produced in a particle collider experiment, we attempt to quantify how often we would expect this decay to occur, what it would look like in our experiment, and what other decays and effects may be present that would obscure it. We refer to these ideas and quantities as the cross section, signal, and backgrounds respectively.

Chapter 2

The Belle II detector

All information in this chapter that is not otherwise cited is from the Belle II Technical Design Report [13] and the Belle II Physics Book [22].

Belle II is a high-energy particle physics collider experiment based in Tsukuba, Japan. Belle II is the sole experiment that uses the SuperKEKB particle collider, the current holder of the world record for the highest instantaneous luminosity for a beam colliding experiment. SuperKEKB collides electrons and positrons after accelerating them to 7 GeV and 4 GeV respectively. The Belle II detector is built around the collision point, and is used to observe the results of the collision. Belle II is the successor to the Belle experiment, one of two original B-factory experiments, so called because the collision energies of such experiments are chosen so that they produce a large number of B mesons. Specifically, at Belle II, the centre of mass energy is 10.58 GeV [13], which corresponds to the energy of the $\Upsilon(4S)$ resonance. $\Upsilon(4S)$ is bottomonium, and decays primarily into two B mesons. Belle II is a next-generation B-factory experiment, and while B physics composes a large part of the Belle II physics program, it is not all Belle II is used for. Belle II is well suited to dark sector searches because of the precisely understood initial state, the hermetic nature of the detector, and the triggers designed specifically for such searches. Additionally e^+e^- collisions at this energy are relatively clean, with fewer particles produced by each collision.

The Belle II detector is composed of many subsystems and subdetectors. Figure 2.1 is a diagram that shows a cross section view from the top of the detector,

with the various components labelled. The detector is clearly asymmetric, with the point of collision off-centre. This is because of the asymmetry in the energy of the electron and positron beams, with the electron beam having 3 GeV more energy in the lab frame. The centre of mass (CMS) frame, therefore, is not the same as the lab frame and is boosted relative to it. This boost is in the same direction as the electron beam. This direction is more often called the forward direction, and is useful when discussing parts of the detector because of the aforementioned asymmetry. The detector is elongated in the forward direction and contains more detection elements, as most particles will tend to travel this way.

Figure 2.1: A cross section view from the top of the Belle II detector. Diagram from [22].

The coordinate system Belle II uses defines the forward direction as the positive z direction. For the Cartesian system, y is then defined as the positive vertical direction, and x is then horizontal by the right hand rule. However Belle II primarily uses spherical and cylindrical coordinate systems, with the same z definition. θ is

used to denote the polar axis, and ϕ for the azimuthal axis. See Fig. 2.2 for a diagram that shows the two coordinate systems in relation to the detector.
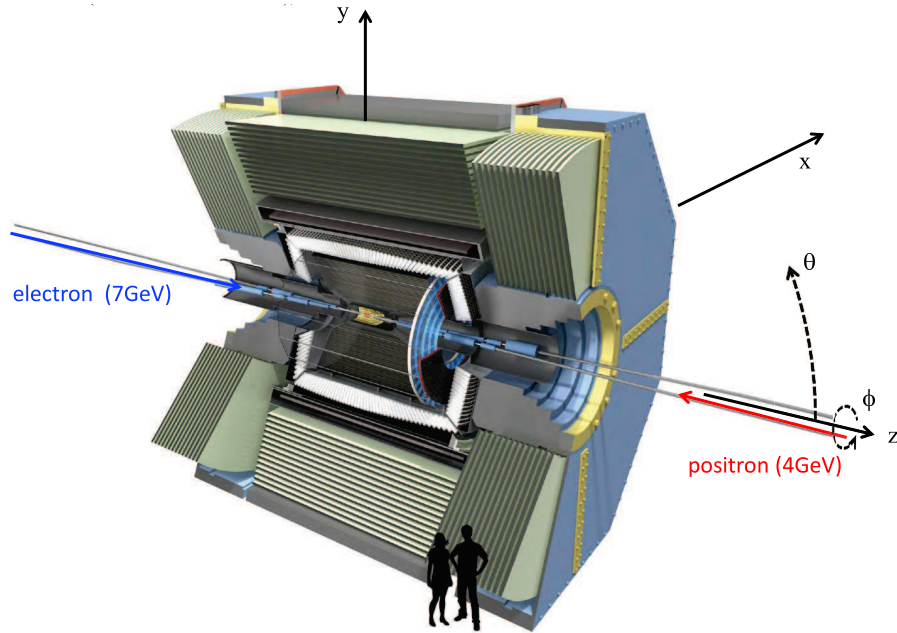
Figure 2.2: The coordinate systems for Belle II overlaid on the detector. Silhouetted people included for scale. The *z*-axis is in the direction of the electron beam, and *y* is vertical. θ and ϕ are defined from the Cartesian coordinates in the standard way. Image from [18].

Inside the core of the Belle II detector, there is a magnetic field that causes charged particles to follow trajectories that curve in ϕ. The magnetic field is created by the solenoid, shown in Fig. 2.1, and is uniform inside it, with a strength of 1.5 T. The solenoid axis is directly along the *z*-axis.

Belle II is designed to detect the results of the collision of an e^+e^- pair. The collision, and all associated detection information is called an event. Events have an event time, calculated by various subdetectors. All other times in the event are referenced to this time, with $t = 0$ ns being the same time as the event time. Events and their quantities will be referred to frequently in the rest of this thesis. The location in the detector at which the two beams collide is called the interaction

point (IP). The IP is not exactly at the origin of the coordinate system, though it is very close to it.

Due to the high luminosity of SuperKEKB, a significant beam-induced background is present at Belle II. This background, more commonly referred to as beam background, comprises various effects originating from the high-energy beams. It is necessary to discuss this background here because it is important to the design of many components of the detector, and to the design of the analysis conducted in this thesis. The primary causes of the beam background at Belle II include: synchrotron radiation, wherein high-energy particles emit radiation due to their curved trajectory; beam-gas scattering, wherein the few gas molecules in the beam pipe deflect the beam particles, causing them to interact with accelerator and detector components, resulting in particle showers; Touschek scattering, a phenomenon in which beam particles in one bunch deflect each other, also leading to showers of particles from interactions with material; and radiative Bhabhas, in which photons are emitted and then either shower in the detector, or travel along the beam pipe and interact with the magnets, thereby producing a substantial quantity of neutrons.

The details of the most relevant subdetectors and systems of the Belle II detector are described below. For a more in-depth description of Belle II, see the Technical Design Report [13].

2.1   Calorimetry

The main purpose of the calorimeter is to detect photons and electrons, and measure their energy and position. It also detects other particles however, and can be used to help refine their position. This type of calorimeter — one designed primarily for photons and electrons — is often referred to as an electromagnetic calorimeter. At Belle II, this detector is therefore called the ECL.

The Belle II calorimeter largely reuses the calorimeter from the Belle detector, and is composed of over 8000 crystals of CsI(Tl), which are wrapped in teflon, aluminum and mylar. The crystals are scintillators, and when non-photon particles enter them, they emit light. The photons that enter or are emitted in them remain inside by reflecting off of the materials in which they are wrapped, and the light is measured by photodiodes glued to the back of the crystals. The light output of the

scintillator is proportional to the energy of the particle deposited into the crystal, and is calibrated using $e^+e^- \rightarrow \gamma\gamma$ events [13].

The calorimeter crystals are arranged into three sections: the forward endcap, barrel, and backward endcap. Together these sections cover the entire range of ϕ in the angular range of $12.4° < \theta < 155.1°$, except for the gaps between the barrel and endcaps. These gaps in the calorimeter are for support structure and cable routing, and result in gaps in acceptance at $31.4° < \theta < 32.2°$ and $128.7° < \theta < 130.7°$ [2]. The shape and size of the crystals varies throughout the detector for two primary reasons: to allow the crystals to nest tightly together, and so that each row of crystals could be built tilted towards, though not directly at, the IP. These two design features reduce the probability of particles going through the calorimeter without depositing any energy in it, or for photons, without depositing their full energy. When energy 'leaks' out through the calorimeter, it is referred to as leakage. Some particles, such as muons, leave a specific amount of energy in the ECL, around 190 MeV; a particle that does this is referred to as a minimum ionizing particle (MIP).

A common way to refer to the polar position of a cluster in the calorimeter is with a quantity called thetaID. ThetaID corresponds to a ring of crystals in the calorimeter, and is used in place of θ because of its simplicity, and the clear way in which it relates to the detector. While θ values are available for clusters in the calorimeter, the determination of more precise location for the cluster than simply the centre of a crystal relies on a centroid algorithm which has been shown to not always return the best results. A diagram of the layout of crystals with their corresponding thetaID is shown in Fig. 2.3.

2.1.1 Clustering

Incoming particles do not in general deposit energy in just a single calorimeter crystal, and therefore the energy in the calorimeter must be reconstructed into clusters of crystals that are caused by the particles that interacted with it. What follows is a simplified description of the clustering method, containing only the most relevant parts.

Crystals that have more than 10 MeV are all considered as possible starting
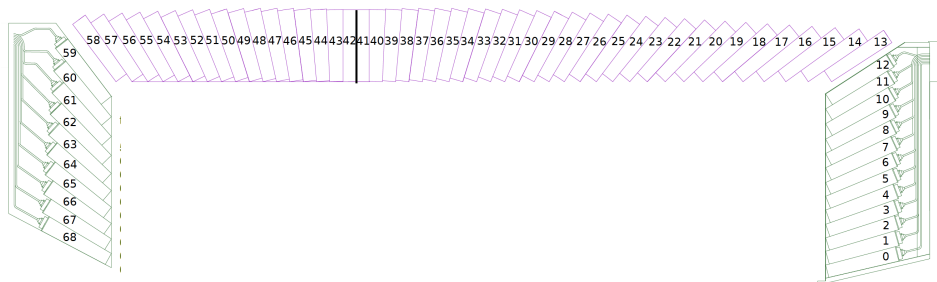
Figure 2.3: The layout of one line of crystals in the ECL. The right side of the diagram is the forward endcap, while the left is the backward endcap. Each crystal has its corresponding thetaID written on it. The black line between thetaIDs 41 and 42 signifies that the collision point is directly below that crystal gap and also indicates the presence of a 1.5 mm thick mechanical structure. The tilt of the crystals is illustrated in this diagram. Image from [19].

points for a group of crystals. These crystals then have all 8 nearest neighbours with at least 0.5 MeV added to their group. The groups merge if there are any crystals that are in both. The groups of crystals are then split into clusters, each with exactly one crystal that is both a local maximum, and above 10 MeV. The energy from each crystal is assigned to the nearest clusters according to its proximity to the position of the cluster, taken initially as the centre of the local maximum crystal. The exact position of the cluster is then calculated from the positions of each crystals belonging to a cluster using the energy assigned to the cluster from each crystal as a weight. The cluster energy and position are refined by iterating the process above. The maximum size of a cluster is 21 crystals arranged in a five by five grid with the corners excluded. The minimum energy of a cluster is 20 MeV.

Unfortunately, due to a bug in current reconstruction software, when there are more than 10 clusters in a group, only one cluster is reconstructed. This is much more likely to happen when there are many crystals with non-negligible amounts of energy in them, which occurs when the event is subject to high beam background conditions.

2.1.2 Variables

The calorimeter measures and provides a variety of quantities that can be used in event reconstruction or analysis. Those quantities that are used directly in this thesis are described below.

First and foremost, every cluster in the calorimeter will have an energy, θ, and ϕ position, as well as a thetaID value. In addition to this, the time of the cluster, t_c, is recorded, as well as a measure of the error on that time, dt99. The error on the timing is quantified as the width of the time distribution that 99% of photons of that energy would fall into. However, as this quantity has not been calibrated recently, and was calculated exclusively using simulated data, it can not be relied on to that extent. Despite this, it is still useful when considering the timing of clusters of different energies because the resolution of the cluster time is inversely proportional to the energy of it. Therefore, when comparing cluster timing across a wide range of energy it is better to use the ratio of these quantities, as the width of the time distribution accounts for the energy correlation, resulting in a roughly energy independent measurement of the time.

There are also several quantities that characterize the shape of the ECL cluster, such as the cluster Zernike multivariate analysis (MVA), Z_{MVA}, and cluster second moment, C_{2M}. These are referred to collectively as shower shape variables. Z_{MVA} can be used to distinguish photon clusters from other ECL clusters. It is a dimensionless quantity that ranges between 0 and 1, with the closer to 1 it is, the more photon-like the ECL cluster is. C_{2M} also helps to distinguish between ECL clusters, though in a more complicated manner that need not be discussed. It has units of cm^2.

There is also a useful calorimeter variable that applies to the event as a whole, as opposed to a particular ECL cluster: the number of out-of-time crystals in the ECL, n_{OOT}. This is the number of crystals that measure at least 7 MeV, and have an absolute value of t_c of at least 110 ns. n_{OOT} is a useful measure of the amount of energy and beam background present during and surrounding an event.

14

2.2 Tracking

Tracking in Belle II relies on several subdetectors, namely the pixel detector (PXD), the silicon vertex detector (SVD), and the central drift chamber (CDC). The purpose of the PXD and SVD is to detect the paths of particles near the IP. The information obtained is then used to reconstruct particle tracks and the vertices of particles that decayed near the IP. Both the PXD and SVD are silicon-based detectors, though of different designs.

The PXD is the innermost detector in Belle II, and is designed to be composed of two cylinders that encircle the beam pipe, though only one full layer and a fraction of the second layer has been installed. The cylindrical layers are both composed of many pixels of silicon, each of which is able to detect the passage of a charged particle through it. The pixels use DEPFET (DEPleted Field Effect Transistor) technology. DEPFET was chosen because this design has low noise at the expected operating temperature, and combines detection and amplification, allowing the readout electronics to be moved away from this detector. This, combined with the low power draw of the sensors and lack of required cooling, allows for them to be made very thin. This thinness is important because it reduces the amount of material on which particles might scatter, enabling a more accurate reconstruction of the particle tracks. This detector is expensive, and has a large number of channels to be readout, but is necessary in such a high-luminosity environment.

The SVD consists of four layers of double sided silicon strips, arranged in concentric cylinders. The outer three layers deviate from cylindrical in the forward direction, sloping inwards to cover more of the forward solid angle with the same amount of detector material. This region is important because of the forward boost, as discussed earlier in Chapter 2, and without sloping would require a longer SVD. The strips are double-sided with one set of strips that run along the z-axis, and one set that wraps around in the ϕ direction. This setup reduces significantly the number of readout channels, while still providing 2D information; when two strips that overlap record hits, their overlap must be the location of the hit. However, this assumption is no longer valid when a high percentage of strips are hit during one event, and this technology can only be used in regions where this is less of a concern.

The CDC is a drift chamber, which is the main tracking system at Belle II. It is designed to detect the paths of charged particles and permit their reconstruction in 3D. This track reconstruction allows precise measurements of the momenta of the charged particles based on the curvature of those tracks. The CDC is a large gas-filled chamber that contains nearly 15000 sense wires. Each wire is in one of two orientations, either axial, along the magnetic field lines, or stereo, which means skewed relative to the axial wires. When charged particles travel through the CDC they ionize the gas, and the ionization charges drift to the sense wires, which record the pulse in charge. The axial and stereo wires together provide enough information to reconstruct 3D position by forming a grid. The drift time of the charges to the various wires is also taken into account, which allows precise tracking.

2.2.1 Track reconstruction

Pattern recognition algorithms are used to build track candidates in the PXD and SVD together, and separately in the CDC. These algorithms consider information such as the location and timing of the hits in the various detectors. The track candidates from the two systems are then extrapolated, and if they appear compatible based on this extrapolation, they are merged.

The track candidates are then curve fit, allowing the determination of the momenta, and the point of closest approach (POCA) to the IP. Other track quantities that are available during analysis include the transverse momentum, and the number of CDC hits, n_{CDC}.

2.3 K_L^0 and muon detector

The K_L^0 and muon detector (KLM) is the outermost detector and is designed to detect K_L^0 and muons, hence its name. Similar to the ECL, the KLM is split into three sections: the forward endcap, barrel, and backward endcap. The KLM covers the entire ϕ range in the angular range of $18° < \theta < 155°$. Unlike the ECL however, there is no gap in coverage between the barrel and endcaps, and they overlap significantly in coverage to ensure this. The barrel contains 15 layers of detector material alternating with iron plates arranged in 8 sections, forming in an octagonal prism

around the solenoid and ECL. The endcaps consists of 14 layers of detection material alternating with iron plates, and these are arranged such that they cap the barrel KLM, as shown in Fig. 2.1.

The KLM uses two different detection subsystems, one carried over from Belle, and one that is designed for the higher-luminosity environment of Belle II.

The resistive plate chamber (RPC) is the technology used by Belle, and in Belle II it comprises the outer 12 layers of the barrel. They consist of two glass parallel plate electrodes separated by gas. Particles ionize the gas as they pass through it, discharging the plates in that location. This discharge is then recorded. Due to the discharge and the subsequently required charging of the plates, RPC detectors have a large dead time between particle passages. This means the efficiency of RPC detectors drops significantly when they are exposed to high particle incidence rates, and they can only be used in areas of the detector that sees fewer particles. The inner layers of the KLM are exposed to a large amount of beam background, and the endcaps see a large neutron background due to e^-e^- scattering interacting outside of the detector.

For these regions of higher particle incidence, scintillator strips are used. Each layer of detector material is comprised of two planes of strips which are orthogonal and layered on top of each other. The strips are read out by silicon photomultipliers in groups of 4, and if more than one strip in the group of 4 registers a hit, all strips in the group of 4 are considered hit. This is called a multi-strip hit, and this behaviour is caused by the current firmware and is not the intended long-term function.

While not the primary purpose of the detector, the KLM does detect photons that have passed through the ECL, and can be used as a backup photon detector. This will be discussed further later in this thesis.

2.3.1 Building KLM clusters

The first step in making a KLM cluster is to build 1D hits in the scintillator layers. 1D hits are composed of hit scintillator strips, and often contain only 1 strip. They may contain multiple hit strips if they are neighbouring strips, are not from the same group of 4 readout strips (otherwise it would be a multi-strip hit as defined earlier), and have times that are close together. At this stage, instead of being used,

17

all multi-strip hits are entirely ignored by the reconstruction software. This will be changed in future software releases.

After building 1D hits, 2D hits are constructed by combining overlapping 1D hits. These 2D hits have the position of the location of the overlap of the strips, and a time consisting of the average of the 1D hits.

The 2D hits from each layer of the KLM are then used to reconstruct KLM clusters based on their relative positions. Note that in the KLM there is only a magnetic field in the iron plates, as they act as the return flux for the solenoid that generates the magnetic field for the core of the detector. This means that even charged particles do not curve between the iron layers, and instead travel in straight lines. The 2D hits must be in a shape consistent with this behaviour to form a KLM cluster.

2.3.2 Variables

The KLM provides a variety of quantities which can be used in event reconstruction or analysis. Those quantities that are used directly in this thesis are briefly described below.

KLM clusters contain the following pieces of information: the number of layers involved in the cluster, n_K, the innermost layer in the cluster, I_K, the timing of the cluster, t_K, and θ and ϕ location information. Of these, the timing of the cluster needs to be discussed further. While KLM timing information has been collected throughout the entirety of Belle II running, it has only recently been calibrated. Previous to this calibration, it could not be used for analyses. The timing for a KLM cluster is simply the earliest time that any one of its layers recorded. This is not ideal, however, as the timing could be more precise if it were a combination of the information from all the layers involved in the cluster.

2.4 Particle identification

The particle identification system at Belle II consists primarily of two detectors: one in the barrel, and one in the forward endcap. In the barrel, the time-of-propagation (TOP) counter is located between the CDC and the ECL. The TOP counter is composed of 16 quartz bars connected to multi-anode photon detectors.

It uses the location and timing of Cherenkov photons (photons emitted by particles when they are travelling faster than the local speed of light) as they interact with the photon detectors. The photons are reflected inside the crystal through total internal reflection until they reach the photon detectors. The photon detectors then measure the location and incidence time of the photons at the end of the quartz bars. The angle of the cone of Cherenkov radiation in a medium is dependent on the speed of the particle. Steeper angles require more internal reflections to reach the photon detectors, thus taking longer to reach them.

In the forward endcap, the detector is the aerogel ring-imaging Cherenkov (ARICH). It is also located between the CDC and the ECL, with the TOP counter extending around the ARICH until its far end. The ARICH comprises two layers of aerogel with different indices of refraction. The aerogel causes particles to emit Cherenkov radiation, much as the TOP counter does. The ARICH allows the Cherenkov rings to spread out, and land on an array of photon sensors.

Both detectors provide a measurement of a particles' speed. This measurement is then combined with the measurement of its momentum by the CDC to give a mass hypothesis, and therefore a hypothesis for the particles' identity.

This information is then combined with the information that other subdetectors are able to provide: the SVD and CDC measure specific ionization which is useful for hadron identification, while the ECL and KLM provide extra information for identifying leptons. Neutral particles meanwhile get all their particle identification information from the ECL and KLM. All of the information gathered is then combined to give the probability that a particle has a certain identity.

2.5 Triggers and data acquisition

The trigger system is responsible for recognizing events that are of interest, and, in tandem with the data acquisition (DAQ) system, recording them. It is a two-level system that utilizes hardware for a fast initial trigger, and software for a slower, more refined check.

The level 1 (L1) trigger is the hardware-based trigger, and uses field programmable gate arrays (FPGA) to take information from all the subdetectors and decide whether to trigger on the event or not. If the L1 trigger activates, the DAQ

19

system takes the output from all of the subdetectors and sends it to the high level trigger (HLT) system. The HLT system is a computing cluster composed of thousands of CPU cores, which rapidly performs event reconstruction. This real-time process allows an accurate determination of whether the event is of interest. At this stage, the event is either discarded, or stored permanently. The L1 trigger system is designed to be capable of an output rate of 30 kHz, while the HLT reduces the rate to a maximum of 1.4 kHz.

To determine if an event is of interest, it is compared to a list of triggers. Triggers are a list of criteria relating to physics that Belle II is interested in. For this thesis, there are several triggers of interest, a few of which are often referred to as the single-photon triggers.

For L1 the triggers of interest are:

- hie: At least 1 GeV total in the ECL crystals with $4 \leq$ thetaID ≤ 58. The event does not appear Bhabha-like.

- lml6: Exactly one ECL cluster with CMS energy, $E^* > 1$ GeV within $13 \leq$ thetaID ≤ 58, and no other cluster with laboratory frame energy $E > 0.3$ GeV anywhere in the ECL.

- lml13: Exactly one ECL cluster with $E^* > 0.5$ GeV within $21 \leq$ thetaID ≤ 44, and no other cluster with $E > 0.3$ GeV anywhere in the ECL.

- lml16: Identical to lml13, but there must also be no tracks in the event, as defined by the L1 trigger, not by reconstruction. This trigger did not exist for some of the earlier data, but lml13 did. As a result, both are used for full data coverage, despite lml16 being a subset of lml13, because lml16 is more useful in this analysis.

The HLT triggers of interest are:

- 1: At least one neutral ECL cluster with $E^* > 2$ GeV in $32° < \theta < 130°$. Event does not appear to be a $e^+e^- \to \gamma\gamma$ or Bhabha event.

- 2: Exactly one photon-like ECL cluster with $E^* > 1$ in $45° < \theta < 115°$. No other $E^* > 0.3$ GeV ECL clusters.

- 3: Exactly one photon-like ECL cluster with $E^* > 1$ in $44° < \theta < 98°$. No other $E^* > 0.3$ GeV ECL clusters.

For more details on the HLT and L1 triggers above, see Appendix A.

2.6   Software

Data processing and event reconstruction at Belle II is done with the Belle II Analysis Software Framework (basf2). This framework is written in C++ and Python, and is used to perform a variety of tasks including simulation, reconstruction, and analysis [23]. For analysis, basf2 is interacted with through Python. ROOT [9] is used for the storing, input, and output of data at all levels.

A version of basf2, called gbasf2 (grid basf2) is used on the Belle II grid, a distributed computing system. The grid has a hierarchical structure for data storage and processing, and is designed to handle the large amounts of data and computation required by Belle II [17].

Chapter 3

The dark photon

In this thesis, part of a search for dark matter is presented. The dark matter in this search is described by one particular model, that of the minimal dark photon. In this model, the dark photon, denoted by A', is a gauge boson of and mediator of a dark force analogous to the electromagnetic force [16]. This model does not assume that there is only one particle explaining dark matter; on the contrary, it requires the existence of a dark sector. The lightest dark matter particle will be denoted by χ. This chapter explains the theory behind the dark photon model, and discusses the production and decay of dark photons, as well as the parameter space and current exclusion limits.

3.1 Theory

There are several constructions of the dark photon model, with some versions having massive dark photons while in others the dark photons are massless. This section describes only the massive case. Throughout, when choices are made that differentiate this dark photon from other possible choices, it will be noted.

In this version of the dark photon model there is a broken dark U(1) gauge symmetry, and the corresponding dark field strength tensor mixes with the Standard Model U(1) hypercharge field strength tensor [16]. In other dark photon constructions, the mixing can be with the Standard Model U(1) electric charge group instead of the hypercharge group. For the massive dark photon, this changes the

physics of the dark photon [14].

In the description of dark sectors in Sec. 1.2, it was mentioned that the way that dark sectors interacts with Standard Model particles is called a portal. Given that in this model, the dark sector mediator that interacts with Standard Model particles is a gauge boson, the portal is the vector portal. For the dark photon the portal is described by the coupling of the dark photon to the Standard Model electromagnetic current, J_{EM}^{μ}. The Lagrangian formalism for the portal is

$$\mathcal{L}_{\gamma A'} \supset e \varepsilon A'_{\mu} J_{\text{EM}}^{\mu}, \tag{3.1}$$

where e is the normal electromagnetic coupling constant, ε is the strength of the mixing, and A'_{μ} is the dark photon gauge field [22]. Note that this means the coupling of the dark and regular photons is not quantized, and is instead the arbitrary, though presumably small, $e\varepsilon$. The Lagrangian contains terms in addition to the portal term, and these come — along with the portal term — from the diagonalization of the gauge and kinetic terms after electroweak symmetry breaking. The diagonalization procedure can be seen in [14], starting from the general kinetic terms in a Lagrangian for two Abelian gauge bosons. The relevant terms in the Lagrangian are then

$$\mathcal{L}_{\gamma A'} \supset -\frac{1}{4} F'_{\mu\nu} F'^{\mu\nu} + \frac{1}{2} m_{A'}^2 A'^{\mu} A'_{\mu} + \varepsilon e A'_{\mu} J_{\text{EM}}^{\mu} + \mathcal{L}_{A'\chi\chi}, \tag{3.2}$$

where $F'_{\mu\nu}$ is the dark field strength tensor, and $m_{A'}$ is the mass of the dark photon [16]. This mass is obtained from the Stueckelberg Lagrangian [14]. To keep this model more general, the exact form of the interaction of the dark photon with dark matter is not specified, and those terms are left as $\mathcal{L}_{A'\chi\chi}$.

3.2 Production and decay

Due to the coupling of the dark and Standard Model photon, dark photons can be produced by any mechanism that produces a virtual photon with sufficient mass. This of course opens up many potential avenues of production for dark photons at particle colliders. With Belle II, the best production mechanism is the annihilation of the $e^{+}e^{-}$ pair, and this is the case studied in this thesis.

The dark photon can decay to both dark matter and Standard Model particles, because of its coupling to the electromagnetism (EM) current. The coupling to the Standard Model is suppressed by ε however, so it assumed that if it is kinematically allowed ($m_{A'} > 2m_\chi$, where m_χ is the mass of the lightest dark matter particle), the dark photon will preferentially decay to dark matter. This statement can be made more precise by looking at the partial decay widths of the dark photon.

For the decay of the dark photon to Standard Model leptons, the partial decay width is

$$\Gamma(A' \to \ell^+\ell^-) = \frac{1}{3}\alpha\varepsilon^2 m_{A'} \sqrt{1 - \frac{4m_\ell^2}{m_{A'}^2}} \left(1 + \frac{2m_\ell^2}{m_{A'}^2}\right), \tag{3.3}$$

[14] where $\ell = e, \mu, \tau$, m_ℓ is the mass of the corresponding lepton, and α is the fine structure constant. This decay can only occur if $m_{A'} > 2m_\ell$, for whichever lepton is being considered. The partial decay width of the dark photon to hadrons cannot be calculated directly, but can be determined through empirical measurements of the ratio of the cross sections of e^+e^- to hadrons and e^+e^- to muons. This ratio is denoted as $\mathcal{R}$. With this you get

$$\Gamma(A' \to \text{hadrons}) = \Gamma(A' \to \mu^+\mu^-)\mathcal{R}, \tag{3.4}$$

[16] for the partial decay width to hadrons. Just as for the leptons, these decays can only occur if kinematically allowed.

The partial width for the dark photon decaying into dark matter has a similar form [14] to that of decaying into leptons:

$$\Gamma(A' \to \chi\bar{\chi}) = \frac{1}{3}\alpha_D m_{A'} \sqrt{1 - \frac{4m_\chi^2}{m_{A'}^2}} \left(1 + \frac{2m_\chi^2}{m_{A'}^2}\right). \tag{3.5}$$

The key difference is that Eq. 3.5 contains α_D, the dark sector fine structure constant, instead of ε^2 and the Standard Model fine structure constant. These each quantify the the strength of their respective force between elementary charged particles. The result of this difference in the partial decay width formulas is that the decay into dark matter will be dominant if $m_{A'} > 2m_\chi$ and $\alpha_D \gg \alpha\varepsilon^2$. The potential values of ε will be discussed more in the next section, but it is expected to be small, of the order of 10^{-2} or smaller [14]. The value of α_D is unknown, but it is

24

not of particular interest for this analysis. A simplification will be introduced in the next section such that α_D can be ignored.

3.3   Parameters and current exclusion limits

The analysis presented in this thesis is searching for the invisible decay of the dark photon at Belle II, and so only the parameters and parameter space relevant to the invisible decay will be discussed.

The minimal model of the dark photon described above is one of the simplest dark sector models, as there are only three free parameters: the mass of the dark photon, $m_{A'}$, the strength of mixing, ε, and the branching fraction of the dark photon into dark sector particles. A simplification can be made, which is that we assume the branching fraction to dark matter is 1 unless the final dark matter state is kinematically disallowed, where the branching fraction is 0. This assumption is equivalent to assuming that $\alpha_D \gg \alpha\varepsilon^2$. With this simplification there are only two free parameters, and together these form the parameter space for the dark photon.

From analyses of the potential strength of mixing [16], a range of $10^{-6} < \varepsilon < 10^{-2}$ is the most interesting and attainable region to explore. As for $m_{A'}$, it is largely unrestricted, however, the parameter is usually split into two ranges, divided by whether the dark photon mass is greater or less than twice the mass of the electron. Only part of the upper range, $10^{-3}\,\mathrm{GeV}/c^2 < m_{A'} < 10\,\mathrm{GeV}/c^2$, is accessible at Belle II [16].

Many other experiments have conducted searches for dark photons, and have already excluded regions of the parameter space, as shown in Fig. 3.1. This figure also shows the predicted search region for this analysis at Belle II.
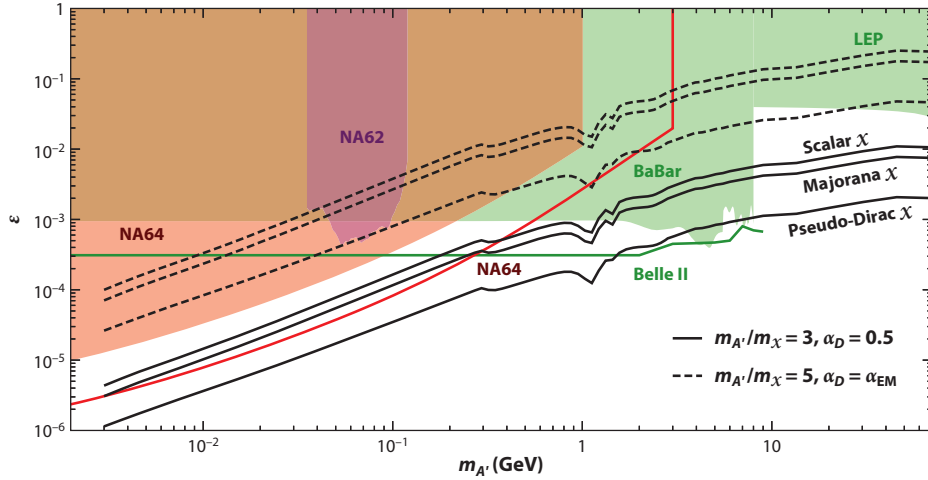
Figure 3.1: An exclusion plot for the minimal dark photon decaying invisibly. The exclusion plot is in the parameter space formed by the mixing parameter and the mass of the dark photon. The filled-in regions are excluded by the labelled experiment. The coloured lines are projected exclusion limits, and the black dashed and solid lines represent the parameters for which the labelled model is compatible with the amounts of dark matter observed in the universe. These compatibility lines are dependent on the ratio of the dark photon and dark matter masses and α_D. The Belle II projection is for $20\,\text{fb}^{-1}$, less that 1/20 of the current dataset. This projection has however been determined to be overly optimistic. Figure from [16].

Chapter 4

Analysis structure

The single-photon analysis is an analysis being conducted at Belle II in search of dark photons. Specifically the analysis is searching for the invisible decays of the massive dark photon described in Chapter 3.

4.1 Overview

When the dark photon is produced by e^+e^- annihilation and decays invisibly, the process is entirely undetectable if there are no other particles involved. While Belle II is able to measure missing energy and mass, this cannot happen for entirely undetectable processes, because there's no indication anything happened at all. The events are simply not stored. In order for this to be an event that could be studied, there must be a detectable particle in the event, such as an initial-state radiation (ISR) photon. This requirement gives rise to the name of this analysis: the single-photon analysis. The Feynman diagram for this interaction is shown in Fig. 4.1.

The signal for the invisible decay of a dark photon is a narrow peak in a smooth background of the distribution of the missing mass of the event, also called the recoil mass. This recoil mass corresponds to the mass of the dark photon.

Belle II is well suited for this analysis because of the large amount of the solid angle it covers, the known initial state, and the dedicated single-photon triggers. As previously discussed in Chapter 2, Belle II has several single-photon triggers that
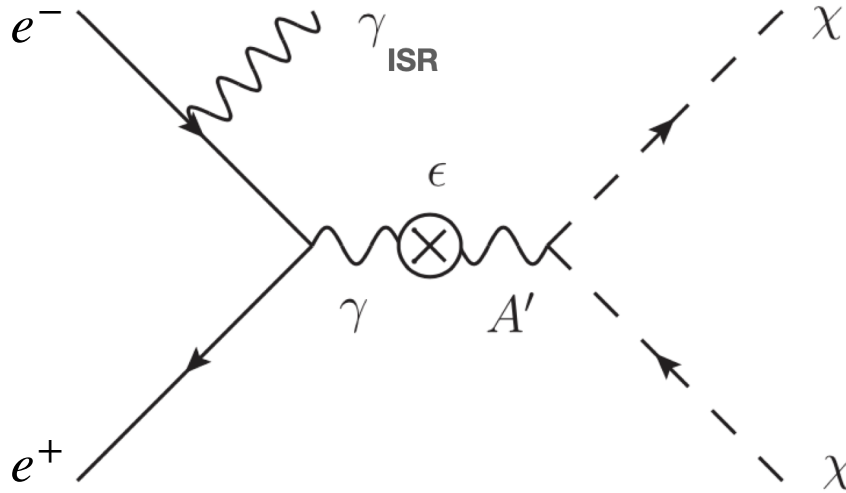
Figure 4.1: A Feynman diagram of the signal event for the single-photon analysis. A virtual photon is produced by e^+e^- annihilation, which then kinetically mixes with the dark photon with coupling ε. The resultant dark photon then decays invisibly to dark matter, represented by χ. Modified from [31].

store events where there is a lone, high-energy photon. These triggers are essential to this analysis.

4.2 Backgrounds

Events that are not caused by dark photons are sometimes able to mimic the appearance of a single-photon event. These events are called background events. The main sources of background are listed here along with a brief description:

- Radiative Bhabhas: Bhabha events are the scattering of the e^+e^- pair, and are extremely common at Belle II. The term radiative Bhabha means a photon is emitted as well: $e^+e^- \rightarrow e^+e^-\gamma$. If two out of three of the resulting particles are not detected due to detector inefficiency or detector acceptance, the remaining particle can cause an ECL cluster that could constitute a viable single-photon cluster. In this case, the event then imitates a single-photon

28

event. This happens for only a tiny fraction of radiative Bhabha events, but because their cross section is so high, they are an important background.

- $\gamma\gamma(\gamma)$: these events are simply $e^+e^- \to \gamma\gamma(\gamma)$, and can imitate single-photon events when all but one of the photons are missed or are out of acceptance.

- Cosmic rays: these events are caused by cosmic rays that pass through the detector. These particles trace one path through the detector, and might leave only one ECL cluster of significant energy. The tracks in these events do not generally pass through the IP. These events also typically have a KLM cluster with many layers, which can be useful in rejecting them.

- Beam background: this is described in Chapter 2. Since beam background is the term for many processes there isn't one particular way that these events mimic signal. In general, as in the other cases, only one particle leaves a significant ECL cluster.

The single-photon analysis is complex due to the difficulty of characterizing these backgrounds [14]. Each background requires careful study and construction of vetoes to remove as much of it as reasonably possible.

4.3 Structure of the analysis

Due to its complexity, the single-photon analysis is broken into components which are then completed by the analysis team. The components are described in the following subsections.

4.3.1 Study of signal

While the event signature for this analysis is an event that contains just one photon, that does not mean events that have absolutely anything else in them will be rejected. True single-photon events could also contain tracks, extra photons, or KLM clusters caused by beam background, noise, or any one of a number of processes. In order to determine what single-photon events actually look like, it is necessary to study a channel that can stand in for the signal, along with signal Monte Carlo (MC). The signal proxy has the advantage of being available for both data

and MC, while the signal MC represents the exact events of interest, but is clearly not available for data. Radiative dimuon events were chosen as the signal proxy because they are clean, and well understood. The radiated photon in these events will represent the single-photon. Signal studies also allow the investigation of the shape of the distributions that will be used in signal extraction.

4.3.2 Study of backgrounds and veto construction

The major backgrounds listed in Sec. 4.2 all need to be studied in detail. The purpose of this is twofold: in combination with the characteristics of the signal events, vetoes can be constructed to significantly reduce the backgrounds; to study the shape and scale of the distributions that will be used in signal extraction.

4.3.3 Data-MC corrections

MC does not represent data perfectly, and because much of the analysis is conducted using MC to keep the analysis blind, correction factors are needed. These correction factors are particularly important when calculating the inefficiency of the ECL and KLM, as small changes in how often these subdetectors fail to detect particles can have a large impact on how many background events are let through.

4.3.4 Fitting procedures and signal extraction

In the single-photon analysis, the signal will be fit and extracted in two regions, each treated slightly differently. Both regions will use the recoil mass squared m_R^2, which is related to the centre-of-mass energy of the ISR photon, E^*, by the formula

$$m_R^2 = \sqrt{s}\left(\sqrt{s} - 2E^*\right), \tag{4.1}$$

where $\sqrt{s}$ is the CMS collision energy. As mentioned earlier, the mass of the dark photon corresponds to the recoil mass, and so $m_{A'} = m_R$. This allows Eq. 4.1 to be modified and rewritten as

$$E^* = \frac{\sqrt{s}}{2} - \frac{m_{A'}^2}{2\sqrt{s}}, \tag{4.2}$$

where it is clear that E^* is dependent on $m_{A'}$, which is fixed, and $\sqrt{s}$, which has several different values throughout data taking at Belle II. This makes fitting m_R^2

superior to fitting E^*.

The two fitting regions and their corresponding methods are:

- When the single-photon E^* is below $2\,\text{GeV}$, the signal will be fit from the 1D distribution of the recoil mass squared, m_R^2. This was chosen because it is extremely difficult to quantify the magnitude of the radiative Bhabha background in this energy range. The background distribution is expected to be smooth however, which should allow the 1D fit to work effectively.

- When the single-photon E^* is above $2\,\text{GeV}$, the signal will be fit from the 2D distribution of m_R^2 as a function of the thetaID. This allows for excellent separation of the backgrounds and signal, if the shape and magnitude of the background distributions can be quantified, which is expected to be possible.

4.3.5 Systematic uncertainty estimation, unblinding, and setting upper limits

These are the final components of the analysis and are necessary steps. Unblinding refers to the analysis, specifically the signal analysis, finally being run on the actual data instead of the simulated data. Simulated data is used to prevent accidental biases in the analysis, but the the final result must, of course, be based on the data. Since other components need significant work, no specifics of this will be given here. It will follow the normal procedures in Belle II, as laid out in [24].

The study of the signal proxy and the radiative Bhabha background, and the construction of the associated vetoes is presented in the next chapter.

Chapter 5

Analysis

This chapter presents vetoes to be used in the single-photon analysis that involve KLM clusters, ECL clusters, and tracks. These vetoes are designed to veto the events when we detect potential particles present in the event besides the single photon itself. Radiative dimuons are a well-defined event type that both allow us to study the background signals in the detector by looking at what happens aside from the photon and muon pair, and act as a proxy for single-photon events in data and MC. When being used this way, the radiated photon is referred to and treated as the single photon. Due to the utility of radiative dimuon events, a clean control sample was constructed of these events to make use of their abilities.

A significant area in which data and MC disagree is that of the KLM response to high-energy photons. This is particularly important because the single-photon analysis will use the KLM as a backup photon detector. The radiative photons in the radiative dimuon control sample allow us to study a pure sample of high-energy photons, which is useful in characterizing the response in the KLM and ECL for both data and MC. While radiative dimuons can be used as a signal proxy, the other control sample used is composed of radiative Bhabhas, one of the major backgrounds.

In the following sections we will go through the datasets used, the construction of the control samples, and the vetoes proposed by use of them. Unless otherwise specified, all quantities discussed in this chapter are measured in laboratory rest frame. All histograms in this chapter include an information tab that provides vari-

ous data. This data includes the number of entries in the entire parameter space (not just those in the subspace displayed), the mean and standard deviation of the relevant axes, and the integral of displayed plot entries. Additionally, the tab presents overflow and underflow numbers, which for 2D histograms are eight individual numbers that indicate the axis in which events are in overflow or underflow.

5.1 Datasets used

This analysis uses data and MC simulated data from the Belle II collaboration. The data and MC samples used are described in more detail below.

5.1.1 Data

Belle II has been collecting data since 2019, and has amassed a dataset of almost $432\,\text{fb}^{-1}$. However, the single-photon triggers were not active for the first few data taking sessions, and so the dataset available for this analysis is $425\,\text{fb}^{-1}$. All of the data used was taken in 2020–2022. These data comprise primarily data taken with the CMS collision energy at the $\Upsilon(4S)$ resonance, but also contain data taken off-resonance, and some taken at various energies near the $\Upsilon(5S)$ resonance. Table 5.1 shows the breakdown of the data used in this analysis by the collision energy at which it was collected.

Table 5.1: The CMS collision energies at which the data was collected. For each energy, the corresponding amount of data used in this analysis is listed. The total amount of data used is also listed.

CMS **collision energies**	Size $\left(\textbf{fb}^{-1}\right)$
$\Upsilon(4S)$	363.4
$\Upsilon(4S)$ off-resonance	42.3
Various energies near $\Upsilon(5S)$ resonance	19.4
Total data used	**425.2**

5.1.2 MC

MC is produced centrally at Belle II for all analysts to use. The MC simulation simulates the e^+e^- collisions, the resulting particles, and their interactions with

the detector. The electronic response of the detector to those particles is also fully simulated and then processed and reconstructed with the *same* software that is used for data. Non-specialized MC that is intended for broad use may be referred to as generic MC. There is a campaign associated with each basf2 release, with the most current being campaign 15. There are two types of MC: run-independent, and run-dependent. Run-independent means that the backgrounds are simulated, and the MC does not depend directly on the data. Run-dependent means that the background is from the data, and the MC is split into sections that correspond to when in the data that background is from. Run-dependent is the superior type of MC, as it more accurately represents data compared to run-independent MC. This analysis uses only run-dependent MC from campaign 15, which is denoted as MC15rd. Only the part of MC15rd that corresponds to the data with single-photon triggers is used.

Due to its simulated nature, MC is split into event types. In this analysis, the e^+e^- and $\mu^+\mu^-$ samples are used. While run-dependent MC uses the backgrounds from data, and corresponds to particular parts of the dataset, it does not generally have the same luminosity. The e^+e^- MC15rd sample has one tenth the luminosity of data, whereas the $\mu^+\mu^-$ sample has four times the luminosity of data.

As will be noted again later, the regular MC15rd Bhabha samples require that both of the scattering MC electrons have θ values that are in ECL acceptance. This generation requirement is quite relevant for this analysis.

5.2   Radiative dimuon control Sample Selection Criteria

The selection criteria for the radiative dimuon control sample must make sure that the events in the sample are actually radiative dimuon events, while preserving sufficient statistics, and not inadvertently biasing the sample by unnecessarily removing events that are relevant. The following sections go through the various categories of requirements.

5.2.1   Muon requirements

Both muons must pass the criteria listed in Table 5.2. These parameters and values were chosen based on their use in another Belle II analysis [28]. Several require-

ments that were included in that analysis were excluded here, due to the different goals of this work. One requirement which has been added is a cut on L_μ, which is the likelihood that the particle is a muon. L_μ is calculated using information from the particle identification system. The L_μ cut is loose, however when the L_μ for the muons in the pair is plotted in Fig. 5.1, it can be seen that this requirement is sufficient to require that virtually all events have at least one muon with a L_μ greater than 0.95. Due to leakage and gaps in the KLM among other reasons, the L_μ for one muon can be low while the other is high, and this pair is with high probability a muon pair, which is why these events are kept.

5.2.2 Event requirements

The control sample events should contain only one ISR photon and the muon pair. To achieve this we make cuts on the square of the mass recoiling against the dimuon system, m_R, and on the recoil momentum of the dimuon system, p_R. In single-ISR events, there should be no recoil mass, and the distribution would be entirely concentrated at zero. However, primarily due to finite resolution, while the distribution for m_R^2 is peaked at zero, it exhibits a non-zero width. Reconstruction error and the limits of resolution should cause equal smearing in the positive and negative directions, but situations such as a double-ISR could cause there to be a small recoil mass due to their non-zero invariant mass. Some events of this type will be events we want to keep, and as such, the range of acceptable values should be biased in the positive direction. The chosen range of acceptable values is $-0.25\,\mathrm{GeV}^2/c^4 < m_R^2 < 1\,\mathrm{GeV}^2/c^4$. Figure 5.2 shows the m_R^2 distribution for the control sample with this cut enacted. This distribution can't be seen without this cut since it is implemented at an earlier stage of data analysis, and is one of several cuts that reduces the sample to a manageable size.

To ensure that there is an ISR photon of the energy we are interested in, we require a recoil momentum of at least $0.5\,\mathrm{GeV}/c$. The remaining recoil momentum distribution can be seen in Fig. 5.3. Ideally this recoil momentum should all be due to the photon, however this and the m_R^2 criteria are not enough to guarantee this, and in the next subsection we will add some selection criteria to select events where this is true.
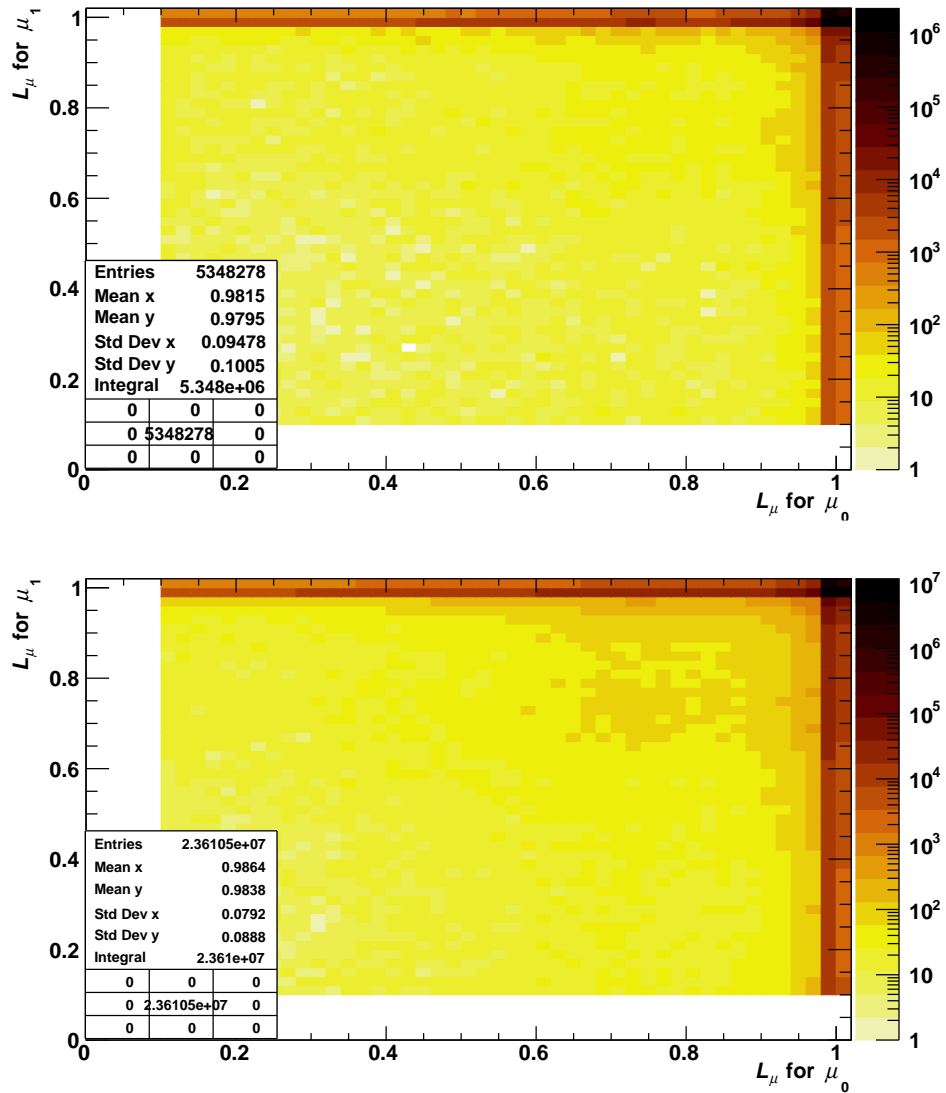
Figure 5.1: Log plot of the L_μ of the two muons, μ_0 and μ_1, for data (top), and MC (bottom). These plots have the whole radiative dimuon control sample selection criteria applied, which includes a requirement that both muons have $L_\mu > 0.1$. It can be seen that with this requirement there are very few events in the sample that have a poor L_μ for both muons.
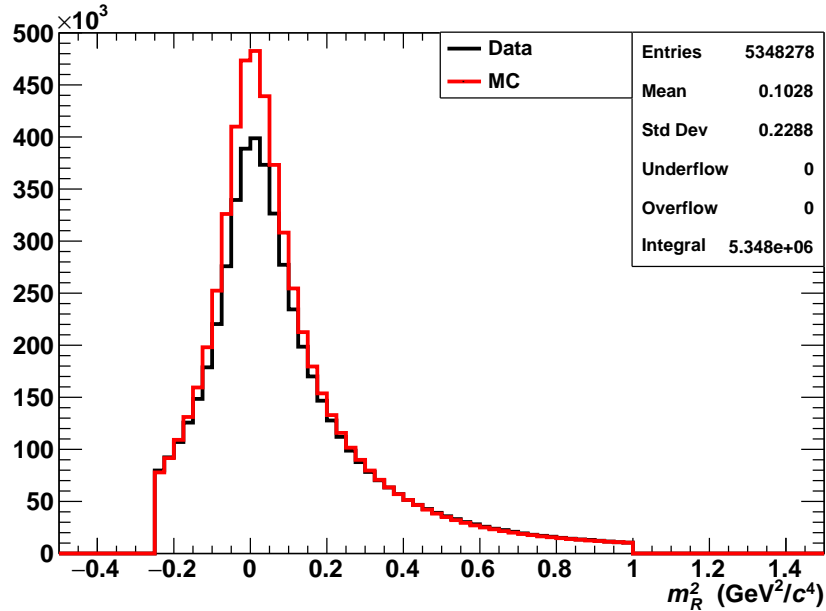
Figure 5.2: The distribution of the square of the mass recoiling against the dimuon system. MC is normalized to data by luminosity and the information tab is for data. The distribution is curtailed at $-0.25\,\mathrm{GeV}^2/c^4$ and $1\,\mathrm{GeV}^2/c^4$, as this is the distribution with all control sample criteria applied. The distribution is peaked very near zero as expected, and is somewhat asymmetric with the bins on the positive side consistently containing more entries than their negative counterparts.

A summary of the event requirements is given in Table 5.2.

5.2.3 Photon requirements

The criteria applied thus far are not sufficient to achieve a very clean control sample, but this can be greatly helped by checking if there is a photon corresponding to roughly what is expected based on the recoil momentum: a recoil photon. The term recoil photon will be used interchangeably with the term single photon SP for radiative dimuon events. If a recoil photon cannot be matched to the recoil momentum, the event will be discarded. The matching and other photon criteria are
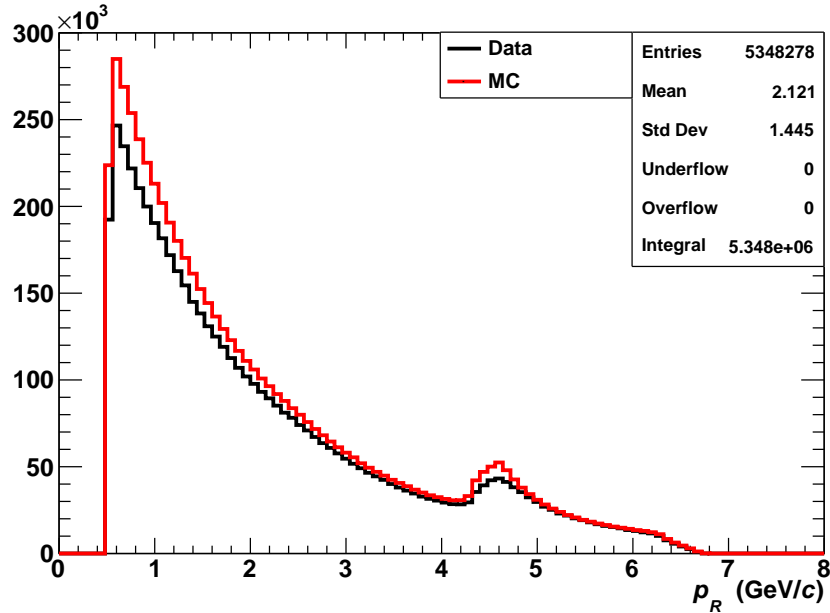
Figure 5.3: The distribution of the recoil momentum against the dimuon system for both data and MC. MC is normalized to data by luminosity and the information tab is for data. The distribution is cut at $0.5\,\mathrm{GeV}/c$, as this is the distribution with all control sample criteria applied. The distribution is peaked near this cutoff, which is expected since there are more radiative dimuon and other mimicking events with smaller recoil, such as lower energy radiated photons. The local maximum between 4 and $5\,\mathrm{GeV}/c$ is caused by beam energy photons.

summarised in Table 5.2.

The angle between the recoil photon and recoil momentum vectors, α_R, should be near zero when the photon is the main cause of the recoil. The momentum of the recoil photon, p_p, should also be very close to that of the recoil momentum p_R. This means the ratio of the two momenta should be close to 1. Extra ISR photons and the uncertainties in reconstruction introduce some smearing though, causing both distributions to be less sharply peaked. Figure 5.4 shows the parameter space for the momentum ratio and angular separation between the recoil momentum and recoil photon.
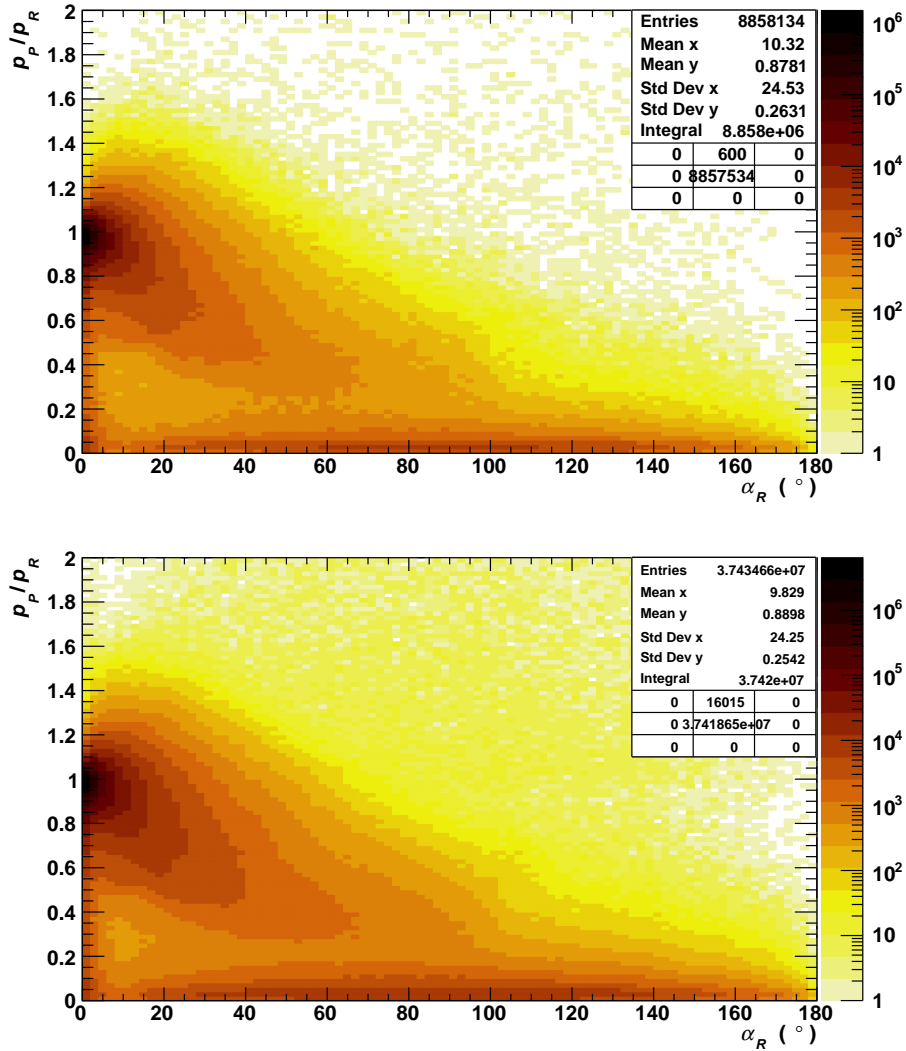
Figure 5.4: The ratio of the recoil photon momentum to the recoil momentum against the two muons vs. the 3D angle between the recoil momentum and the recoil photon, plotted for data (top) and MC (bottom). Both plots are log scaled, and were made with all control sample criteria applied, except for the criteria based on these plots. The vast majority of entries are in the region near a momentum ratio of 1, and $\alpha_R < 20°$.
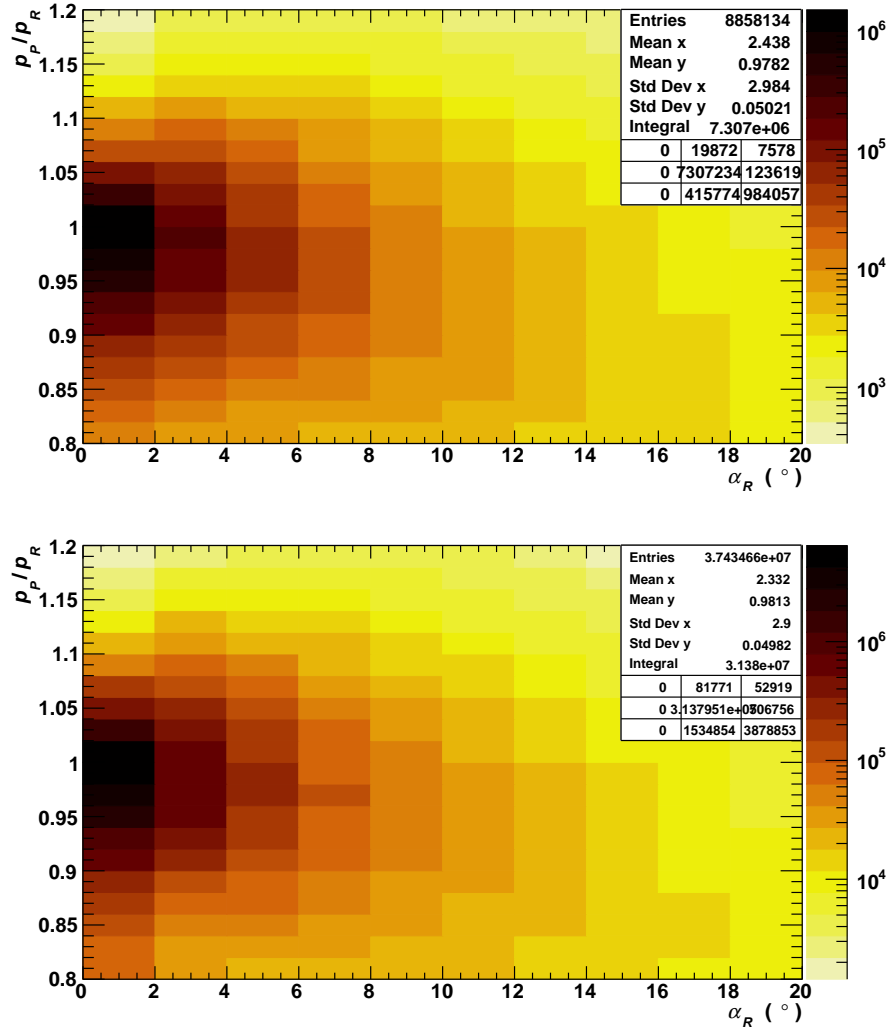
Figure 5.5: The ratio of the recoil photon momentum to the recoil momentum against the two muons vs. the 3D angle between the recoil momentum and the recoil photon, plotted for data (top) and MC (bottom). Both plots are a crop to the area of interest of the plots in Fig. 5.4. The vast majority of entries are still present in the crop, due to the large concentration at a ratio of 1 with small angular separation.

The region bounded vertically by 0.95 and 1.1, and horizontally by 0 and $6°$ contains most of the events, and Fig. 5.5 shows a crop to that area. There are two main factors that cause the spread of energy near a ratio of 1: leakage of the photons through the ECL causing an underestimation of the photon energy, and beam background causing an overestimate. While the leakage effect is stronger than the beam background one, we don't necessarily want to include events where the leakage of the single photon is significant as this could make the sample less representative of signal. There is, however, another reason for the asymmetric range around a ratio value of 1. There is an effect that is primarily present below a ratio of 0.95 that is likely caused by a relatively high-energy secondary ISR photon. These events are not desired, and might not get caught by other requirements or vetoes.

Figure 5.6 shows a clear separation of the events that likely have a high-energy second ISR photon. These plots are of the momentum ratio as a function of the 3D angular separation of the candidate recoil photon and the most energetic extra photon, where that extra photon has a lab energy of at least 250 MeV.

The two populations can be fairly well separated by a line at 0.95 for the momentum ratio. The upper distribution is what is expected from from a radiative dimuon event, where the momentum ratio is close to 1, and the angle of the recoil photon and most energetic extra photon is not correlated. The lower distribution has a strong correlation between the momentum ratio and the angular separation of the photons, which is indicative of something else going on in the event. The suspected cause of this effect is double-ISR, as most events in this group are separated by a distance too significant for it to be attributed to a clustering issue. In a clustering issue, a photon cluster gets split into two potential photons; however, this observed separation is more in line with the possibility of double-ISR. To confirm whether the energies of the photons are consistent with this explanation, the energies of the recoil photon and the most energetic extra photon in the event are summed for events within a region of the parameter space shown in Figure 5.6 where the momentum ratio is below 0.9, and the 3D angular difference is less than $90°$. The momentum ratio is then recalculated with the new combined energy value used in place of the measured photon energy. A plot of this recalculated momentum ratio can be seen in Fig. 5.7, which shows that the sum of these two photons'
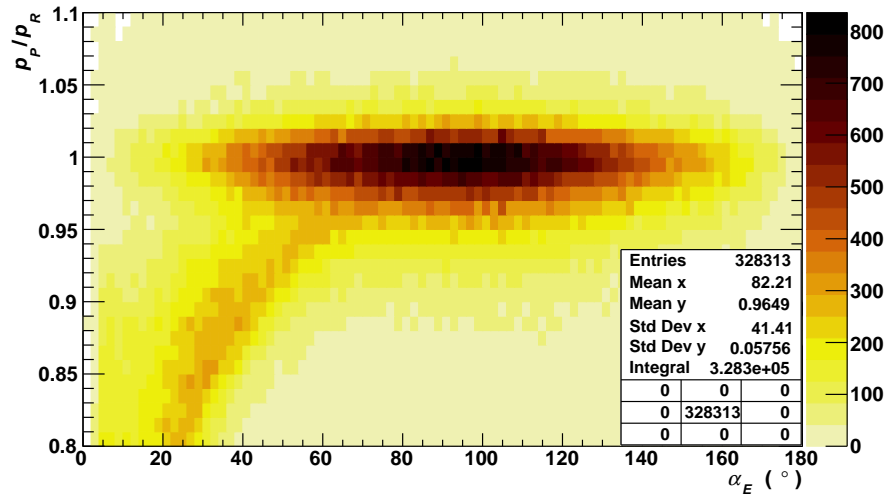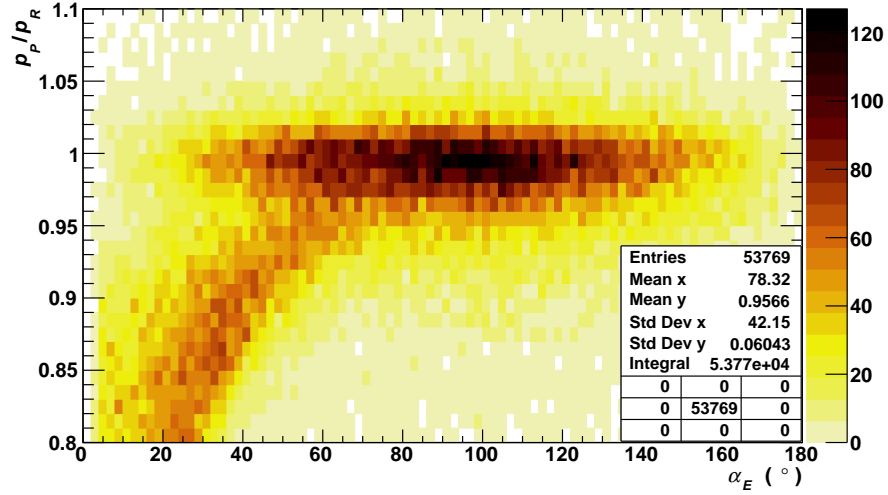
Figure 5.6: The ratio of the recoil photon momentum to the recoil momentum as a function of the 3D angle between the recoil photon and the most energetic extra photon with a lab energy of at least 250 MeV. Top is data, and bottom is MC. These were made with the control sample criteria except with a momentum ratio of 0.8 as the lower bound instead of 0.95. In both plots there are two distinct components: one group has a strong correlation between the axes, while the other does not. These two groups do overlap, though the higher concentration components can be reasonably separated by a line at $y = 0.95$.

energies produces a momentum ratio with a distribution that peaks near 1. This plot therefore supports the theory that these events have double-ISR.
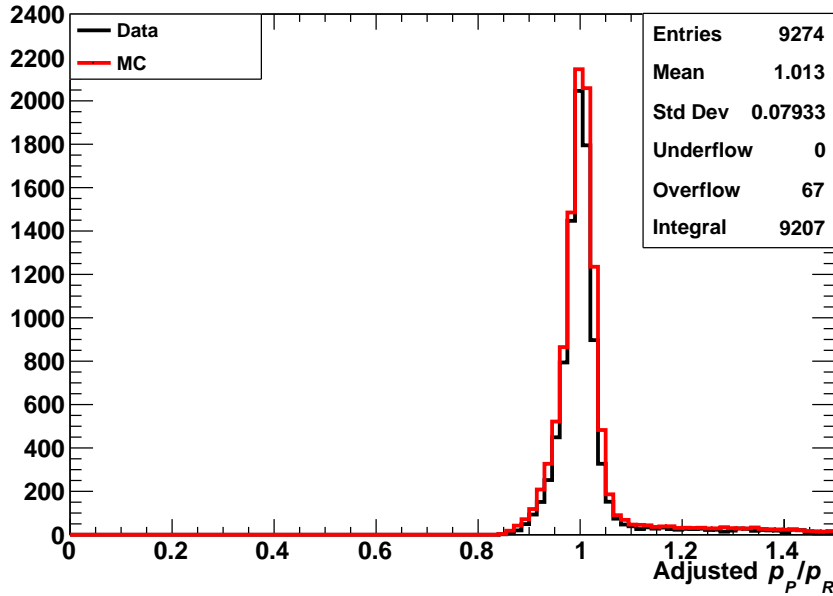
Figure 5.7: The adjusted measured photon energy divided by the recoil momentum against the two muons. Adjusted means that the energy of the most energetic extra photon was added to that of the recoil photon. This process resulted in a distribution peaked at one, indicating that these two photons combined contain the expected energy of the recoil photon. MC is normalized to data by luminosity and the information tab is for data.

The recoil photon is also required to have a θ value in the range $(36.4°, 120.1°)$ which corresponds to a thetaID range of [16, 54]. This is a subset of the barrel component of the ECL, which has a thetaID range of [13, 58]. The reason for the requirement is that the barrel is the most reliable part of the ECL, but more importantly it also increases the chances of detecting the other particles in the event such as muons or electrons if they are present since they are less likely to both go down the beam. This is most relevant for radiative Bhabha events as these disproportionately have their radiated photons at lower angle, and without this restriction to the

barrel there would be an overwhelming number of low angle radiative Bhabhas. The three crystals from both edges of the barrel are excluded as there is increased leakage there. An additional crystal is excluded on the high side for reasons that will be discussed later. The θ distribution for the recoil photon, θ_R, in the control sample is displayed in Fig. 5.8.
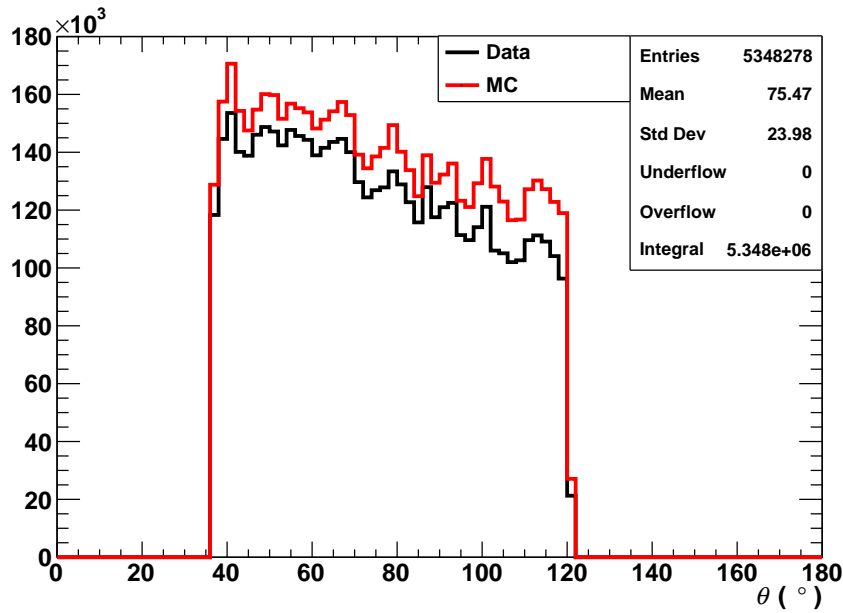
Figure 5.8: The distribution of the lab frame θ of the recoil photon. MC normalized to data by luminosity and the information tab is for data. All sample selection criteria have been applied.

In order to reduce possible contamination of the shower shape variables in the control sample, a selection is applied that requires that the photon is at least $15°$ away from either muon, as measured at the ECL. We'll use α_μ to denote this quantity.

Figure 5.9 shows that there are a significant number of events for which this is a consideration, and that the range that is excluded should be as small as possible so as to not unnecessarily veto events.

This selection is achieved by use of variables that store where the extrapolated
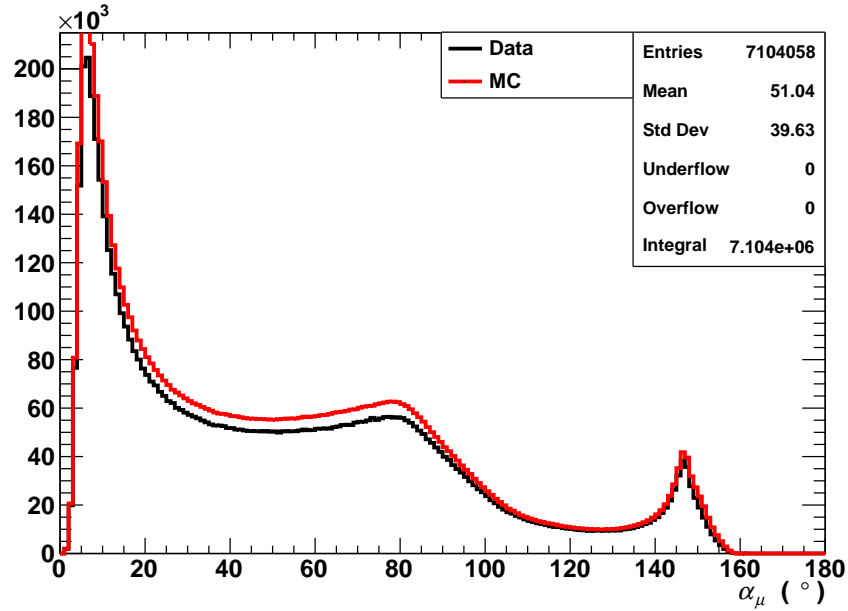
Figure 5.9: Angle between the recoil photon and the closer of the two muon tracks, measured at the ECL. MC normalized to data by luminosity and the information tab is for data. All control sample selection criteria have been applied except a cut on the angle between the recoil photon and the closer of the two muon tracks, as measured at the ECL. The peak near zero is caused by the preferential emission of the photon in the direction of a muon. It is not peaked at zero due to the path curvature experienced by the muon. The peak at high angular difference is caused by beam energy photons.

paths of the muons intersect the ECL. These locations are then compared to the location of the photon in the ECL. The extrapolation is necessary since the paths of muons curve due to the magnetic field, while those of photons do not. Additionally the muons are not required to have an associated ECL cluster, and so those cannot be used instead. The reasoning for requiring $\alpha_\mu > 15°$ is based on the geometry of the ECL: each crystal is approximately $2.5°$ wide, and a cluster is, at its largest, a 5x5 array of crystals centred on the most-energetic crystal, with the corners missing. The cluster size necessitates that there be the space of at least 5 crystals between

the centres of the clusters to prevent all overlap of clusters. $15°$ is 6 crystals wide however, and was chosen in order to be safe.

The appropriateness of this cut can be seen in Fig. 5.10, where it will remove the events with low Z_{MVA} at low angle difference, where there is a noticeable abundance of such events.

5.2.4 Selection summary and control sample plots

Table 5.2 summarizes the selection criteria for the radiative dimuon control sample.

Table 5.2: The full selection criteria for the radiative dimuon control sample. The criteria are split into their three categories corresponding to the sections in which they are described.

Category	Criteria	Explanation of variable
Muon	dr < 2 cm	Distance from IP to POCA in the x-y plane
	$|\mathrm{dz}| < 4$ cm	Distance from IP to POCA in z
	$L_\mu > 0.1$	Likelihood the particle is a muon
	$p_\mu > 2\,\mathrm{GeV}/c$	Momentum of the muon
	$n_{\mathrm{CDC}} > 4$	Number of CDC hits for the muon track
Event	$-0.25\,\mathrm{GeV}^2/c^4 < m_R^2 < 1\,\mathrm{GeV}^2/c^4$	The square of the mass recoiling against the dimuon system
	$p_R > 0.5\,\mathrm{GeV}/c$	Momentum recoiling against the dimuon system
Photon	$\alpha_R < 6°$	Angle between the recoil momentum and photon
	$0.95 < \frac{p_P}{p_R} < 1.1$	Ratio of the recoil photon and recoil momenta
	$36.4° < \theta_R < 120.1°$	Lab θ of the recoil photon
	$\alpha_\mu > 15°$	Angle between the recoil photon and the closer muon at the ECL

The first plot of interest made using this control sample is a 2D histogram of
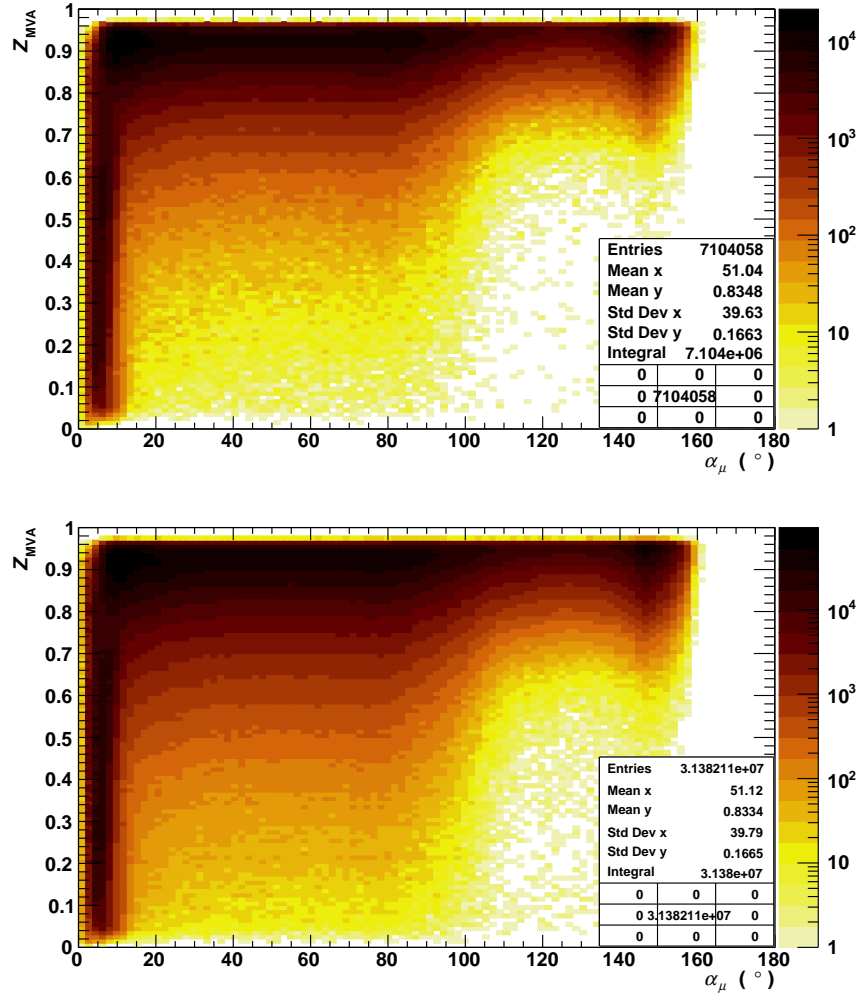
Figure 5.10: The recoil photon Z_{MVA} as a function of the 3D angle between the recoil photon and the nearest muon, as measured at the ECL. Data is shown at top, while MC is shown in bottom. All control sample selection criteria are applied except a cut on the angle between the recoil photon and the nearest muon, as measured at the ECL. Z_{MVA} ranges from 0 to 1, with higher values indicating the ECL cluster is photon-like. On the left of the plot there is a considerable concentration of recoil photons that are within a few degrees of a muon at the ECL, and that have a $Z_{MVA} < 0.7$. These photon ECL clusters were likely contaminated by the muon ECL cluster, resulting in lower Z_{MVA} values.

the single-photon E^*, the energy in the CMS frame, as a function of the thetaID of the photon. This plot is shown for data and MC in Fig. 5.11.

Also of particular interest for the single-photon analysis is the recoil mass of the event squared as a function of the thetaID of the photon. For the radiative dimuon control sample the recoil mass is specifically the mass recoiling against the radiative photon, because this is analogous to what the recoil mass is in a single-photon event. This plot is displayed for both data and MC in Fig. 5.12.

5.2.5 Selection of KLM clusters, extra photons, and tracks

Now that the events of the control sample have been selected, the extra photons, KLM clusters, and tracks that are not part of the radiative dimuon can be selected. The following sections describe the selection of these objects.

KLM clusters

The two energetic muons in radiative dimuon events should cause large KLM clusters as the KLM is designed to detect muons. However, sometimes the muon KLM clusters can look similar to those caused by high-energy photons, and are clusters that would not be present in a single-photon event. As such, in order to study the response of the KLM to single-photon events we need to ignore the KLM's response to the muons.

Since the muon-associated KLM clusters range widely in number of layers and location, the surest way to ignore them is to ignore all KLM clusters near the muons. Unfortunately the angular resolution of the KLM is far worse than that of the ECL, and so we must exclude a large angular area around each muon track when we want to look at the KLM response to the rest of the event.

To determine the angular range that safely excludes the vast majority of muons but that does not overly exclude regions of the KLM, plots of the θ and ϕ between KLM clusters and the closer muon can be made. Figure 5.13 shows these plots, from which we can see the distribution of the muon related clusters relative to the muon momentum. The angle difference in ϕ is significantly larger than that in θ due to the curling of the muons in the magnetic field, which affects only the ϕ position. This is also why ϕ and θ are used here instead of the 3D angle difference, because
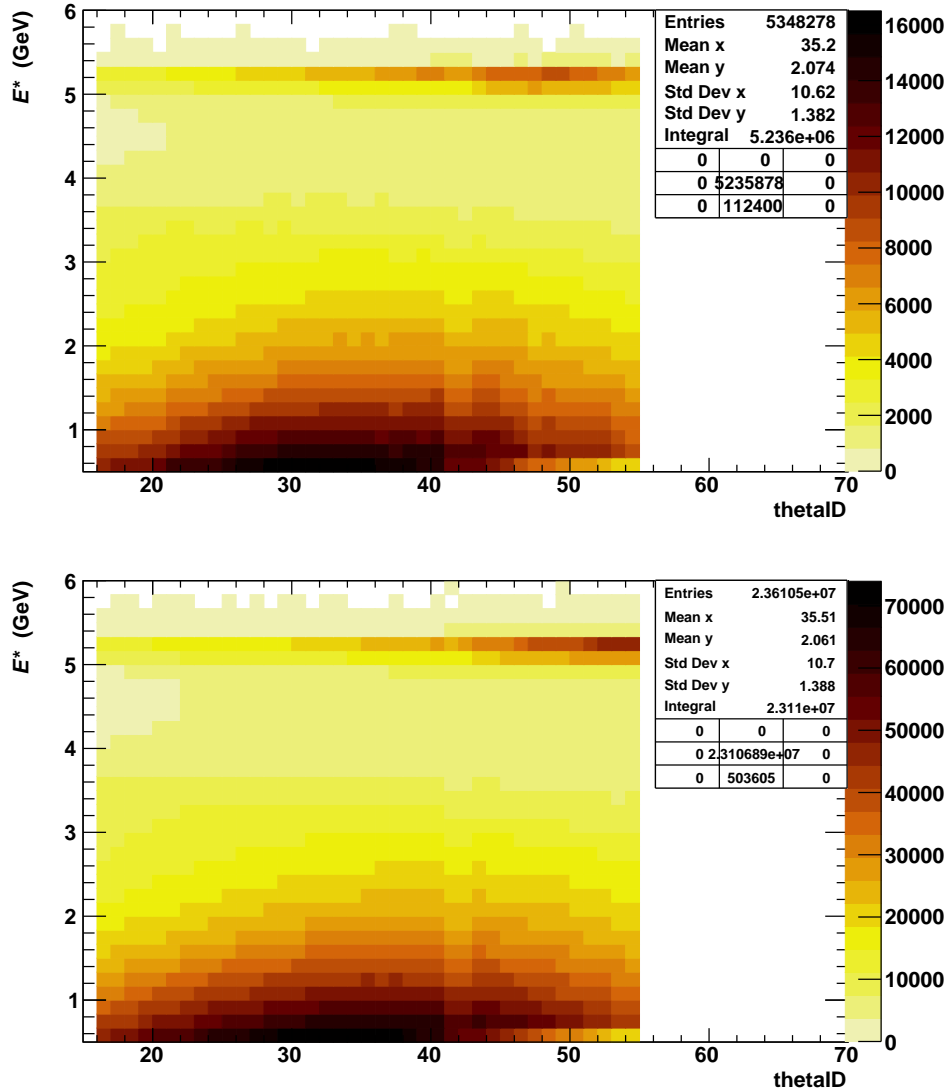
Figure 5.11: The data (top), and MC (bottom), distributions of E^* as a function of the thetaID for the recoil photon. These are made with the radiative dimuon control sample, and as such only have entries in the thetaID range of [16, 54] which corresponds to the θ requirement of the sample. The plots contain two distinct densely populated areas: one at high energy that is composed of beam energy photons, and the other covering most of the parameter space below 2 GeV.
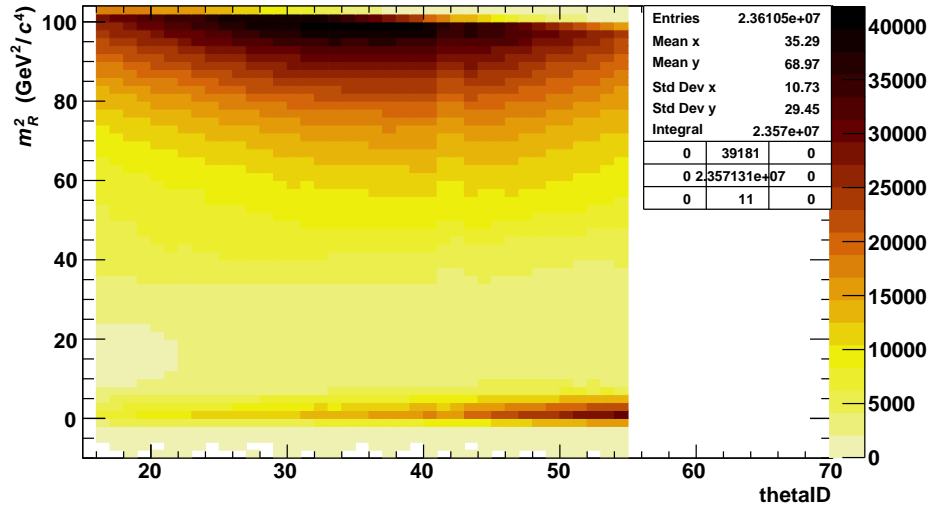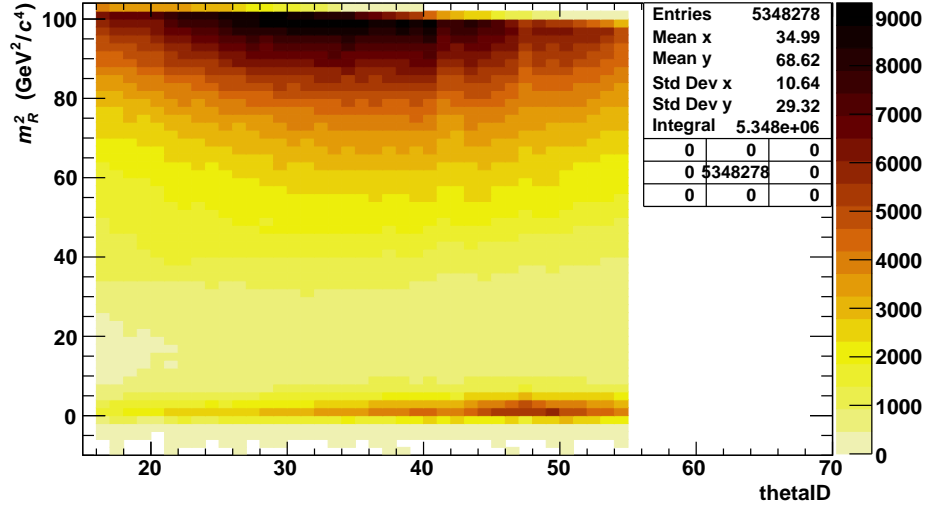
Figure 5.12: The data (top), and MC (bottom), distributions of the square of
the mass recoiling against the photon as a function of the thetaID for
the recoil photon. Due to relation of the square of the mass recoiling
against the photon to the CMS energy of the photon, this plot appears
very similar to E^* vs thetaID, though reflected around the x-axis and
translated. However, there are slight other differences because the data
was taken at several different beam energies, as laid out in Table 5.1.
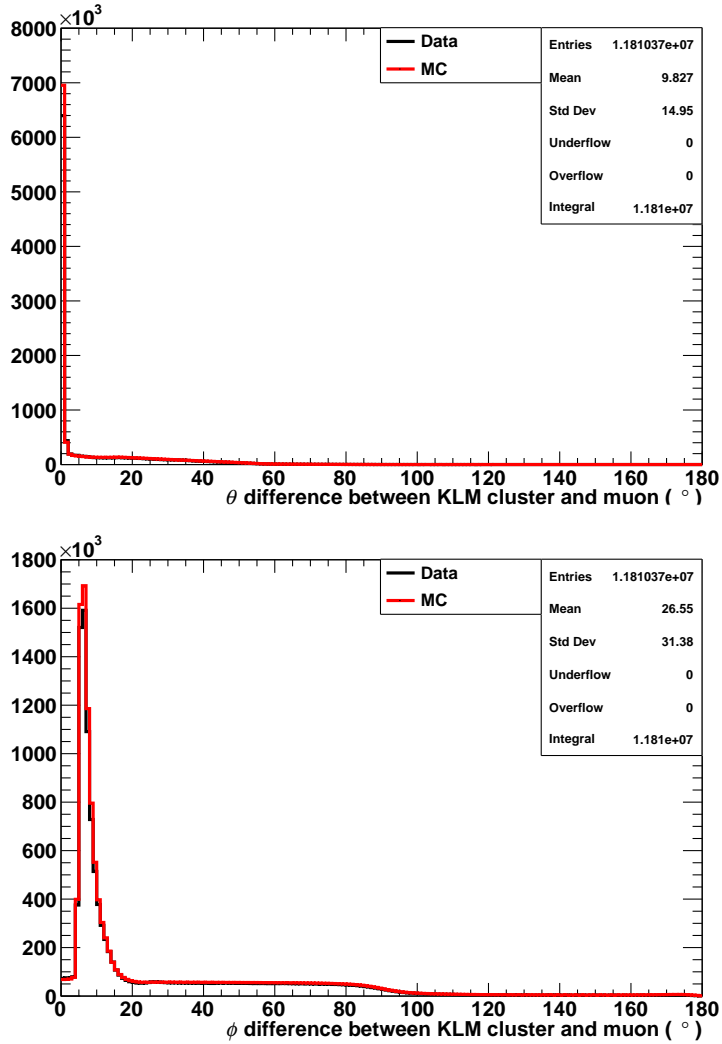
Figure 5.13: The θ (top), and ϕ (bottom), angular difference between a KLM cluster and the closest muon. Closer here means the muon nearest in θ for the θ difference plot, or nearest in ϕ for the ϕ difference plot. MC normalized to data by luminosity and the information tabs are for data. These are made using the radiative dimuon control sample, but without criteria for the selection of the KLM clusters. The θ difference is very narrowly peaked at $0°$, while the ϕ difference peak is broader and peaked near $10°$. This is caused by the curvature of muons in ϕ. Both plots show excellent agreement between data and MC.

to account for the large spread in ϕ, we would have to exclude cases where the θ value is well away from the muon, thereby excluding more clusters unnecessarily.

The θ and ϕ angle difference plots indicate that very generous bounds for the exclusion of KLM clusters would be $10°$ in θ, and $30°$ in ϕ. This would mean excluding all clusters within $10°$ in θ, and within $30°$ in ϕ, which would be expected to be sufficient. However, when the number of layers in a KLM cluster is plotted as a function of the ϕ or θ difference between the KLM cluster and the nearest muon for clusters that are relatively in time, it becomes evident that the above cuts would let muon associated clusters through. In time is defined as $|t_K| < 20$ ns, a region which contains roughly 70% of entries in the previous histograms. These plots can be seen in Fig. 5.14 and Fig. 5.15 for the θ and ϕ differences respectively.

These figures suggest that more appropriate values for the exclusion bounds are $20°$ in θ, and 30–$40°$ in ϕ. In order to be more cautious, $40°$ in ϕ was chosen lest muon related KLM clusters be included in the radiative dimuon control sample. Incidentally, both sets of figures demonstrate the similarity of data and MC for these quantities.

It's essential to note that because of the way in which KLM clusters are handled, only the four KLM clusters with the highest n_K are considered. The muon proximity requirements are then imposed, and the remaining KLM clusters are the ones used hereafter.

Extra photon selection

While neutral ECL clusters are not necessarily photons, in this thesis all neutral clusters will generally be referred to as photons.

The recoil photon is not the only photon of interest in the control sample events. We are also interested in the lower energy photons, as they will be useful later in determining appropriate ECL vetoes. Of these other, lower energy photons, only the three highest lab energy ones that satisfy $|t_c| < 200$ ns will be considered, and if they pass the other criteria described below, stored and referred to as the extra photons. The t_c requirement is present so that photons that are not related to the rest of the event are not included, and was inspired by a similar cut made in [28]. If out-of-time photons were included in the extra photons it could result in the event
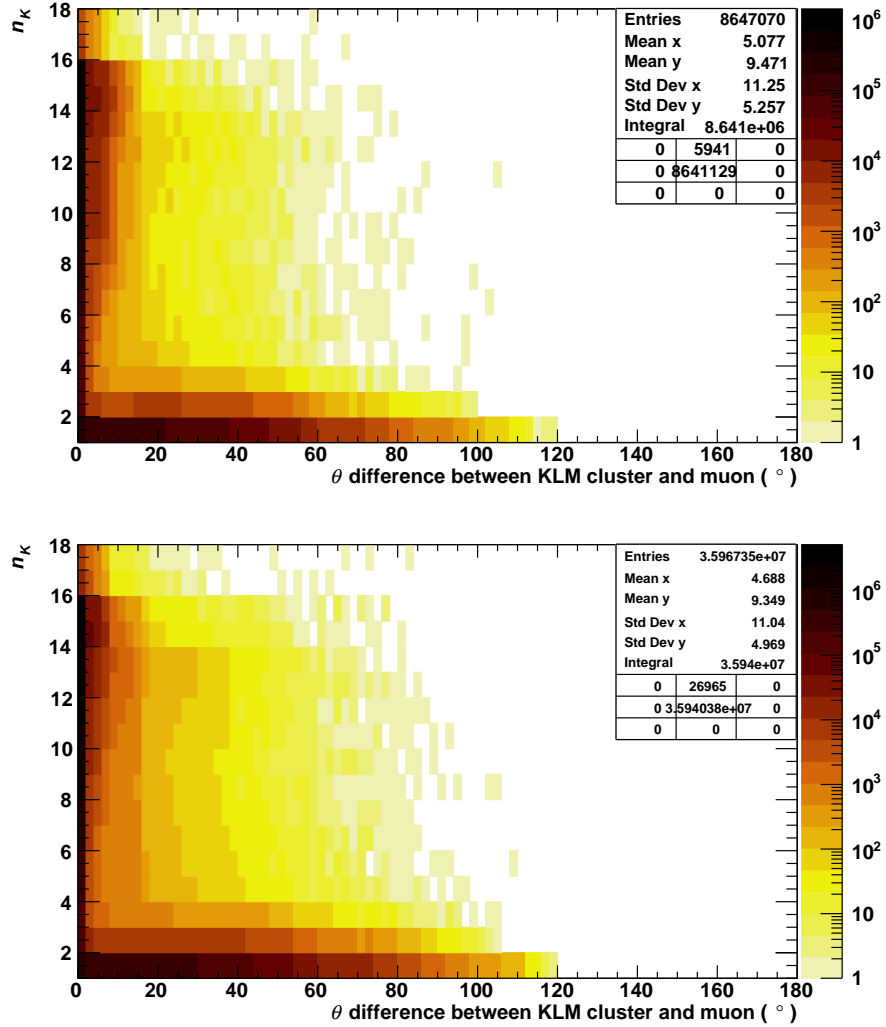
Figure 5.14: n_K plotted as a function of the θ difference between the KLM cluster and the closer (in θ) muon. Data is shown at the top, and MC on the bottom. These are made using the radiative dimuon control sample, but without criteria for the selection of the KLM clusters. They reveal the correlation of the number of layers in a KLM cluster and the θ proximity of that KLM cluster to a muon. There is a particular concentration of high n_K clusters below a θ difference of $20°$ in both data and MC. This correlation is due to the KLM clusters caused by the muons themselves.

53
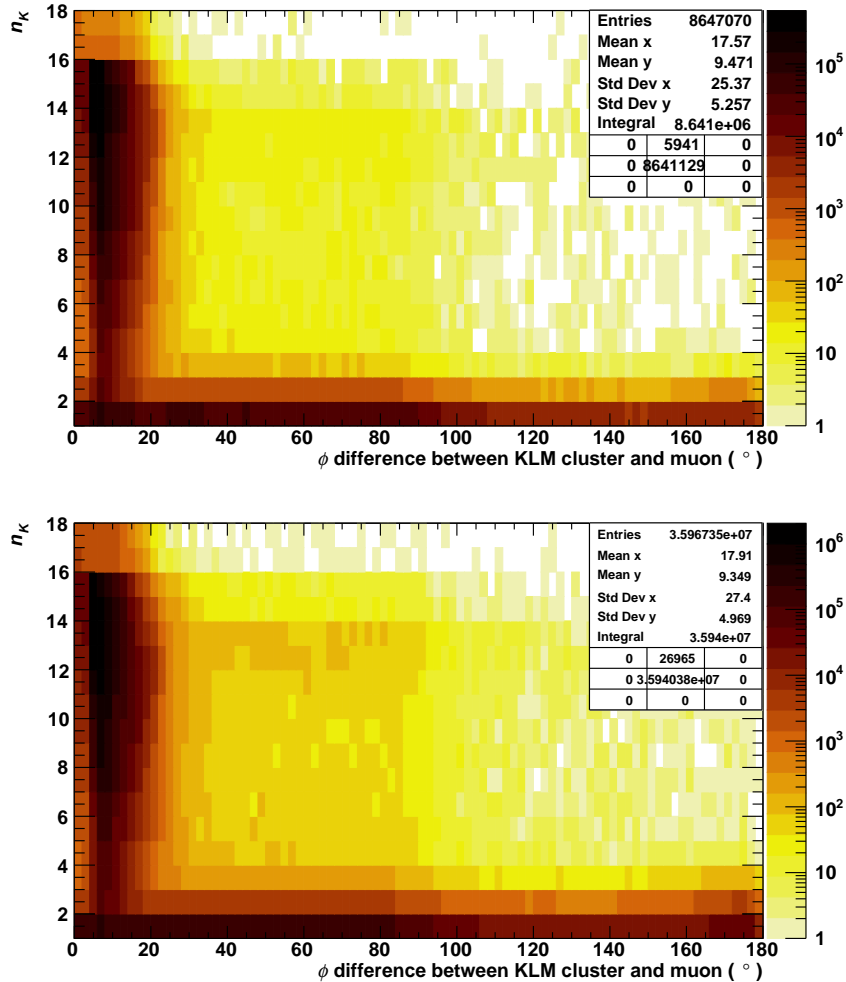
Figure 5.15: n_K plotted as a function of the ϕ difference between the KLM cluster and the closer (in ϕ) muon. Data is shown on the top, and MC on the bottom. These are made using the radiative dimuon control sample, but without criteria for the selection of the KLM clusters. They reveal the correlation of the number of layers in a KLM cluster and the ϕ proximity of that KLM cluster to a muon. There is a particular concentration of high n_K clusters below a ϕ difference of $35°$ in both data and MC, though there is another structure in MC that extends to larger ϕ differences as well. This correlation is due to the KLM clusters caused by the muons themselves.

54

being vetoed unnecessarily. The rest of the extra photon criteria relate to their proximity to the muons both in space and time.

Just as muons can cause KLM clusters, they can also cause neutral ECL clusters by producing final state radiation (FSR) photons. They can also create photons through interactions with detector material, though FSR is the dominant cause. Again, similarly to the KLM clusters caused by the muons, these particular photons would not be present in a single-photon event, and thus when using this sample to design photon vetoes these photons need to be ignored. Plotting the θ and ϕ between the extra photons and the closest muon, shown in Fig. 5.16 reveals that there is a concentration of photons near the muons. In θ the curve levels out at $10°$ separation, and in ϕ there is a sharp initial spike, followed by a small second bump ending at $15°$ separation. The differing behaviour between θ and ϕ may be partially explained again by the curving trajectory of muons in ϕ. There is also a noticeable difference between MC and data, though the histogram shape is quite similar. MC15rd has significantly more extra photons present than data.

The criteria for spatial proximity to the muons are established based on the curves' behavior, as detailed above. Consequently, the threshold is defined as being within $10°$ in θ and $15°$ in ϕ. With the spacial proximity requirements set, the temporal proximity can be considered.

When the extra photons are sorted by whether they are close to the muon or not according to the θ and ϕ criteria above, their respective time distributions can be studied. Figure 5.17 shows these two time distributions, and it can be seen that the majority of proximal photons have a small absolute time, while those away from the muon do not. Most photons near muons have a time less than 40 ns, while most further away from muons have a time greater than 40 ns. This occurs because the majority of photons close to the muons are associated with the muons, whereas the photons further away are usually not related, caused by beam background or similar. As we do not want to study photons that are caused by the muons, we can use a combination of the angular and temporal proximity to exclude such photons. Therefore, the selection for the extra photons is that the three highest momentum photons with $|t_c| < 200$ ns are stored if they do not also satisfy all three of $\Delta\theta < 10°$, $\Delta\phi < 15°$, and $|t_c| < 40$ ns. The time requirement ensures that relatively out-of-time photons are not excluded from the control sample simply because they are spatially
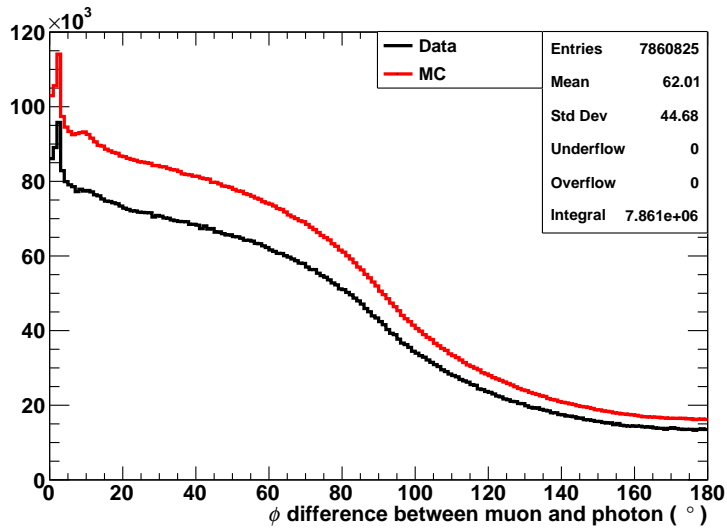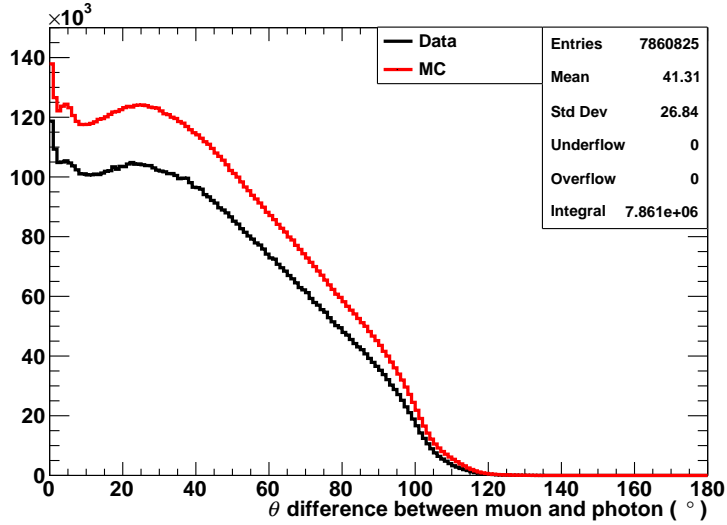
Figure 5.16: The θ (top), and ϕ (bottom), angular separation between the extra photons and the closest muon of the pair for both data and MC. Closest in this case is determined by 3D angular difference. MC is scaled to data by luminosity and the information tabs are for data. These are made using the radiative dimuon control sample, but without criteria for the selection of the ECL clusters. MC and data agree in shape, though not in number, with MC always higher. Peaks are present at or near zero for both, as expected.
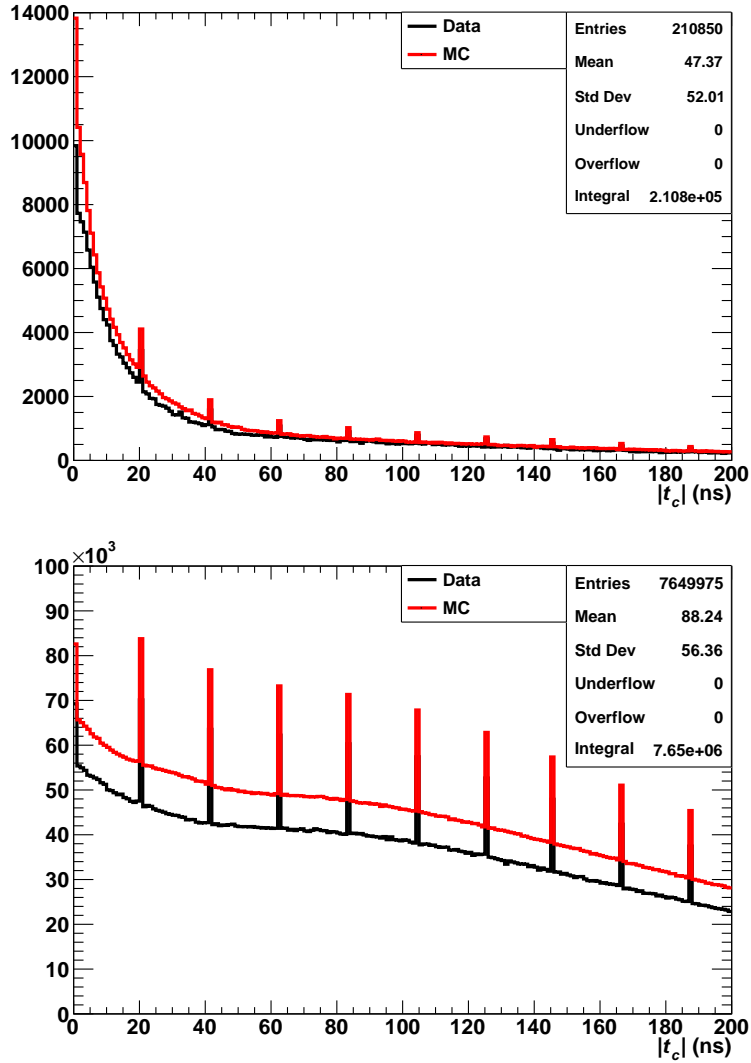
Figure 5.17: The absolute value of t_c for extra photons that fall into the angle cut defined above (top), and extra photons that are not in the angle cut (bottom), for both data and MC. MC is scaled to data by luminosity and the information tabs are for data. These are made using the radiative dimuon control sample, but without criteria for the selection of the ECL clusters. The spikes that can be seen in both plots are due to binning. There are few photons in the top plot that have poor timing, while there are many in the bottom plot.

57

close to the muons. The boundary value was chosen as 40 ns because it corresponds to the location that both plots in Fig. 5.17 approach a plateau.

Tracks and extra object selection summary

Tracks are selected as long as they are not the track of either of the two muons. They are ranked by various quantities, and stored according to what is required for studying vetoes. Table 5.3 summarizes the selection of the KLM clusters, extra photons, and tracks for the radiative dimuon control sample.

Table 5.3: A summary of the criteria for selecting KLM cluster, extra photons, and tracks for the radiative dimuon control sample. The initial criteria is applied. This means that even if there are more than 4 KLM clusters in the event, there might not be 4 KLM clusters that are considered part of the radiative dimuon control sample if the 4 with the highest number of layers do not pass the secondary requirement.

Category	Criteria	
	Initial	**Secondary**
KLM clusters	4 highest n_K clusters	Not within $20°$ in θ AND $40°$ in ϕ of a muon
Extra photons	3 most energetic (non-recoil) photons with $|t_c| < 200\,\text{ns}$	Not satisfying both: within $10°$ in θ AND within $15°$ in ϕ of a muon, $|t_c| < 40\,\text{ns}$
Tracks	Any track that is not one of the muon tracks	–

5.3 KLM vetoes

As has been mentioned, the KLM can be used to detect photons, and therefore can be a useful detector for vetoing events that contain extra photons or other particles that we do not want. As discussed in the control sample subsection on self contamination 5.2.5, we have removed KLM clusters that are near the muons since the muons are well detected by the KLM, but are not of interest since the purpose of this control sample is to replicate single-photon events, which would not include these muons.

5.3.1 Number of KLM layers

One of the most useful quantities that the KLM provides is the number of layers of the KLM that are involved in the cluster, which we denote as n_K. We use this quantity to categorize the KLM clusters, allowing us to tailor veto requirements for the different n_K. n_K is the natural parameter by which to categorize due to the distinctly different distributions it has in response to various particles, particularly muons, and photons. Additionally, for the lowest-layer KLM clusters there is a good chance that the KLM cluster is caused by non-interesting physics and noise, like neutrons, and therefore these KLM clusters need to be treated somewhat differently.

An important distribution to study when designing KLM based vetoes for the single-photon analysis is the number of KLM layers in clusters caused by the single-photons. In this sample, because of the recoil photon and recoil momentum ratio requirement, the single photon has been well reconstructed, and therefore likely has little leakage through the ECL. The leakage matters since high leakage means more energy in the KLM, and less in the ECL. For these high-energy ($\gtrsim 0.5\,\mathrm{GeV}$), low-leakage photons, the distribution of the number of layers of nearby KLM clusters is shown in Fig. 5.18. The KLM clusters that are caused by these photons rarely exceed 2 layers, with around 99.6% of them being 1 or 2 layer clusters. This indicates that any KLM cluster with 3 or more layers is highly unlikely to be caused by a well reconstructed single photon, and we are free to veto on these clusters without worrying about vetoing on the signal itself.

While noise can cause KLM clusters with a small number of layers, they are rarely larger than even 1 layer, meaning that if there is a KLM cluster of more
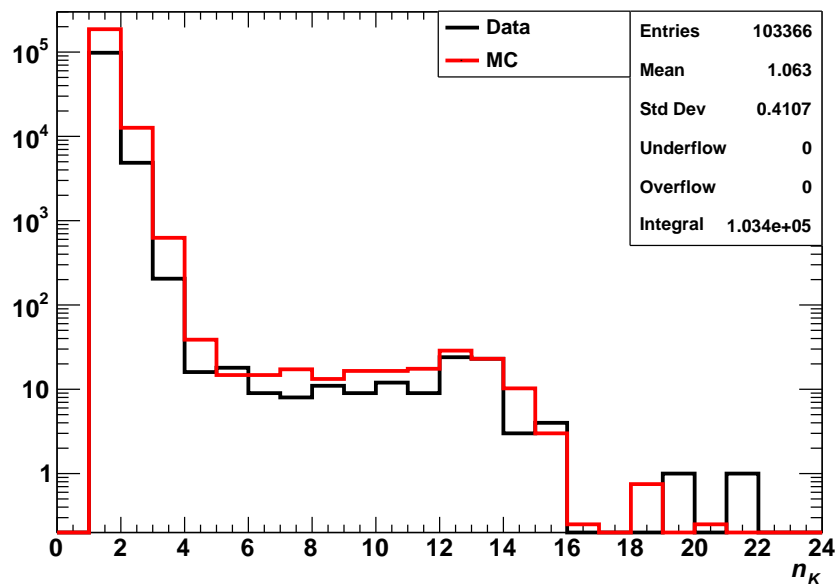
Figure 5.18: n_K for KLM clusters within $8°$ of the recoil photon for events in the radiative dimuon control sample. MC is normalized to data by luminosity and the information tab is for data. The angular difference restriction is imposed so that this plot contains primarily KLM clusters that are likely caused by the recoil photon. $8°$ was chosen as the angular bound based on being roughly half the angular spread of photons related KLM clusters, shown later in Fig. 5.22. This figure is intended to demonstrate that the vast majority of KLM clusters close to the recoil photon have fewer than 3 layers. MC has considerably more entries than data even when normalized, a fact that is obscured by the logarithmic scale. The likely cause of this is multi-strip hits.

than 2 layers in the event, there is likely something else in the event. As such, we veto events that have a KLM cluster of 3 or more layers regardless of the other KLM quantities. This does not veto a significant percent of the control sample, and therefore nor should it for signal. The distribution of n_K for the control sample can be seen in Fig. 5.19, where it is important to note that an event can have more than one KLM cluster, and thus more than one entry in this plot. While there are only

15 KLM layers in the barrel, it is possible for barrel and endcap layers to both be involved in one cluster, thereby allowing n_K to exceed 15 on occasion. The vast majority of KLM clusters are 1 or 2 layers, with less than 1% having more than 2 layers.
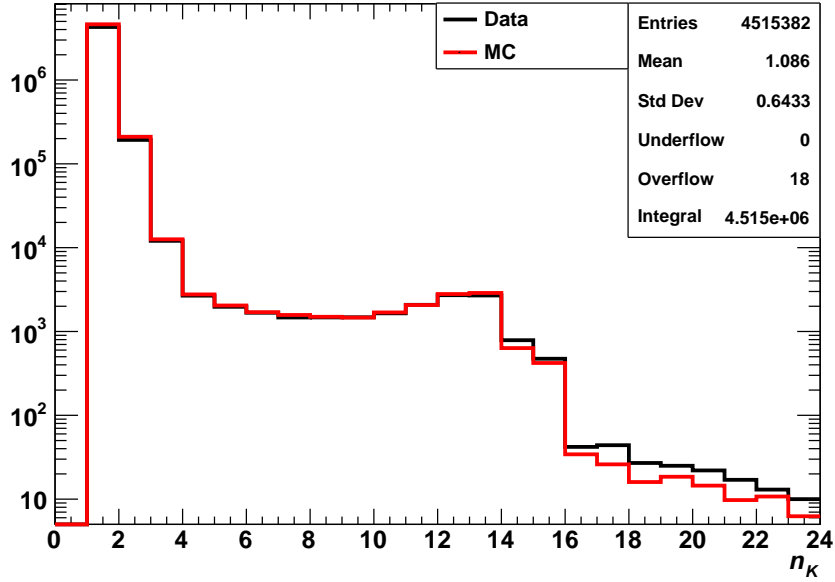
Figure 5.19: n_K for the radiative dimuon control sample. MC is normalized to data by luminosity and the information tab is for data. As events can have a number of KLM clusters, there are many events with no entries in this plot and many with multiple. The vast majority of KLM clusters have 1 or 2 layers. The data-MC agreement is considerably better than when looking only within 8° of the recoil photon.

For the 1- and 2-layer clusters other KLM quantities are taken into consideration since these clusters don't necessarily indicate that the event isn't a single-photon event. Aside from that, there are far more of these clusters, and overly broad vetoes would veto much more of the signal proxy than the 3+ layer veto. The quantities that we use to characterize the KLM clusters aside from the number of layers are: the innermost layer of the cluster, I_K, the timing of the cluster, t_K, and the angular

proximity of the cluster to the single photon, α_K.

Table 5.4 shows a summary of the KLM vetoes using the parameters just described. A more detailed description of these vetoes and their motivation can be found below.

Table 5.4: Summary of the KLM vetoes for the single-photon analysis, developed using the radiative dimuon control sample. If any KLM cluster satisfies one of the sets of requirements, the event would be vetoed.

n_K	Veto requirements
≥ 3	none
2	$-10\,\text{ns} < t_K < 30\,\text{ns}$ $I_K \leq 4$ $\alpha_K > 15°$
1	$-10\,\text{ns} < t_K < 30\,\text{ns}$ $I_K \leq 4$ $\alpha_K > 165°$

5.3.2   KLM timing

KLM clusters that are directly related to the event should all have a t_K near 0 ns, and those clusters that don't are likely caused by beam background, cosmic rays, or noise. Therefore, we only want to veto 1- and 2-layer KLM clusters if they are sufficiently in time, and would prefer to err on the side of classifying more clusters as in time to ensure that all event-related clusters are considered in time.

The plots in Fig. 5.20 show the t_K distribution for MC and data for both 1 and 2 layers. The MC and data curves are noticeably different, both in shape and centre location. The data histogram is noticeably asymmetric, with a sharp rise at t = 0 ns. This behaviour is what is expected since the timing is calibrated. For MC however, the peak is largely symmetric, perhaps indicating that it is not calibrated, or is calibrated using a different method. This MC-data difference is not so substantial as to give rise to issues, though its cause is not fully understood. Where MC and data do agree however, is on the long tails present for both the 1- and 2-layer KLM clusters. There are tails on both sides, though, for the 1-layer clusters, the left-side tail is much more prominent.
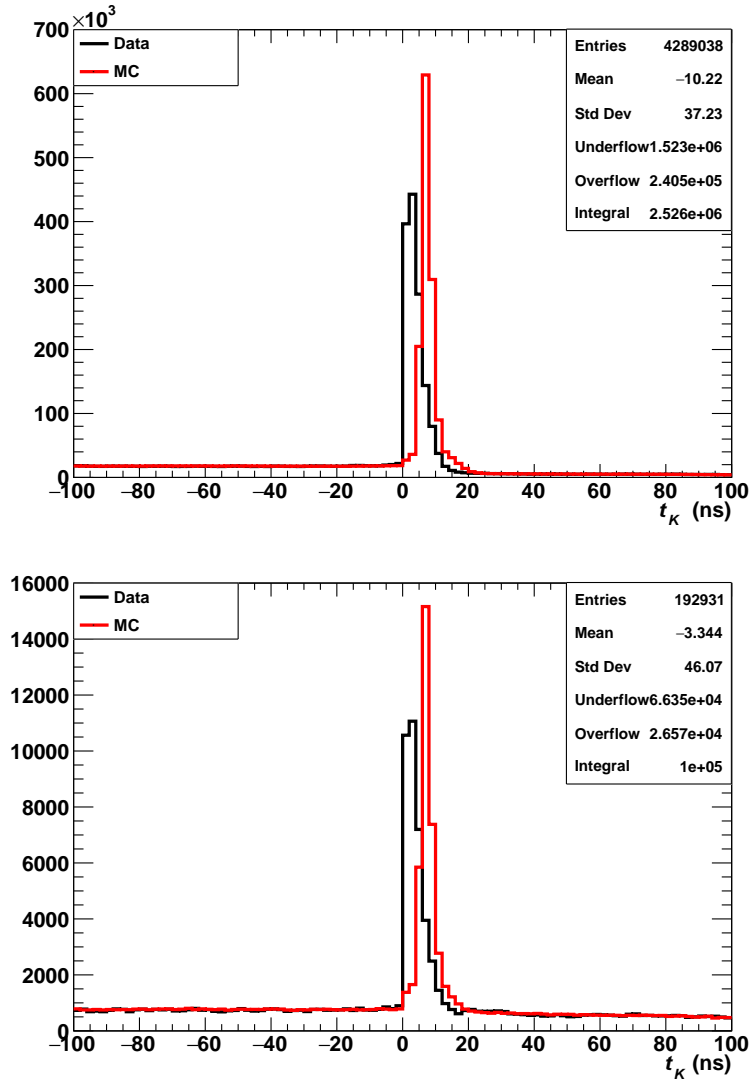
Figure 5.20: t_K distributions for 1- and 2-layer clusters (top and bottom, respectively) in the radiative dimuon control sample for data and MC. MC is normalized to data by luminosity and the information tabs are for data. The two plots are similar in shape, though not in scale. Data and MC noticeably do not agree, with MC being more sharply and symmetrically peaked, with a higher central value, and more entries. However, the two central values are close together, and the peaks nearly entirely overlap, settling to background levels at the same place.

A range of $-10\,\text{ns}$ to $30\,\text{ns}$ encompasses the entire peaking region near $0\,\text{ns}$ for data and MC in both plots, plus a small region around the peak. Outside this range, the distribution is flat, an indication that those KLM clusters are not collision-related. As such, in time is defined as $-10\,\text{ns} < t_K < 30\,\text{ns}$, and only clusters within this time window will be vetoed on.

5.3.3 Innermost KLM layer

I_K is useful particularly in discriminating between photons and other particles, and whether or not that photon is coming from the IP. Particles in general, but especially photons that are coming from the IP, will register in the inner layers of the KLM, not just in the outer layers. This means if I_K is sufficiently high, it is very unlikely to be caused by a particle coming from inside the detector at all, and particularly not by a photon. This also makes I_K useful for ignoring noise and external interference in the detector, since it allows us to ignore the KLM cluster if I_K is greater than a certain value.

From the plots of I_K in Fig. 5.21, it can be seen that most clusters have a high I_K, and that at low I_K where we are most interested the entries per bin varies significantly. The histograms are relatively flat for I_K values of 5–10, and at a level that is consistent with our expectation of most particles not starting a KLM cluster in the middle of the layers of the KLM. For the reasons discussed in the last paragraph, we will only veto on clusters with a I_K of 4 or lower, as these are likely collision related clusters. 4 was chosen as the boundary for this veto based on where the plots in Fig. 5.21 change behaviours and level out.

The high proportion of events that have a I_K greater than 10 is caused by energetic neutrons that hit the detector from the outside. These neutrons are created by the accelerator and beams in large numbers, and impact the KLM significantly since it is the outer detector. Shielding to limit this effect is being installed in the current Belle II shutdown (2023). Neutrons produced by the beams interacting with accelerator and detector material can also cause some KLM clusters in the innermost few layers of the KLM, though this is a less prominent effect.

Low I_K is also where there is the greatest MC-data discrepancy for both 1- and 2-layer clusters. The cause of these discrepancies is likely the differing ways that
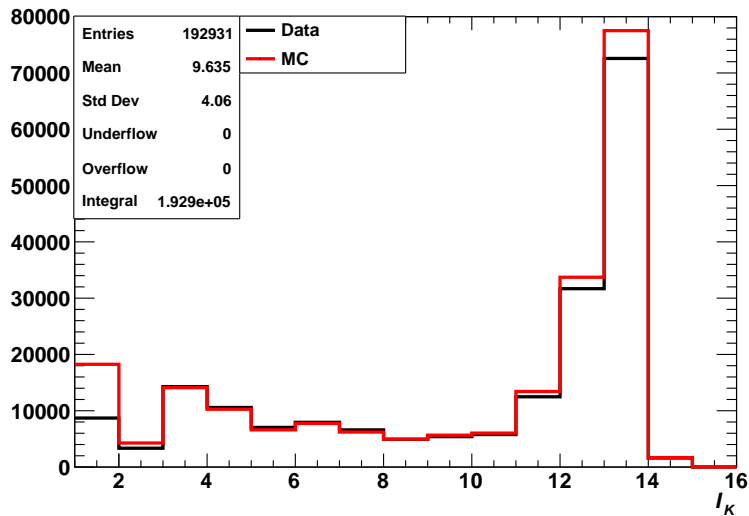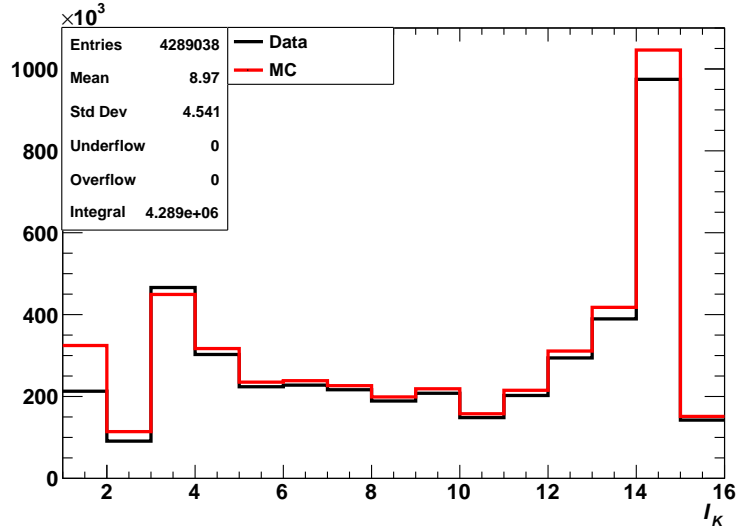
Figure 5.21: I_K for 1- and 2-layer clusters (top and bottom, respectively) in the radiative dimuon control sample. MC is normalized to data by luminosity and the information tabs are for data. Data-MC agreement is very good aside from the first few layers. In the innermost layers MC has significantly more entries, an effect ascribed to the differing treatment of multi-strip hits in data and MC. The large number of entries with an innermost layer of 12 or higher is predominantly caused by neutrons coming from outside of the detector.

MC and data handle multi-strip hits. Multi-strip hits are particularly prominent in this analysis because of the way photons shower in the KLM, but they are an issue for the Belle II collaboration as a whole, including in K_L^0 reconstruction [15]. For a more detailed description of multi-strip hits see [26].

One other potential factor for the MC-data discrepancies could be an overestimation of the photon detection efficiency in MC. This could occur because the calibration of detection efficiencies in the KLM is done using muon events. The detection efficiency of photons is not necessarily directly linked to that of muons, and could cause a discrepancy between MC and data as a result. This would have to be a small effect, or one that is only present for the scintillators since the MC-data agreement is reasonable at higher I_K.

Another curiosity present in the plots of I_K is that there is a notable lack of clusters with an innermost layer of 2 relative to an innermost layer of 1 or 3. This is present among both 1- and 2-layer clusters, and data and MC, though it is more prominent in 1-layer clusters and in data. Part of the reason for this is may be that the innermost two layers of the barrel, which are scintillator, are less sensitive than the outer barrel layers. This loss of sensitivity at least in data may be caused in part by the multi-strip hit issue. This means clusters with innermost layer 1 or 2, are less likely, particularly if we are looking for only 1 layer clusters. However, since particles lose energy rapidly in the KLM, especially in the steel plates at the beginning, we do see a relatively large number that start in layer 1, particularly considering their poor efficiency for photons. In addition, the innermost layers receive much more background radiation due to being closer to the IP, which also contributes to particularly the higher number of $I_K = 1$ clusters. However, a complete description and understanding of the cause of these I_K distributions has thus far eluded us.

5.3.4 Angular separation from the single photon

The angle from the single photon requirements are harder to motivate with this sample, but the purpose of them is to not veto on a KLM cluster that is either caused by the single photon (2 layer) or that is just noise (1 layer). We must also be careful that we do veto backgrounds though, such as $e^+e^- \to \gamma\gamma(\gamma)$ with its back-to-back photon. In Fig. 5.22 it can be seen that $15°$ (3D) away from the single

photon is the extent of the KLM response to a single photon. As such, to veto on a 2 layer KLM cluster, α_K must be greater than $15°$. We can be reasonably confident that the peak present in both plots below $15°$ angular separation is indeed the KLM response to the photon itself, because only in this region of the plots does the shape deviate significantly from that expected if the KLM cluster and photon angles were uncorrelated.

For 1 layer clusters, even with all the other criteria, they are likely to be caused by beam background or noise, and therefore these clusters should not be vetoed on unnecessarily. Events that produce back-to-back photons are a large background for the single-photon analysis, thus we want to be as sensitive to such events as possible. The back-to-back photons in these events might cause a KLM cluster, even if the ECL failed to detect them. As a result, we only veto the event if the 1 layer KLM cluster is within $15°$ of back-to-back, equivalent to greater than $165°$ from the single photon. This value was chosen based on the upper plot of Fig. 5.22. This plot does not show any interesting behaviour near $165°$ that would indicate it is a good value for such a cut, which is as expected, since in a radiative dimuon sample there should be no preference for a KLM cluster back-to-back with the photon. However, as is mentioned above, this plot does show that 1-layer KLM clusters which are the result of photons are predominantly within $15°$ of that photon. This implies that 1-layer KLM clusters caused by back-to-back-photons should be more than $165°$ from the recoil photon, hence this bound.

Figure 5.22 demonstrates another large MC-data discrepancy, one that is strongly related to the discrepancy shown in the I_K plots. This MC-data difference is present only at small angular separation of the KLM cluster and radiated photon, and therefore is related to differing detection and reconstruction efficiencies of photons in the KLM in MC and data. This means that this large disagreement between MC and data is caused by the same issue that caused the disagreement in the I_K plots: multi-strip hits. This hypothesis is supported by a study conducted by another analysis team member. In that study, the way that the hits are used in reconstruction in MC and data was reconciled as much as possible. The result of this was that there were a significant number of KLM clusters near photons that were reconstructed when multi-strip hits were used, that were not reconstructed with the regular code.

Luckily, the way multi-strip hits are handled currently is a recognized issue,
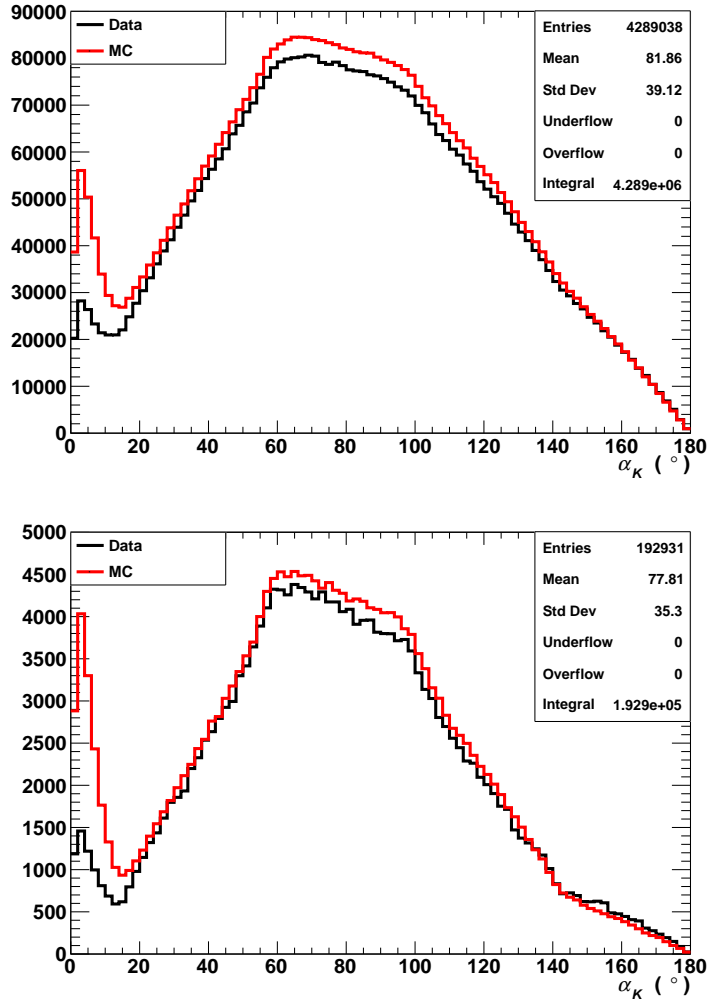
Figure 5.22: The 3D angle between the recoil photon and 1- and 2-layer KLM clusters (top and bottom, respectively) in the radiative dimuon control sample. MC is normalized to data by luminosity and the information tabs are for data. Data and MC are in good agreement except for at smaller (α_K). Below 20° angular separation there is a spike in entries, as would be expected if some of the photons are detected by the KLM. However, MC indicates that significantly more photons are detected by the KLM than data suggests. This gap in detection is again most likely caused by the poor treatment of multi-strip hits in data.

and the reconstruction code has been modified for the next basf2 release, both by making better use of multi-strip hits in data reconstruction, and by making MC reconstruction more realistic.

5.4 ECL cluster vetoes

5.4.1 Neutral ECL clusters

This subsection describes the selection of the vetoes that use neutral ECL clusters. Even though these clusters may not in fact be photons, they will frequently be referred to as photons as previously mentioned.

The presence of extra photons in the event — the definition of which can be found in subsection 5.2.5 — can be indicative of the event not being that of a single photon. However, lower-energy photons can be produced as a result of beam background, and do not necessarily mean we should veto the event. These two factors must again be balanced in deciding on the photon vetoes.

For photons, we use their energy in the lab frame to sort them into three categories: low energy (20–100 MeV), mid energy (100–300 MeV) and high energy (> 300 MeV). These ranges are chosen broadly along the lines of both frequency of occurrence, and an understanding of the detector. 20 MeV is the lower bound for the low energy range because it is the lowest energy for a photon that Belle II will reconstruct. A log scale plot of the full energy range is shown in Fig. 5.23, and linear scale plots of the energy broken down by category are shown in Fig. 5.24.
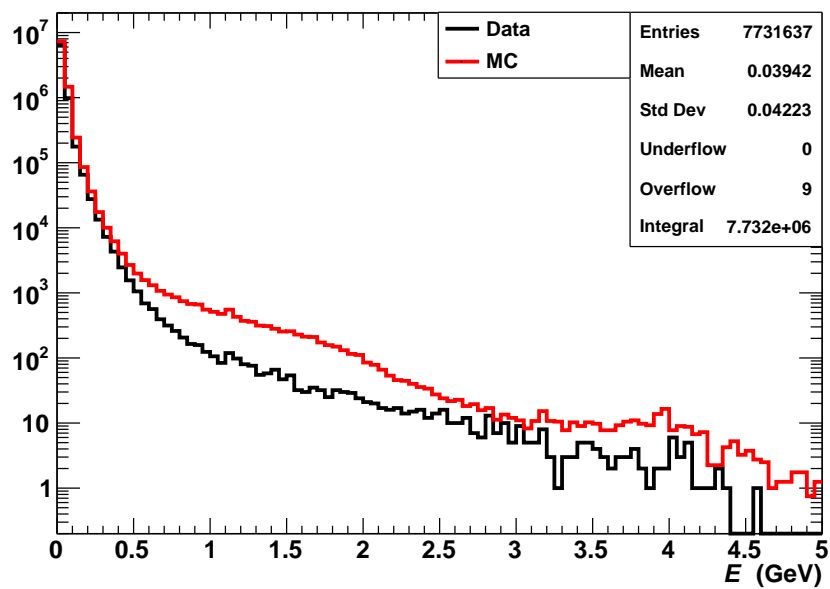
Figure 5.23: The energy of the extra photons for the radiative dimuon control sample. MC is normalized to data by luminosity and the information tab is for data. Events may have multiple entries. Data and MC have a similar distribution shape, but there are more entries in MC.
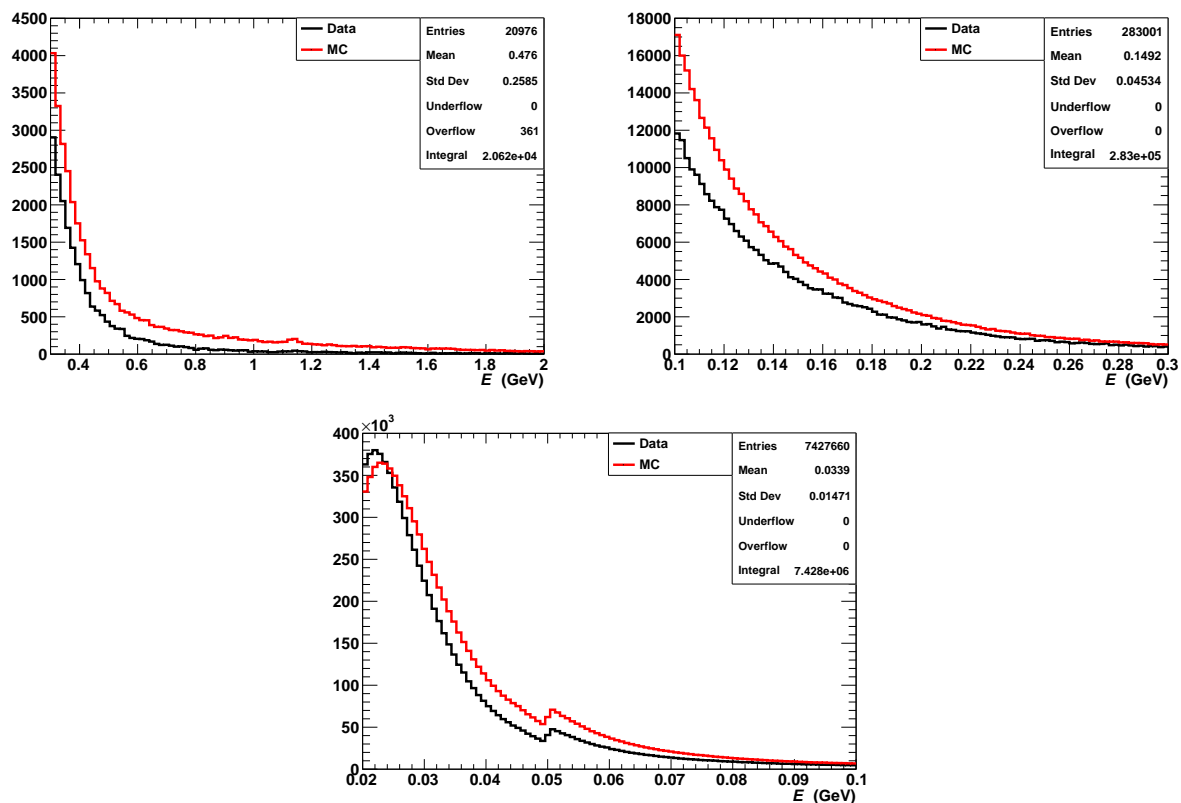
Figure 5.24: The energy of the extra photons in the high (top left), mid (top right), and low (bottom) energy ranges for both data and MC for the radiative dimuon control sample. MC is normalized to data by luminosity and the information tabs are for data. The high and mid energy plots are similar, with both looking like an exponential decay. The low energy plot however has two notable departures from this: first, near 22 MeV the distribution reaches a peak and decreases towards 20 MeV, the threshold for photons at Belle II. Second, there is a kink just above 50 MeV, which is caused by the requirement of $|t_c|/\mathrm{dt}99 < 1$ imposed on photons with $E < 50$ MeV.

The variables we use to characterize photons aside from lab energy are a quantity that represents the timing of the cluster, $|t_c|/\mathrm{dt99}$, and α_E, the angle between the single photon and the extra photon. t_c is not used directly because 100–300 MeV is a wide energy range, and without dt99 the timing is energy dependent. Table 5.5 displays a summary of the photon vetoes. The vetoes are described in more detail

Table 5.5: Summary of the photon vetoes for the single-photon analysis, developed using the radiative dimuon control sample.

Photon Energy	Veto requirements
> 300 MeV	none
100–300 MeV	$|t_c|/\mathrm{dt99} < 3$ $\alpha_E > 15°$
20–100 MeV	$|t_c|/\mathrm{dt99} < 1$ $\alpha_E > 176°$

below. The values are chosen based on Fig. 5.25, and Fig. 5.26. Figure 5.25 shows the distributions of $|t_c|/\mathrm{dt99}$ as a function of the photon energy, both for data and MC. Figure 5.26 shows the distributions of the angle from the single photon as a function of the photon energy, both for data and MC.

For the high energy range, any event with an extra photon that falls into this range ($E > 300$ MeV) will be vetoed, regardless of the photon's timing or angular proximity to the single photon.

In the mid energy range, in order to veto the event, $|t_c|/\mathrm{dt99}$ must be less than 3 to ensure it likely is a result of the event itself, and it must be more than 15° away from the single photon, so that we are sure it is not caused by interactions of the single photon with the detector.

In the low energy range, it's important to note that due to the large number of photons detected with < 50 MeV, there is already a $|t_c|/\mathrm{dt99}$ cut. Only photons with $|t_c|/\mathrm{dt99} < 1$ are kept, and so to ensure consistency in the low energy range, the timing veto requirement is $|t_c|/\mathrm{dt99} < 1$.

The angle from the single photon is again harder to motivate with this sample, however we want to veto as many events as possible that are potentially contaminated, while removing few 'clean' events. To study the optimal angular proximity requirement for the middle energy range, a plot was produced of the fraction of the
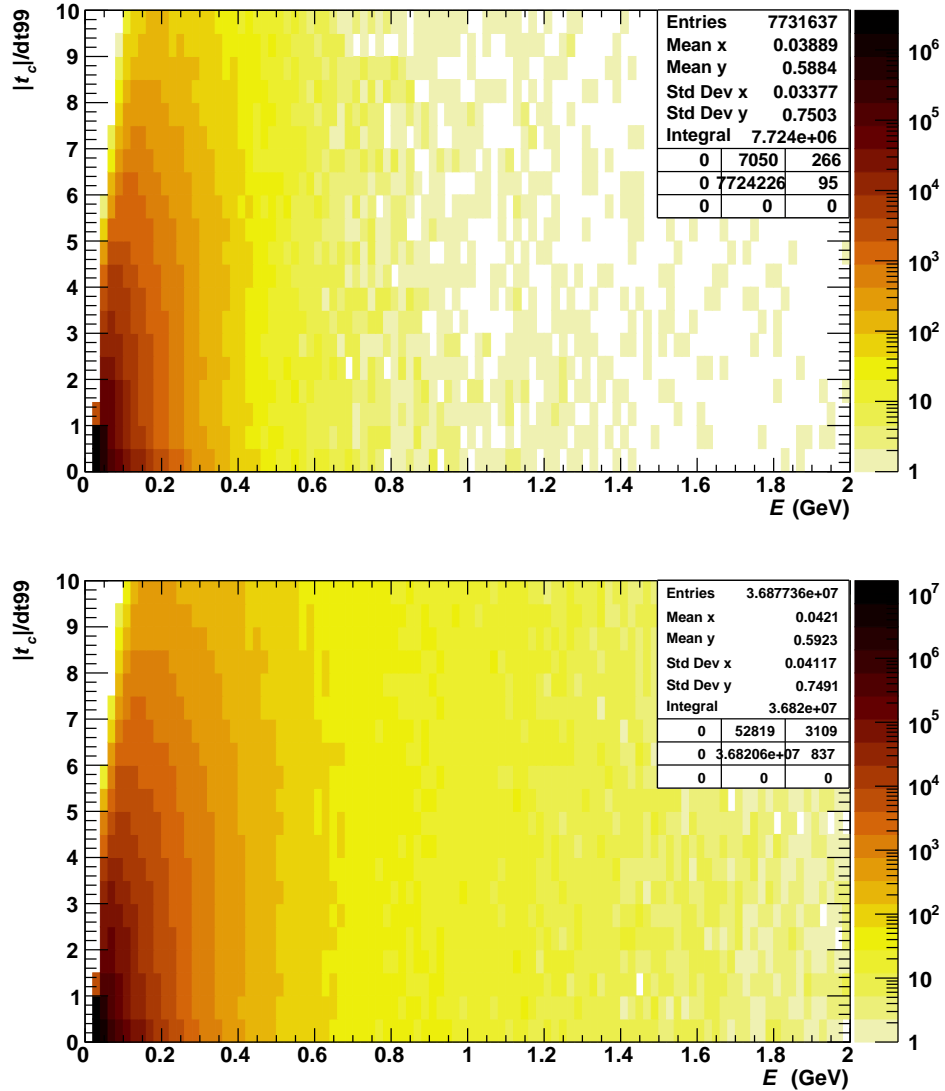
Figure 5.25: $|t_c|/\mathrm{dt}99$ as a function of the lab energy for the extra photons in the radiative dimuon control sample. Data can be seen in the top plot, and MC in the bottom plot. Below 50 MeV, photons must have $|t_c|/\mathrm{dt}99 < 1$, with the entries above this in the plots being caused by rounding.
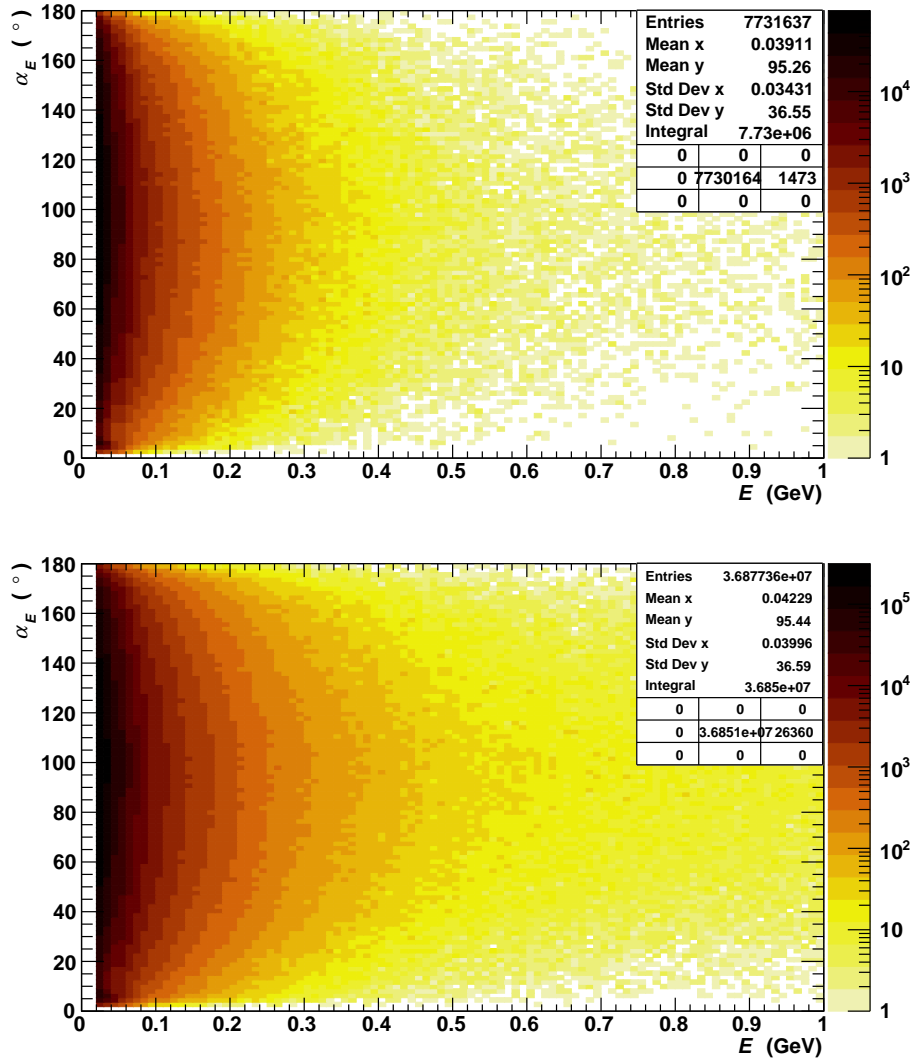
Figure 5.26: The 3D angle between the extra and recoil photons as a function of the extra photon energy. Data can be seen in the top plot, and MC in the bottom plot. The angular distribution corresponds to the expected shape for two uncorrelated vectors. Almost all extra photons in excess of 100 MeV have more than 15° angular separation from the recoil photon. As well, there are some extra photons with less than 100 MeV that have more than 176° angular separation from the recoil photon, though not many, which is as expected with this sample.

sample vetoed as a function of the angle from the single photon requirement. This plot, Fig. 5.27, indicates that at 15°, only 3.4% of the sample is vetoed in data, and 4.4% in MC. 15° is consistent with the angular proximity to single photons used elsewhere in this analysis, and vetoing around 4% of the signal was deemed acceptable. Without knowing how this cut affects all potential backgrounds, there is no optimization that can be done.

For the low energy range the angle requirement is, much like the corresponding KLM veto, about vetoing events with back-to-back photons. Therefore for the event to be vetoed there must be a photon with $\alpha_E > 176°$. This value is chosen based on the work of another collaborator who is studying a $e^+e^- \to \gamma\gamma(\gamma)$ sample.

5.4.2   Charged ECL clusters

The ECL vetoes in the previous subsection only dealt with neutral ECL clusters, clusters without an associated track. This of course leaves charged ECL clusters to deal with. One way to deal with this is to make a cut on E_t, the energy of an ECL cluster that is associated with a track. While E_t is corrected for leakage and background, it is otherwise simply the energy deposited in the crystal and therefore does not depend on a mass assumption. This assumption independence makes this a good variable for use in a veto.

A MIP will deposit around 190 MeV in the ECL, whereas energetic electrons will deposit more. Based on this, a 100 MeV E_t veto should remove events where track reconstruction for electrons failed but the ECL still recorded a large E_t, and also events that contain MIPs. 100 MeV should also be a high enough energy threshold that it is infrequent that a beam background related cluster overlaps with a track, and is mistaken as associated. This consideration matters since the neutral ECL vetoes have a different, and in the 100–300 MeV energy range, tighter veto than that of track associated ECL clusters.

Figure 5.28 shows the distribution of E_t for the track with the highest E_t for the radiative dimuon control sample. The majority of tracks with an associated E_t have a E_t in excess of 100 MeV, however, 99.5% of events in this control sample do not have a track with an associated E_t. This keeps the percent of the sample vetoed by this veto to below 0.5%. It is also why this veto does not amount to vetoing almost
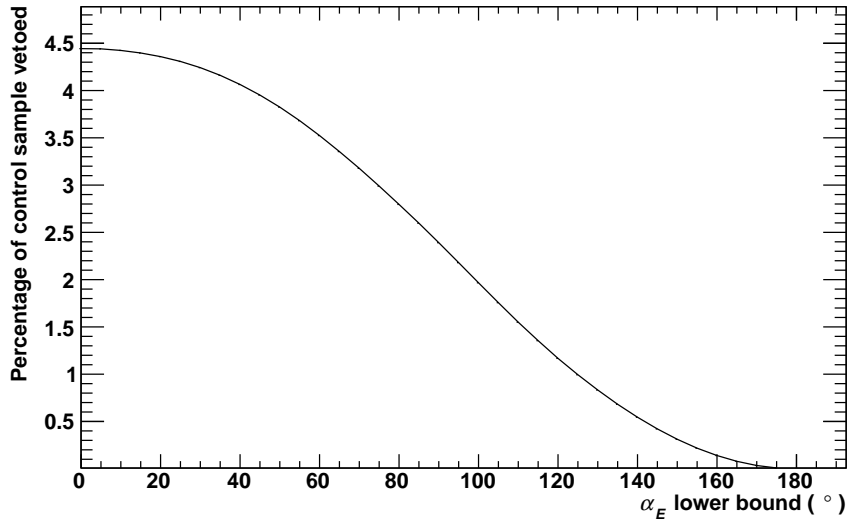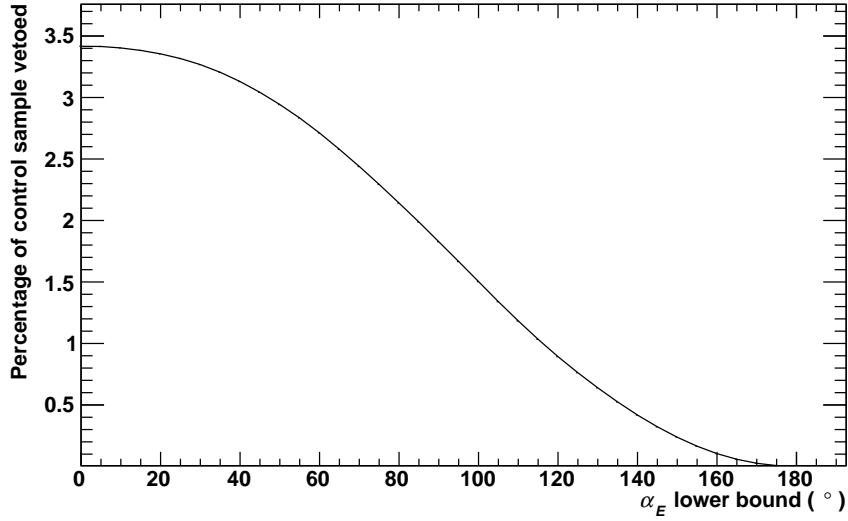
Figure 5.27: The percentage of the radiative dimuon control sample vetoed by the mid energy ECL veto as a function of the minimum angle from the single photon. Data is shown at top, and MC at bottom.

every event with a track. The impact of this veto on a background sample can be examined in the following sections to ensure that it serves its intended purpose.
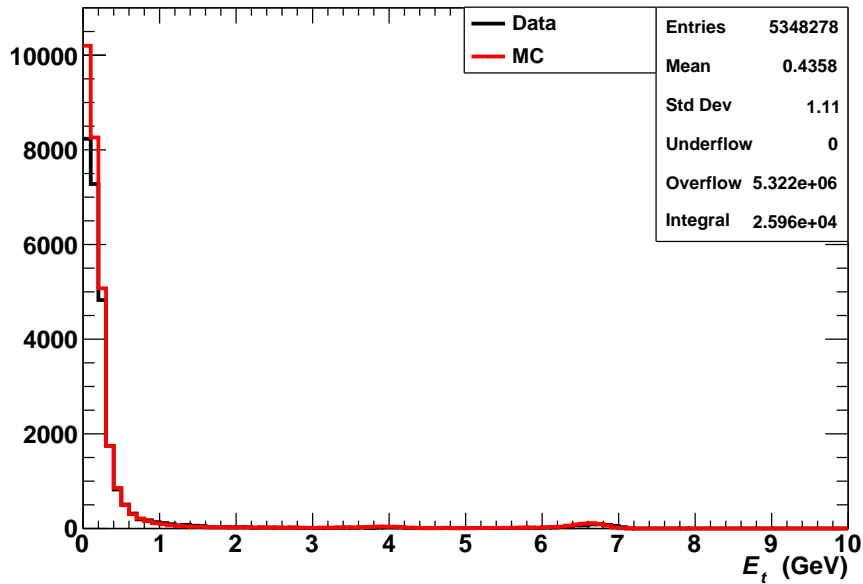
Figure 5.28: The distribution of the largest E_t in each event for the radiative dimuon control sample for both data and MC. MC is normalized to data by luminosity and the information tab is for data. While MC has more entries than data at very low E_t they generally agree. Note that are more events in overflow than in the plot by several orders of magnitude, as most events do not have any track associated ECL clusters.

5.5   Single photon requirements and vetoes from elsewhere

There are several requirements and vetoes for the single-photon analysis that are based primarily on work outside this thesis, and that have not yet been mentioned. The most interesting of these are discussed here as they will form part of the selection criteria for the next control sample. The veto is on n_{CDC}, while the requirements concern the single photon itself and use several variables.

Cosmics are a major background for the single-photon analysis. Cosmic rays often leave tracks, however, these tracks do not in general pass through or originate from the IP. As such, a veto for these events must not have any location require-

78

ment, but also must not simply veto on all tracks, lest too high a percentage of the signal gets vetoed trying to remove this one background. The n_{CDC} veto was chosen based partly on cosmic ray events.

The variable n_{CDC} is the number of CDC hits for a given track. The more hits there are, the more confident we are in that track. Tracks may have anywhere from 0 to over 100 n_{CDC}. Based on a cosmic study by a collaborator, cosmic tracks have a similar distribution of n_{CDC} to that of other tracks, and if tracks have 10 or more CDC hits it is extremely likely to be a well-reconstructed track of a charged particle. Therefore, if any track has $n_{\text{CDC}} > 9$, we veto the event. When implementing this veto in the radiative dimuon sample only tracks aside from those of the muons are considered, as specified in Subsection 5.2.5.

The photon requirements are designed to ensure that the photon in single-photon events is in a good location, of a sufficient energy, and displaying the qualities expected of a photon originating from near the IP.

In the selection of the radiative dimuon sample it was discussed why we restrict the photon to a subset of the barrel, and those reasons still hold for the single-photon analysis. The thetaID range for the single photon is [16, 54] for $E^* >$ 1 GeV. For $0.5 \,\text{GeV} < E^* < 1 \,\text{GeV}$, there is a θ instead of thetaID restriction due to the range that is part of the trigger that goes down to 0.5 GeV. This θ restriction is $(44°, 98°)$, which corresponds to roughly [21, 44] in thetaID.

The lower bound for the single photon center of mass energy is 0.5 GeV since this is around where the lower energy bound for the relevant single-photon triggers, and is also approaching the limit of our sensitivity for single-photon events.

Shower shape variables are used to ensure the neutral clusters are consistent with those of photons by quantifying the shape of the ECL cluster. Using plots of the various shower shape variables from the radiative dimuon control sample and from backgrounds, a collaborator determined that Z_{MVA} and C_{2M} have the best discriminating power. For the single photon, the requirements are $Z_{\text{MVA}} > 0.75$, and $0.5 \,\text{cm}^2 < C_{2M} < 1.5 \,\text{cm}^2$. See Chapter 2 for the definitions of Z_{MVA} and C_{2M}.

79

5.6 Radiative Bhabha control sample

The radiative dimuon control sample is useful for studying the effects of vetoes on signal, but not for understanding their effects on the background. Radiative Bhabhas are expected to be one of the major sources of background, and are therefore helpful for studying track cuts. Just as importantly, it is possible to obtain information relevant to the fitting for the single-photon analysis. This includes distributions of the single-photon E^*, and the square of the recoil mass against the radiative photon as a function of the single-photon thetaID. However, due to the MC samples available, these plots are not complete. This will be discussed more precisely later.

The key veto to be studied with this sample is one based on track information, specifically p or p_T, and |dz|. This sample will also allow some study of the E_t veto. Since radiative Bhabhas are a background, this sample should consist only of the events that would be left behind by the other single-photon selection criteria and vetoes so that we can tune our vetoes to remove as much of this sample as possible. When comparing to the radmumu sample this radiative Bhabha sample will allow us to see the effect of the track cut on both signal and background.

Once all the vetoes besides the E_t veto have been applied, we can examine the distribution of E_t for this background. Figure 5.29 shows the distributions of the highest E_t associated with a track in each event for this preliminary radiative Bhabha sample. The same plot, but for the radiative dimuon control sample can be seen in Fig 5.28.

The distributions themselves are different shapes, with the Bhabha distribution displaying significantly more prominent peaks near 4 and 7 GeV. However, the key feature is the percentage of events that even have a track with a E_t: the vast majority of radiative Bhabha events do, while the inverse is true for radiative dimuon events. As a result, the E_t veto significantly reduces the preliminary version of the radiative Bhabha sample, cutting almost 80%, while only removing just over 0.3% of the signal proxy, the radiative dimuon control sample. This is due primarily to the higher percentage of events with a track associated E_t as most E_t values are above 100 MeV in both samples.

One last veto that needs to be discussed in more detail is a veto on the number of

Entries	6232
Mean	4.421
Std Dev	1.861
Underflow	0
Overflow	1171
Integral	5061
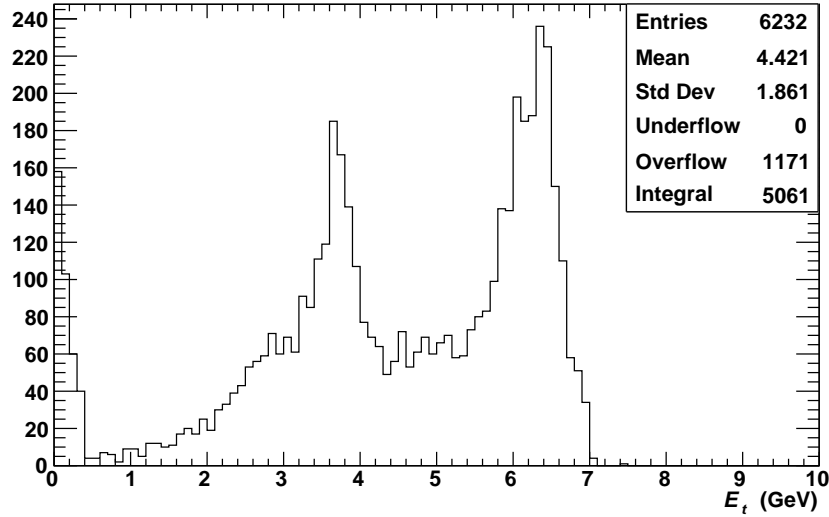
Figure 5.29: The distribution of the largest E_t in each event for the radiative Bhabha control sample, excluding a cut on E_t. There are peaks in the expected places for a Bhabha event, since E_t is a lab quantity, and in the lab the electron and positron initially have around 7 GeV and 4 GeV respectively. Also noticeable is the peak near 0 GeV with many tracks having less than 100 MeV.

ECL out-of-time crystals (n_{OOT}). This variable, defined in Chapter 2, is indicative of the magnitude of the beam background in an event. It was noticed by a collaborator that some events had n_{OOT} in excess of 2000, a significant fraction of the total crystals in the ECL ($\mathcal{O}(8000)$). These events have degraded clustering and tracking due to the immense beam background, and are not entirely reliable. In the radiative Bhabha sample, higher energy single-photon events were disproportionately likely to have a n_{OOT} in excess of 1000, relative to the overall sample. A distribution of the n_{OOT} for the otherwise complete radiative Bhabha control sample can be seen in Fig. 5.30.

Based on this plot, a veto of $n_{OOT} > 400$ was chosen, which is also consistent with where the collaborator started to notice issues, and with a study being conducted to calculate the final luminosity values for data.

Entries	1421
Mean	147.3
Std Dev	115.6
Underflow	0
Overflow	48
Integral	1373
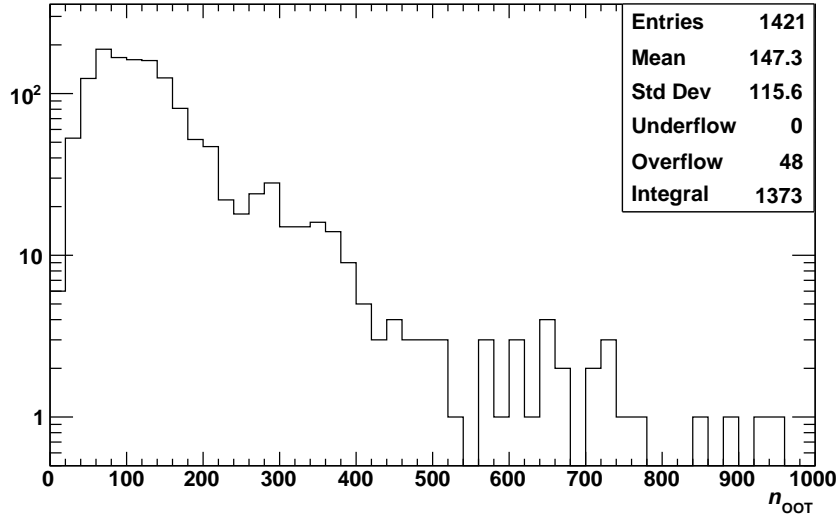
Figure 5.30: The number of ECL out-of-time crystals for the radiative Bhabha control sample, excluding a cut on this quantity (n_{OOT}). The majority of events have a reasonable number of out-of-time crystals, but there are events in this sample exceeding 500 or even 1000 out-of-time crystals.

The full radiative Bhabha control sample selection criteria are summarized in Table 5.6. Aside from the p- or p_T-by-$|dz|$ veto, which will be determined with this sample, these are also the current single-photon selection criteria.

Table 5.6: Summary of the selection criteria for the radiative Bhabha control sample. They are split into requirements that the events must satisfy, and vetoes which must not be satisfied. These are most of the vetoes and requirements currently used in the single-photon analysis

Type	Category	Criteria
Requirements	Single Photon	$E^* > 0.5\,\text{GeV}$
		$16 \leq \text{thetaID} \leq 54$
		If $E^* < 1\,\text{GeV}$, $44° < \theta < 98°$
		$Z_{\text{MVA}} > 0.75$
		$0.5\,\text{cm}^2 < C_{2M} < 1.5\,\text{cm}^2$
	L1 Trigger	At least one of the L1 trigger lines discussed in Chapter 2 is satisfied
	HLT	At least one of the HLT trigger lines discussed in Chapter 2 is satisfied
Vetoes	KLM	$n_K \geq 3$
		$n_K = 2$ and $-10\,\text{ns} < t_K < 30\,\text{ns}$ and $I_K \leq 4$ and $\alpha_K > 15°$
		$n_K = 1$ and $-10\,\text{ns} < t_K < 30\,\text{ns}$ and $I_K \leq 4$ and $\alpha_K > 165°$
	ECL	$E > 300\,\text{MeV}$
		$100\,\text{MeV} < E < 300\,\text{MeV}$ and $|t_c|/\text{dt99} < 3$ and $\alpha_E > 15°$
		$E < 100\,\text{MeV}$ and $|t_c|/\text{dt99} < 1$ and $\alpha_E > 176°$
		$E_t > 100\,\text{MeV}$
	Miscellaneous	$n_{\text{CDC}} > 9$
		$n_{\text{OOT}} > 400$

This control sample also allows the study of the type of Bhabha events that make it through the current criteria. Figure 5.31 is a 2D histogram of the angles from the single photon to the nearest MC electron and nearest MC photon with at least 400 MeV. The 400 MeV requirement for the photon is to ensure that it's a photon that could conceivably cause a single photon cluster. This plot reveals three distinct populations: one where the single photon is near an MC photon, one where it's near an MC electron and not near an MC photon, and one where single photon is near neither an MC electron or MC photon. The events where there is an MC photon near the single photon are what is expected for radiative Bhabha events and occurs when the radiated photon is in the reduced barrel, and the electron tracks are out of acceptance, or not well reconstructed. As the plot reveals however, the majority of events do not fall into this category. The events where the single photon is near an MC electron and not near an MC photon are caused by some of the same issues as the previous category, but instead the single photon is actually the electron ECL cluster, and tracking failed sufficiently so that the track is not matched to the cluster. In this case, the second electron was out of acceptance or also poorly reconstructed.

For the events where the single photon is near both an MC electron and MC photon, these are likely FSR photons, but the characteristics of the event should not significantly differ from those of the broader two categories. The group where there is not an MC electron or MC photon nearby is the smallest of the groups with only 16 entries. In these events the single-photon cluster must be caused by beam background. There are some important questions and considerations for these events because of this: are these events that will show up in data, or are they are an artifact of the way in which MC is constructed? We also need to ensure these events are not double counted by showing up in beam background studies and radiative Bhabha studies. The beam background studies are currently underway, and will help us understand how to treat these events.

In all the radiative Bhabha control sample events the electrons have been missed to at least some degree, and so it is interesting to see where they are in the detector. Figure 5.32 shows the θ vs ϕ distribution for the scattered MC electron and positron. There is a large concentration of events around a θ of 12°, the smallest θ in ECL acceptance. This occurs because there is an ever increasing number of Bhabha events at lower angle, and the Bhabha events in MC15rd are generated

84

3D angular separation of SP and MC γ (°)

3D angular separation of SP and MC $e^{\pm}$ (°)

Entries	1327
Mean x	10.92
Mean y	67.84
Std Dev x	24.24
Std Dev y	44.99
Integral	1327

0	0	0
0	1327	0
0	0	0
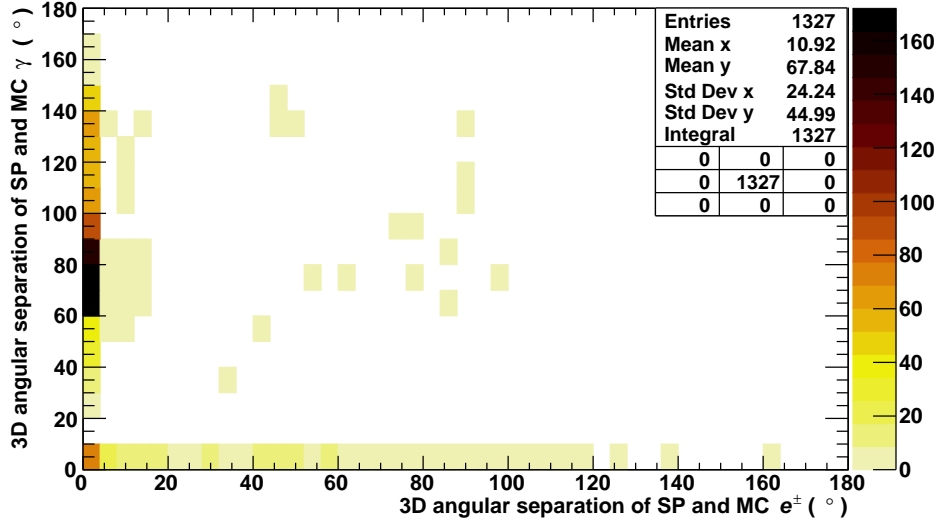
Figure 5.31: The 3D angle between the single photon and the nearest MC photon over 400 MeV is shown as a function of the 3D angle between the single photon and the nearest MC electron. This reveals the true cause of the single-photon clusters, and that in the majority of cases this an electron, not a photon. There are also 16 events where the single photon is not close to either an MC photon or electron. In these events the single-photon cluster is caused by beam background.

with the requirement that both electrons are within ECL acceptance. Unfortunately, events with lower angle Bhabhas are present in data since they occur in Belle II, and as such MC cannot accurately reflect data in this respect. The potential importance of this background indicates, however, that a more useful sample may be imperative to this analysis. This will be discussed further in the next section on the track veto.

It is key to note that at this point, no veto on tracks with few CDC hits or low E_t has been applied. This means some events where there is a high-energy track — likely caused by an electron — have not yet been vetoed. With that caveat, Fig. 5.33 and Fig. 5.34 display the CMS energy of the single photon as a function of the cluster thetaID, and the squared mass recoiling against the single photon as
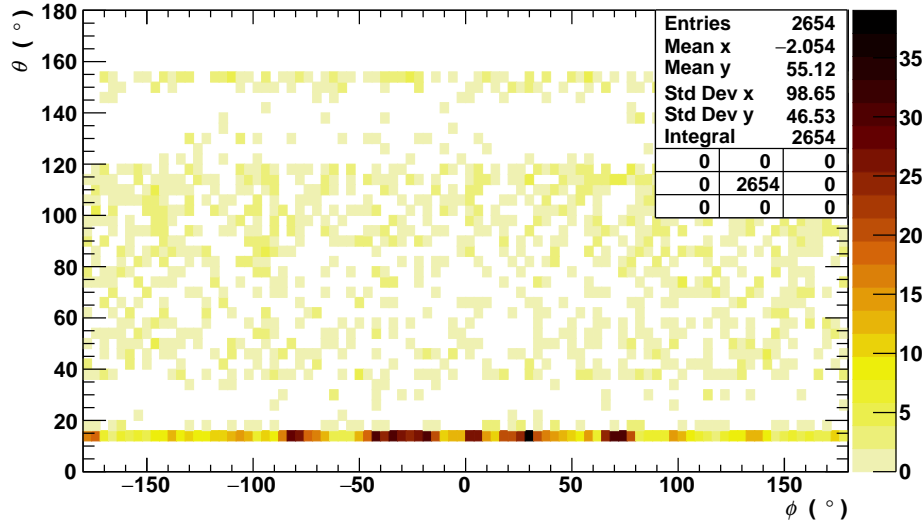
Figure 5.32: θ plotted against ϕ for the non-initial MC electrons in each event. There are two entries per event. There is a concentration of electrons at low θ, at the edge of the ECL acceptance, however there are also many electrons throughout the barrel θ range. For the low angle Bhabhas there is a ϕ dependency, with more electrons being near $0°$ than near $\pm180°$, a dependency that is not seen elsewhere in this plot. This is caused by the boost, which is not perfectly along the z-axis, and consequently biases particles toward $0°$ in ϕ.

a function of the thetaID.

5.7 Track Vetoes

Vetoes on track information are designed to remove events that likely contain a charged particle, since those are not necessarily caught by previous vetoes. The mere presence of a track is not sufficient to veto events, since many tracks are caused by the beam background even in signal events, and we don't want to veto those events. Beam background is an important consideration, particularly looking into the future, and even at the latter part of the current dataset, where the detrimental effects of an ever increasing instantaneous luminosity are obvious. By
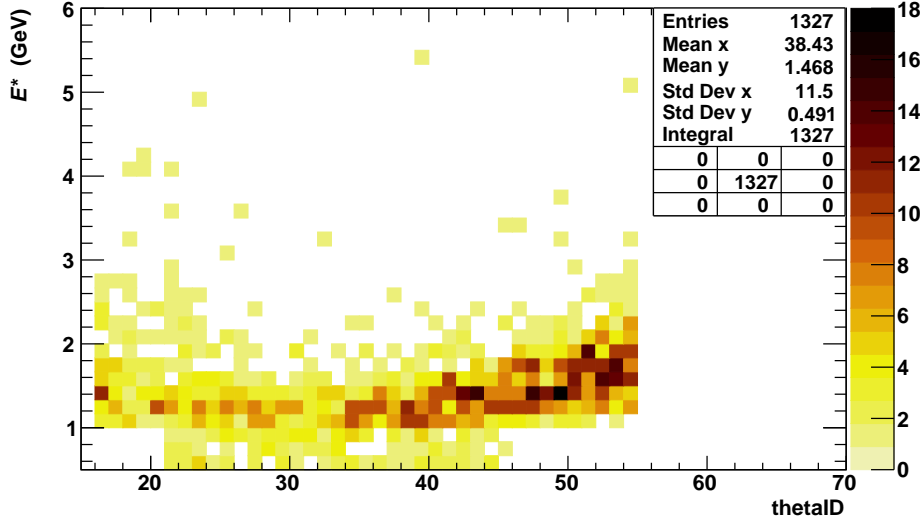
Figure 5.33: The distribution of E^* as a function of the thetaID for the single photon, made using the radiative Bhabha control sample. The thetaID range narrows below $1\,\text{GeV}$ because of the triggers that will be used for the single-photon analysis. Also below $1\,\text{GeV}$ there are fewer events than there likely should be due to the angle requirements used in generic MC15rd Bhabha production.

using the track information, a more selective veto can be made, one tailored to catch higher-energy particles that are collision related.

To achieve this selection, the parameters used need to relate to the energy of the track, and somehow measure its location in the detector. The best available options for energy are the momentum or transverse momentum, p or p_T. There are also two main options for location information, the transverse or longitudinal distance to the IP from the POCA, denoted by dr and dz respectively. p_T, dz, and dr are already in use together in a cut in the single-photon skim, a reduced data sample that is used to lessen the demand on computing resources. This cut is already applied in the single-photon skim that will be used for the single-photon analysis. We cannot avoid this, but we can apply a tighter veto, and veto more events than the skim does. The skim track veto is shown in Table 5.7. Since a tighter veto is possible,
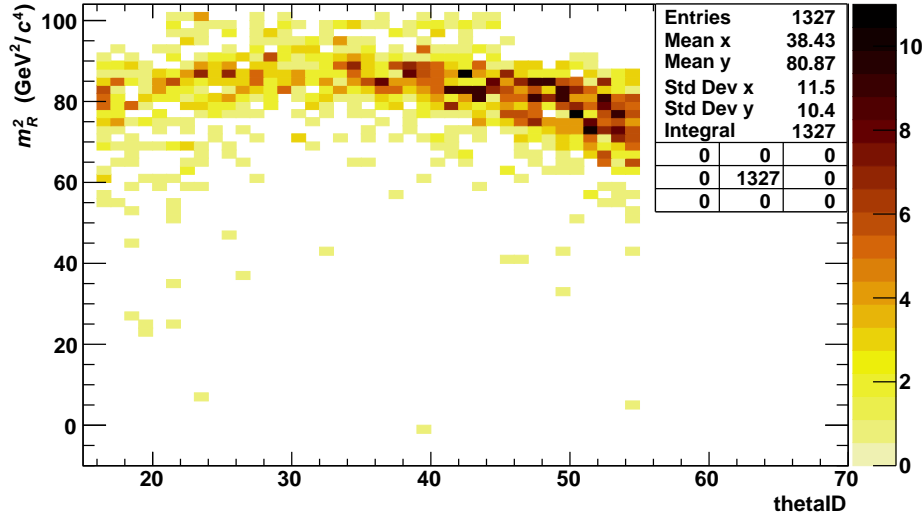
Figure 5.34: The distribution of the square of the mass recoiling against the single photon as a function of the thetaID for the single photon, made using the radiative Bhabha control sample. This plot uses the entire radiative Bhabha control sample, and has no track cuts applied.

it is entirely possible to have no requirement of dr for the track veto, allowing us to make a 2D p_T-by-$|dz|$ veto. Alternatively, we could simply apply a different veto, using p instead of p_T for example, and be cognizant of the skim veto while studying it.

Table 5.7: Summary of the skim track veto. All three criteria must be satisfied to veto the event.

Veto criteria	Explanation of variable
$p_T > 0.15\,\text{GeV}/c$	Transverse momentum of a track
$|dz| < 2\,\text{cm}$	Absolute z distance from POCA to IP
$dr < 0.5\,\text{cm}$	Transverse distance from POCA to IP

The p- or p_T-by-$|dz|$ cut is meant to catch events where a track was reconstructed that originates from the IP and has sufficient transverse momentum to be something we don't want. Radiative Bhabhas, particularly those with higher energy

radiated photons should have tracks like this due to recoil of the photon. However, we are also interested in vetoing events with tracks that do not originate from the IP but that do have a POCA nearby. These tracks could be caused by secondary charged particles. In the case of Bhabhas, tracks like these might be caused by the Bhabhas interacting with the detector just outside of acceptance.

While p_T is used in the skim veto, there's no reason to assume that it is necessarily better than p for our purposes. In order to avoid needing to look at all possible combinations of the cut parameters in detail, receiver operating characteristic (ROC) curves were made for a few p or p_T and $|dz|$ combinations. These can be seen in Fig. 5.35.

These curves show the fraction of the radiative Bhabha control sample rejected by the specific veto as a function of the fraction of the radiative dimuon control sample kept. In these plots the ideal curve would pass through (1,1), and the closer to this point the better. The upper plot uses MC for both samples, while the lower uses data for the radiative dimuon control sample. For the majority of the space, p is significantly better than p_T, and where it is not, they are not far apart, and may in fact be effectively tied in efficacy. While this conclusion is specifically for $|dz| < 10$ cm, the curves for p_T-by-$|dz| < 20$ cm is nearly identical to that of p_T-by-$|dz| < 10$ cm, and so the conclusion will likely hold for other $|dz|$ values too. Based on these ROC plots, p will be used instead of p_T, and a good starting place this veto would be rejecting somewhere in the neighbourhood of 60–80% of the radiative Bhabha control sample.

Now that p has been selected over p_T, we can look at the relevant 2D parameter space for track veto. Plots of this space can be seen in Fig. 5.36.
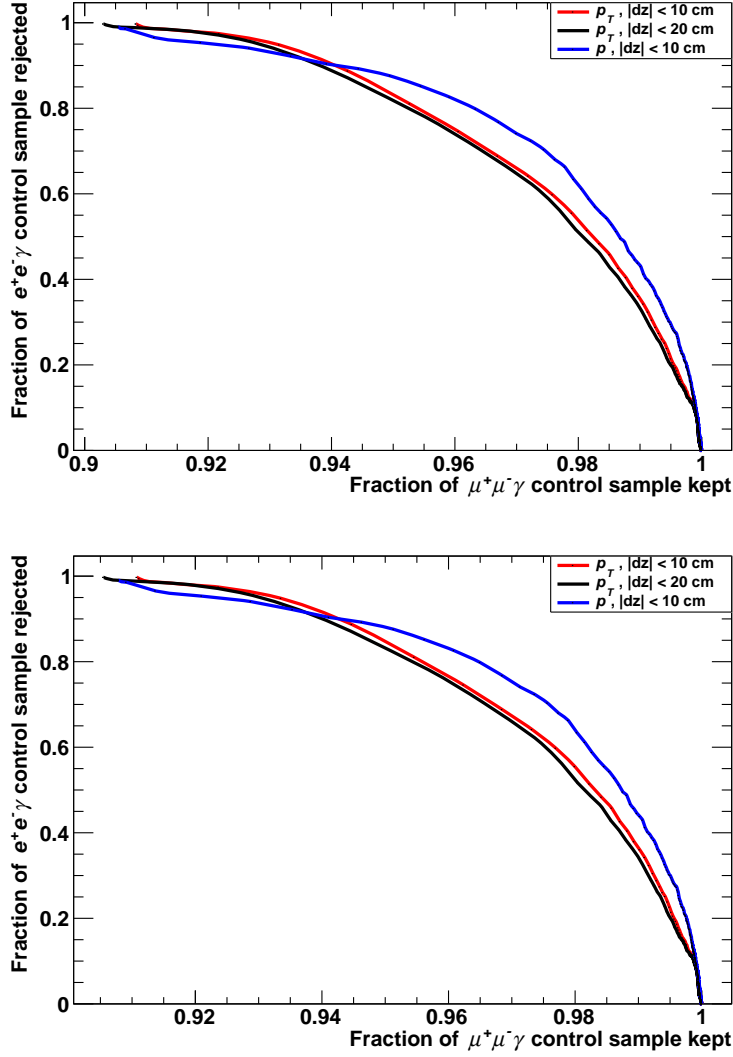
Figure 5.35: ROC curves for the possible track vetoes, using the radiative dimuon control sample as a proxy for signal. On the *y*-axis is the fraction of the radiative Bhabha control sample vetoed, and on the *x*-axis is the fraction of the radiative dimuon control sample kept. The upper plot uses MC for both control samples, while the lower plot uses data for the radiative dimuons. For a p_T-by-$|dz|$ veto there is little difference between a bound of 10 cm or 20 cm, while a p-by-$|dz|$ veto is generally better for the same $|dz|$ bound.
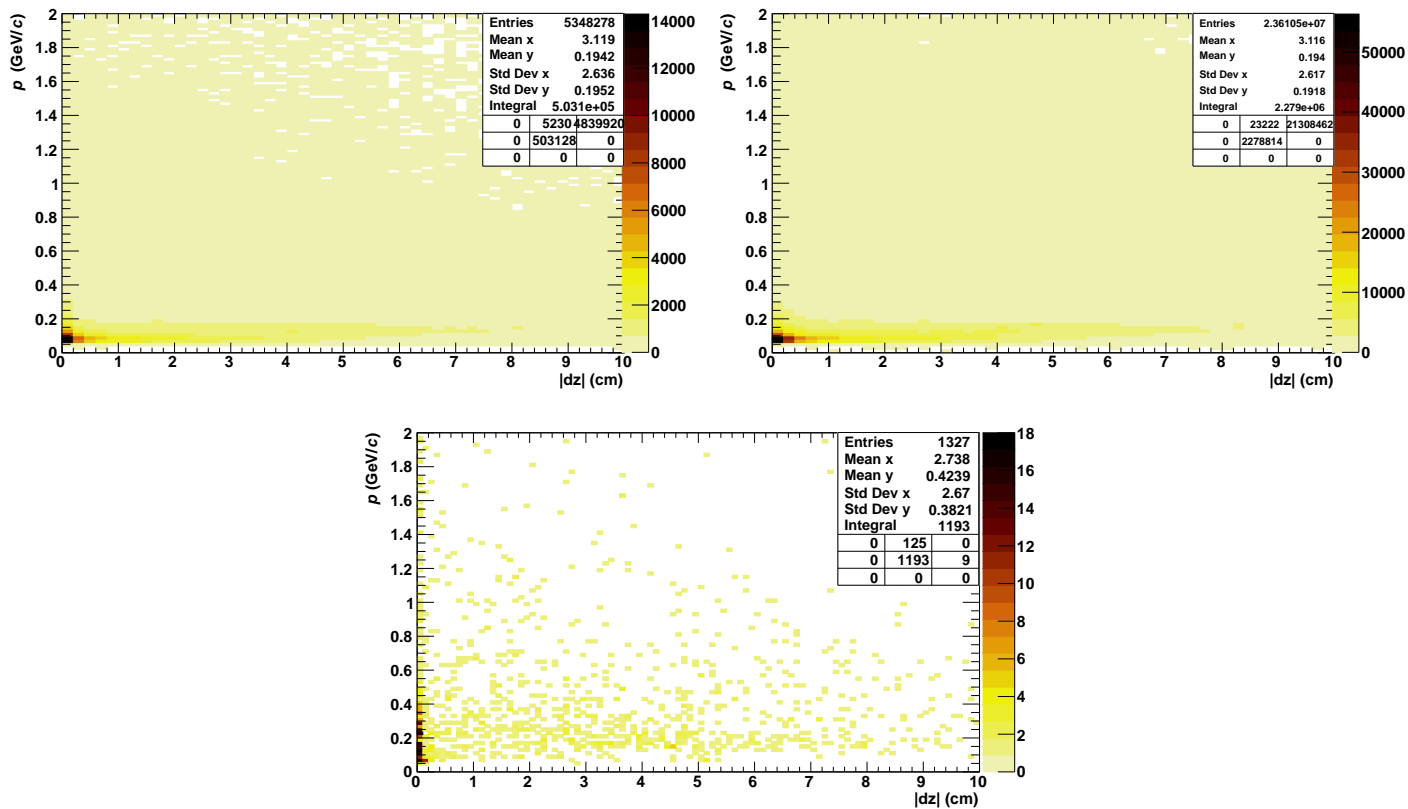
Figure 5.36: Lab momentum as a function of |dz| for the track with the highest momentum that also satisfies |dz| < 10 cm. The upper two plots are made using the radiative dimuon sample, data on the left, MC on the right. The lower plot is for the radiative Bhabha control sample. The radiative dimuon plots have most of their entries in the top right overflow bin because there is no track that satisfies the required |dz|.

These plots are difficult to visually compare due to the differing statistics, but the mean values reveal significantly higher average momentum values, and somewhat smaller |dz| values in the radiative Bhabha sample than in the radiative dimuon sample. Data and MC are in good agreement for radiative dimuons. It's also noticeable that the majority of events in the radiative dimuon plots are in the double overflow bin, which overwhelmingly corresponds to no track in the event. This is in contrast to the radiative Bhabha sample where there are no events in that bin.

Finally to select the values for the boundaries of the p-by-|dz| veto it is useful to look at the veto percentage as function of the p value for several different |dz| values, and then compare these percentages from the radiative dimuon and radiative Bhabha samples. Plots of these percentages can be seen in Fig. 5.37. Note that when using $|dz| < 10\,$cm, and $p > 0\,$GeV$/c$ for the veto, the plot for the radiative Bhabhas indicates that $\sim 100\%$ of events are vetoed — compared to $\sim 10\%$ for the radiative dimuon sample — which means virtually all events have a track that originates near the IP, which was somewhat unexpected. This is discussed further below.
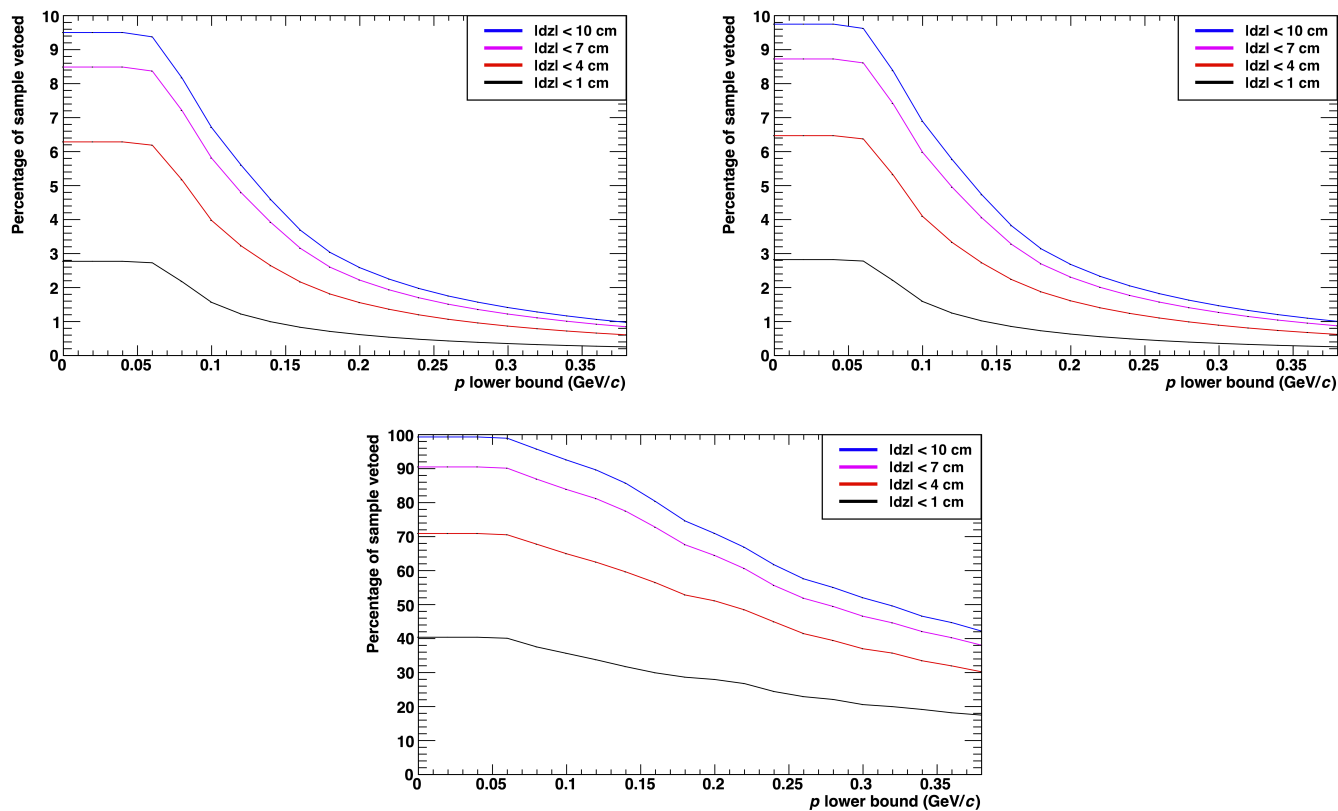
Figure 5.37: Percentage of the sample vetoed as a function of the momentum bound. The upper two plots are made using the radiative dimuon sample, data on the left, MC on the right. The lower plot is for the radiative Bhabha control sample. The radiative dimuon plots veto at most around 10% of events, because the rest of the events do not have any extra tracks. On the other hand, nearly 100% of radiative Bhabha tracks have tracks, and so are vetoed when using a large $|dz|$ upper bound and a lower p bound of $0 \, \text{GeV}/c$.

These plots indicate that a veto of $p > 0.2\,\text{GeV}/c$ and $|\text{dz}| < 10\,\text{cm}$ vetoes around 72% of the radiative Bhabha control sample, and just over 2% of the radiative dimuon control sample. It is also in the region of the plots where, as the p-bound is lowered, the percentage of radiative Bhabhas vetoed increases quickly, but is just before where the percentage of radiative dimuons vetoed increases rapidly. In other words, this is a more conservative veto for now, since there's still more information required to justify a stronger veto. Some of that necessary information will, in future, come from a new radiative Bhabha MC sample.

As mentioned above, virtually all radiative Bhabha control sample events have tracks. This is assumed to be a result of how this sample of MC was generated, because the current MC15rd sample requires both electrons be within ECL acceptance. This results in there being no events in which the electrons are at low enough angles to not leave tracks, and as such, this sample isn't enough to decide this veto. Another MC sample has been requested, which would also use MC15rd but have different angle requirements. This sample will require that either an energetic photon or one of electrons be within the barrel, while at least one of the electrons is outside of the ECL acceptance. The sample will cover an entirely separate set of Bhabha events than the generic MC15rd, and will be used to update the results in this section. Full optimization, however, will require all relevant backgrounds to be sufficiently studied so that a more quantitative measure, such as a figure of merit, can be used to determine the ideal veto bounds. The study of this track veto will need to be revisited when the requested sample is available, and the other backgrounds are better understood.

Despite the temporariness of this vetoes' boundaries, applying it to the radiative Bhabha control sample is useful because the plots of E^* and recoil mass squared as a function of thetaID are demonstrative of the final result for this background. The skim veto is also applied for these plots, though it only vetoes 12 extra events. The aforementioned plots are Fig. 5.38 and Fig. 5.39 respectively.

With the track veto applied, the radiative Bhabha cross section above $0.5\,\text{GeV}$ is 9.1 fb and above $2\,\text{GeV}$ is 0.77 fb.
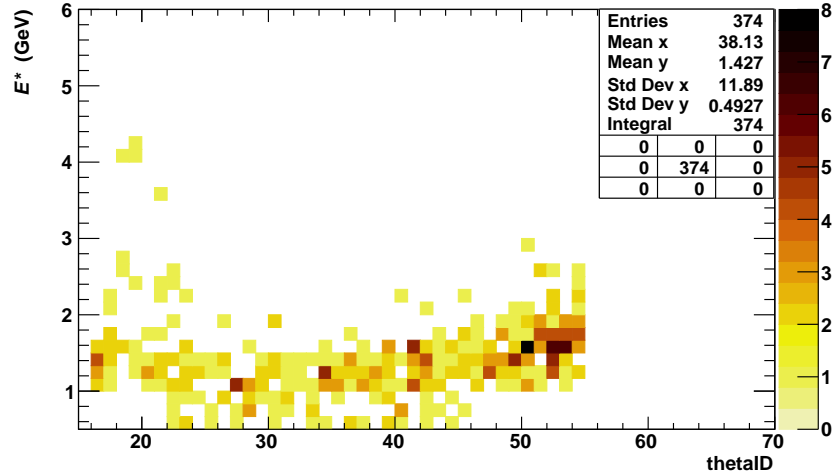
Figure 5.38: The distribution of E^* as a function of the thetaID for the single photon for the radiative Bhabha control sample with the track veto applied. The skim veto is also applied, though its affect is small. The track veto removed almost 75% of control sample events, and particularly removed events with a higher single-photon E^*.
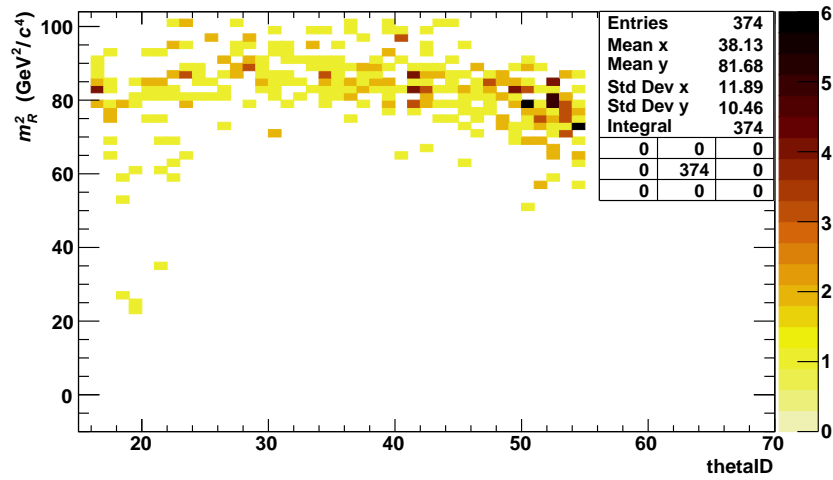
Figure 5.39: The distribution of the square of the mass recoiling against the single photon as a function of the thetaID for the single photon, made using the radiative Bhabha control sample with the track veto applied. The skim veto is also applied, though its affect is small.

5.8 Veto Summary

A summary of the single-photon vetoes discussed in this chapter are shown in Table 5.8. This table also includes the veto percentages of the control sample due to these cuts individually and combined, for both data and MC. The table also has the ratio of the veto percentages, which makes it apparent where MC best represents data and where it does not.

As expected, MC and data do not agree for the few-layer KLM vetoes, which makes sense since there was marked disagreement between data and MC for a variety of KLM quantities for KLM clusters with few layers. Interestingly, in general, MC tends to underestimate the KLM veto percents, and particularly underestimates the 1-layer veto. This is not what might initially be expected, because one of the major disagreements between MC and data for KLM clusters is caused by multi-strip hits, and tends to result in more clusters in MC than data. The increased number of clusters would be expected to cause higher KLM veto percentages in MC, not lower veto percentages. However, most of the data-MC discrepancy related to multi-strip hits for 1- and 2-layer KLM clusters is due to KLM clusters caused by the recoil photon (see Fig. 5.22), and because we intentionally constructed the KLM vetoes such that single-photon-caused KLM clusters do not veto events, the multi-strip hit issue does not factor in very much to the data-MC veto percentage disagreement.

Conversely to the KLM vetoes, MC overestimates the effect the photon vetoes have, with the higher energy vetoes being significantly worse. This was not entirely expected, as MC has many more extra photons present, increasing the chances of one meeting the veto requirements.

The vetoes on E_t, n_{CDC}, and p-by-$|dz|$ all have excellent data-MC agreement. The veto percentage for the n_{OOT} veto could not be checked with current ntuples, but will be calculated in future.

Table 5.8: A summary of the vetoes described in this thesis for the single-photon analysis. The percentage of the radiative dimuon control sample vetoed by each veto is tabulated (if known) for data, MC, and their ratio. These veto percentages are calculated with each veto acting individually. The total percentage vetoed is also displayed.

Category	Veto		% vetoed		
	Main criterion	Other criteria	Data	MC	Data/MC
KLM	$n_K \geq 3$	–	0.58	0.54	1.1
	$n_K = 2$	$-10\,\mathrm{ns} < t_K < 30\,\mathrm{ns}$ $I_K \leq 4$ $\alpha_K > 15°$	0.15	0.11	1.3
	$n_K = 1$	$-10\,\mathrm{ns} < t_K < 30\,\mathrm{ns}$ $I_K \leq 4$ $\alpha_K > 165°$	0.17	0.081	2.1
ECL	$E > 300\,\mathrm{MeV}$	–	0.37	0.62	0.60
	$100\,\mathrm{MeV} < E < 300\,\mathrm{MeV}$	$|t_c|/\mathrm{dt99} < 3$ $\alpha_E > 15°$	3.4	4.4	0.77
	$E < 100\,\mathrm{MeV}$	$|t_c|/\mathrm{dt99} < 1$ $\alpha_E > 176°$	0.16	0.17	0.96
	$E_t > 100\,\mathrm{MeV}$	–	0.33	0.32	1.0
Tracks	$n_{\mathrm{CDC}} > 9$	–	1.6	1.6	1.0
	$p > 0.2\,\mathrm{GeV}/c$	$|dz| < 10\,\mathrm{cm}$	2.6	2.7	0.97
Miscellaneous	$n_{\mathrm{OOT}} > 400$	–	–	–	–
Combined	–	–	8.2	9.4	0.87

Since the mid energy photon veto is the biggest veto, and the other large vetoes have good data-MC agreement, the overall data-MC disagreement is small, but not insignificant, with a data/MC ratio of 0.87. It's also interesting to note that the different vetoes are largely orthogonal. The KLM vetoes, and the extra photon ECL vetoes are fully orthogonal within their category by design, but there is no reason that the other vetoes have to be. If all the vetoes were fully orthogonal 9.4%, and 11% of data and MC would be vetoed, respectively, instead of the actual 8.2%, and 9.4%.

Chapter 6

Conclusion and prospects

The dark photon is a hypothetical particle in the dark sector. It is a massive gauge boson, and mediates a dark equivalent of the electromagnetic force. The dark photon mixes with the regular photon, allowing its production and detection. At Belle II, the dark photon can be produced by the annihilation of an e^+e^- pair. If the dark photon mass is large enough relative to the mass of other dark matter particles, it can decay invisibly. These events can be detected when they involve the initial state radiation of a photon. Belle II is well suited for this analysis due to the clean environment of the e^+e^- collisions, its dedicated single-photon triggers, and its hermiticity.

The single-photon analysis is the search for the invisible decay of the dark photon at Belle II. An overview of the single-photon analysis and its components was given. Two components of this analysis were presented, namely the study of a signal proxy, and the study of the radiative Bhabha background. Vetoes for the single-photon analysis designed from these studies were explained, and their veto percentages were calculated for both data and MC.

The next step for the work presented in this thesis is the reproduction of the radiative Bhabha control sample with a new MC sample generated specifically for this study. This will permit a more complete study of the radiative Bhabha background, particularly at low angle and low centre of mass energy. With this information, and the information from the other backgrounds, the track cut can be adjusted so that it improves the sensitivity of the search. The recoil mass squared as a function of

thetaID plot can also be adjusted, which will be used in the fitting of the radiative bhabha background.

In the next version of Belle II analysis and reconstruction software, there are two changes that are particularly relevant for the single-photon analysis: multi-strip hits will be used in reconstruction, and the ECL clustering algorithms have been fixed.

The multi-strip hit change will allow far more photon-caused KLM clusters to be reconstructed correctly, or reconstructed at all. This will improve the rejection of background events, particularly radiative Bhabha and $\gamma\gamma(\gamma)$ events, as the KLM may detect photons when the ECL has failed.

The fixed ECL clustering will also improve background rejection by correctly reconstructing more than one photon. This effect will be most prominent in events with a larger beam background, like those recorded near the end of data-taking.

For the analysis as a whole to progress, the other components need to be completed. Several of the sections have already been completed by other members of the analysis team, or are currently underway. The major outstanding components are the study of signal MC, and data-MC corrections. After these are completed, and all components finalized, the systematic uncertainty estimations, and unblinding can commence.

The single-photon analysis will, once complete, explore new parameter space for the dark photon. This parameter space includes regions in which the dark photon could explain the relic density of dark matter in the universe. This will contribute meaningfully to the search for dark matter. The future is bright (or possibly, dark).

Bibliography

[1] X-ray: NASA/CXC/CfA/M.Markevitch et al.; Optical: NASA/STScI; Magellan/U.Arizona/D.Clowe et al.; Lensing Map: NASA/STScI; ESO WFI; Magellan/U.Arizona/D.Clowe et al. https://chandra.harvard.edu/photo/2006/1e0657/. Accessed 2023. → page 5

[2] A. Abashian et al. The Belle detector. *Nuclear Instruments and Methods in Physics Research Section A: Accelerators, Spectrometers, Detectors and Associated Equipment*, 479(1):117–232, 2002. ISSN 0168-9002. doi:10.1016/S0168-9002(01)02013-7. → page 12

[3] L. Bergström. Non-baryonic dark matter: observational evidence and detection methods. *Reports on Progress in Physics*, 63(5):793, May 2000. doi:10.1088/0034-4885/63/5/2r3. → pages 3, 4

[4] G. Bertone, editor. *Particle Dark Matter: Observations, Models and Searches*. Cambridge University Press, 2010. doi:10.1017/CBO9780511770739. → pages 2, 4

[5] G. Bertone and D. Hooper. History of dark matter. *Reviews of Modern Physics*, 90:045002, Oct 2018. doi:10.1103/RevModPhys.90.045002. → page 4

[6] G. Bertone, D. Hooper, and J. Silk. Particle dark matter: evidence, candidates and constraints. *Physics Reports*, 405(5):279–390, 2005. ISSN 0370-1573. doi:10.1016/j.physrep.2004.08.031. → pages 2, 4

[7] K. Bleuler. *The Gauge Principle in Modern Physics*, pages 279–288. Springer US, Boston, MA, 1986. ISBN 978-1-4684-5221-1. doi:10.1007/978-1-4684-5221-1_31. → page 6

[8] A. Boveia and C. Doglioni. Dark matter searches at colliders. *Annual Review of Nuclear and Particle Science*, 68(1):429–459, 2018. doi:10.1146/annurev-nucl-101917-021008. → pages 4, 6, 7

[9] R. Brun and F. Rademakers. ROOT — An object oriented data analysis framework. *Nuclear Instruments and Methods in Physics Research Section A: Accelerators, Spectrometers, Detectors and Associated Equipment*, 389: 81–86, 1997. doi:10.1016/S0168-9002(97)00048-X. URL https://root.cern/. → page 21

[10] D. Clowe, A. Gonzalez, and M. Markevitch. Weak-lensing mass reconstruction of the interacting cluster 1E 0657–558: Direct evidence for the existence of dark matter. *The Astrophysical Journal*, 604(2):596, Apr 2004. doi:10.1086/381970. → page 4

[11] D. Clowe, M. Bradač, A. H. Gonzalez, M. Markevitch, S. W. Randall, C. Jones, and D. Zaritsky. A direct empirical proof of the existence of dark matter. *The Astrophysical Journal*, 648(2):L109, Aug 2006. doi:10.1086/508162. → page 4

[12] P. de Bernardis et al. A flat universe from high-resolution maps of the cosmic microwave background radiation. *Nature*, 404(6781):955–959, Apr 2000. ISSN 1476-4687. doi:10.1038/35010035. → page 2

[13] Z. Dolezal and S. Uno. Belle II technical design report. Oct 2010. doi:10.48550/arXiv.1011.0352. → pages 8, 11, 12

[14] M. Fabbrichesi, E. Gabrielli, and G. Lanfranchi. *The Physics of the Dark Photon*. Springer International Publishing, 2021. doi:10.1007/978-3-030-62519-1. → pages 6, 23, 24, 29

[15] G. Finocchiaro. Update on Klong ID preparation for release-08. https://indico.belle2.org/event/9494/#1-update-on-klong-id-preparati, 2023. Internal Presentation. → page 67

[16] M. Graham, C. Hearty, and M. Williams. Searches for dark photons at accelerators. *Annual Review of Nuclear and Particle Science*, 71(1):37–58, 2021. doi:10.1146/annurev-nucl-110320-051823. → pages 22, 23, 24, 25, 26

[17] T. HARA and on behalf of the Belle II computing group. Computing at the Belle II experiment. *Journal of Physics: Conference Series*, 664(1):012002, Dec 2015. doi:10.1088/1742-6596/664/1/012002. → page 21

[18] T. Hara, T. Kuhr, and Y. Ushiroda. Belle II coordinate system and guideline of Belle II numbering scheme. Aug 2011. Internal Collaboration Note. → page 10

[19] E. Hill and C. Hearty. Time calibration of the Belle II ECL crystals and crates. Jan 2019. Internal Collaboration Note. → page 13

[20] S. Hong, G. Kurup, and M. Perelstein. Dark matter from a conformal dark sector. *Journal of High Energy Physics*, 2023(2):221, Feb 2023. ISSN 1029-8479. doi:10.1007/JHEP02(2023)221. → page 6

[21] W. Hu and S. Dodelson. Cosmic microwave background anisotropies. *Annual Review of Astronomy and Astrophysics*, 40(1):171–216, Sep 2002. doi:10.1146/annurev.astro.40.060401.093926. → pages 2, 3

[22] E. Kou et al. The Belle II Physics Book. *Progress of Theoretical and Experimental Physics*, 2019(12):123C01, 12 2019. ISSN 2050-3911. doi:10.1093/ptep/ptz106. → pages 8, 9, 23

[23] T. Kuhr, C. Pulvermacher, M. Ritter, T. Hauth, and N. Braun. The Belle II core software. *Computing and Software for Big Science*, 3(1):1, Nov 2018. ISSN 2510-2044. doi:10.1007/s41781-018-0017-9. → page 21

[24] M. D. Nuccio and T. Ferber. *Search for Axion-Like Particles produced in e^+e^- collisions and photon energy resolution studies at Belle II*. PhD thesis, Hamburg, University of Hamburg, Hamburg, 2021. Presented on 19-10-2021. → page 31

[25] Paraficz, D., Kneib, J.-P., Richard, J., Morandi, A., Limousin, M., Jullo, E., and Martinez, J. The Bullet cluster at its best: weighing stars, gas, and dark matter. *Astronomy and Astrophysics*, 594:A121, 2016. doi:10.1051/0004-6361/201527959. → page 4

[26] S. Prell. Efficiency and muon ID. https://indico.belle2.org/event/8079/#5-efficiency-and-muon-id, 2022. Internal Presentation. → page 67

[27] M. Schmaltz and N. Weiner. A portalino to the dark sector. *Journal of High Energy Physics*, 2019(2):105, Feb 2019. ISSN 1029-8479. doi:10.1007/JHEP02(2019)105. → page 6

[28] H. Svidras, M. Röhrken, S. Wehle, and K. Tackmann. Measurement of the data to MC ratio of photon reconstruction efficiency of the Belle II calorimeter using radiative muon pair events. Oct 2020. → pages 34, 52

[29] M. Taoso, G. Bertone, and A. Masiero. Dark matter candidates: a ten-point test. *Journal of Cosmology and Astroparticle Physics*, 2008(03):022, Mar 2008. doi:10.1088/1475-7516/2008/03/022. → page 5

[30] T. S. van Albada, J. N. Bahcall, K. Begeman, and R. Sancisi. Distribution of dark matter in the spiral galaxy NGC 3198. *The Astrophysical Journal*, 295: 305–313, Aug. 1985. doi:10.1086/163375. → page 3

[31] M. Wakai. Search for invisible decays of dark photon at Belle II. Master's thesis, University of British Columbia, 2021. → page 28

Appendix A

Supporting Materials

A.1   Trigger lines

The full HLT lines required as part of the radiative Bhabha control sample are listed below with an explanation of the requirements:

- software‿ trigger‿ cut&filter&ge1‿ Estargt2‿ GeV‿ neutral‿ clst‿ 32130‿ not‿ gg2clst‿ ee1leg1clst‿ ee1leg1trk‿ eeBrem

  – At least one $E^* > 2\,\mathrm{GeV}$ neutral ECL cluster in θ range [32°, 130°] and not meeting the requirements of a $\gamma\gamma$ event or a partially detected Bhabha event.

- software‿ trigger‿ cut&filter&1‿ photon‿ Estargt1‿ GeV‿ clust‿ in‿ 45115‿ and‿ no‿ other‿ clust‿ Estargt0.3‿ GeV

  – Exactly one $E^* > 1$ photon ECL cluster in θ range [45°, 115°] and no other $E^* > 0.3\,\mathrm{GeV}$ ECL clusters

- software‿ trigger‿ cut&filter&1‿ photon‿ Estargt0.5‿ GeV‿ clust‿ in‿ 4498‿ and‿ no‿ other‿ clust‿ Estargt0.3‿ GeV

  – Exactly one $E^* > 0.5$ photon ECL cluster in θ range [44°, 98°] and no other $E^* > 0.3\,\mathrm{GeV}$ ECL clusters

Similarly, the L1 trigger lines required as part of the radiative Bhabha control sample are listed below with an explanation of the requirements:

- hie

    - Total combined energy $> 1\,\text{GeV}$ in the ECL crystals with $4 \leq \text{thetaID} \leq 58$. The event must not be vetoed for being classified as a Bhabha or by the injection veto

- lml6

    - Exactly one $E^* > 1\,\text{GeV}$ cluster with $13 \leq \text{thetaID} \leq 58$ and no other $E > 0.3\,\text{GeV}$ cluster. The event must not be vetoed by the injection veto.

- lml13

    - Exactly one $E^* > 0.5\,\text{GeV}$ cluster with $21 \leq \text{thetaID} \leq 44$ and no other $E > 0.3\,\text{GeV}$ cluster. The event must not be vetoed by the injection veto.

- lml16

    - Exactly one $E^* > 0.5\,\text{GeV}$ cluster with $21 \leq \text{thetaID} \leq 44$ and no other $E > 0.3\,\text{GeV}$ cluster. The event must not have a track (as defined by the L1 trigger, or be vetoed by the injection veto.

The requirements for classification as a Bhabha event for the L1 trigger are as follows:

1. There are at least two ECL clusters, one of which has $E^* > 3\,\text{GeV}$ and another that has $E^* > 4.5\,\text{GeV}$

2. The sum of the CMS frame polar angles for those two clusters is in the range $[165°, 190°]$

3. The difference of the CMS frame polar angles for those two clusters is in the range $[160°, 200°]$